Alberto Sartori

DYNAMICAL PROPERTIES OF BOSE-BOSE MIXTURES

PhD Thesis, March 7th, 2016

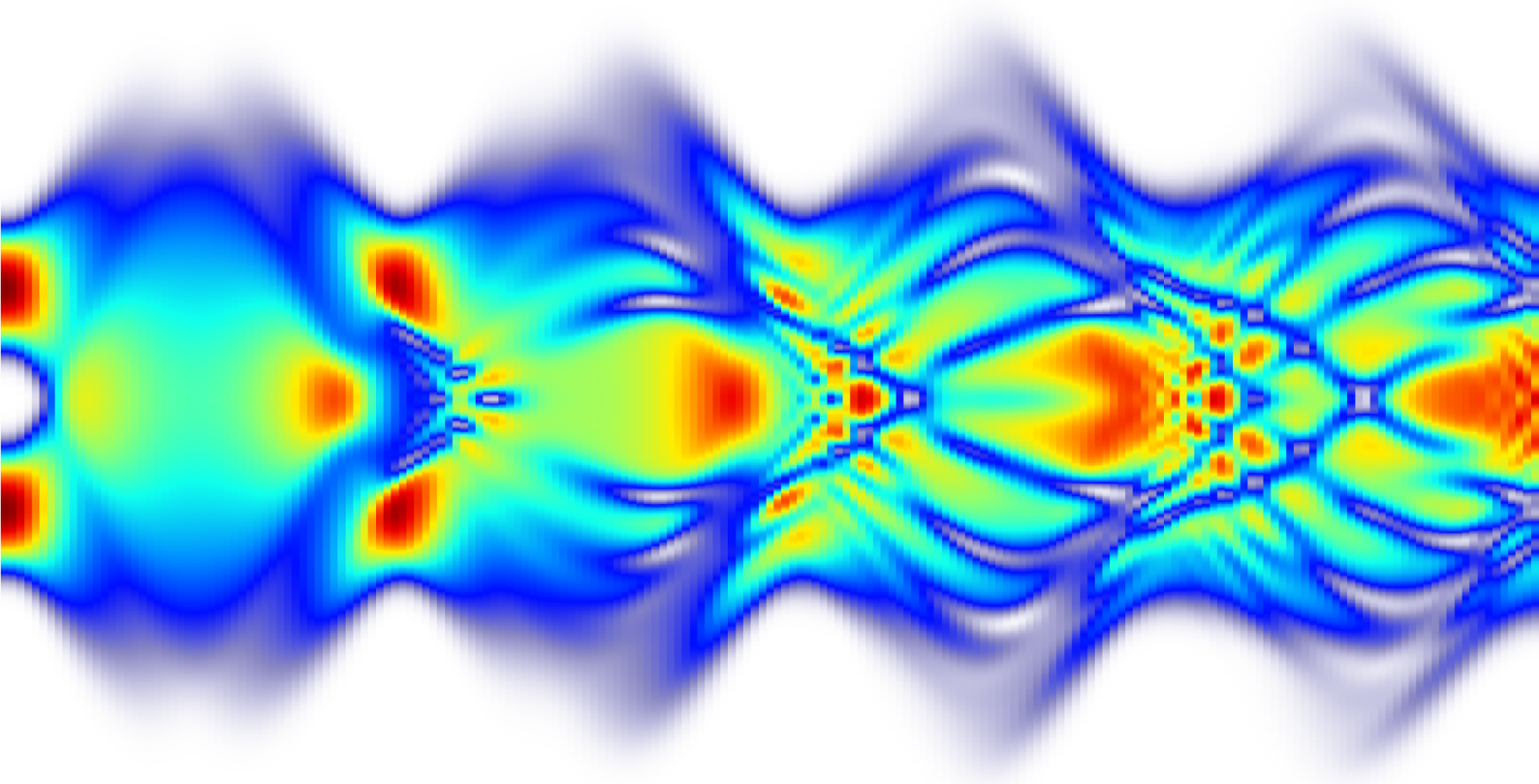

UNIVERSITÀ DEGLI STUDI
DI TRENTO

SUPERVISOR
Dr. Alessio Recati

Contents

Appendices

List of Figures

Introduction

This Thesis summarizes the main topics of the research activity I have performed during the three years of my PhD education at the Department of Physics of the University of Trento, specifically at the INO-CNR BEC Center, under the supervision of Dr. Alessio Recati. The subject of this Thesis is the study of the dynamics of mixtures of ultracold Bose gases.

Ultracold gases allow the realization of multi-component Bose-Einstein condensates (BECs). The latter are novel systems, whose behaviour is very different with respect to that of a single component BEC. In particular they show different zero-temperature phases, each described by a proper vector order parameter. The possibility of tuning a number of system parameters, such as the interaction strength through Feshbach resonances, and the possibility of tailoring the trapping potentials make such systems ideal for studying the structure of the various phases and the nature of the phase transitions and give rise to new ground states and to peculiar dynamic processes. The problem is very general being related to the long standing issue of phases and stability of interacting superfluids. In particular superfluid current stability in mixtures [1, 2, 3] has been started to be addressed experimentally only recently [4].

In the present work we consider one of the easiest implementations, namely a 2-component (spinor) condensate with an (optional) external field that drives the population transfer (spin-flipping) between the two atomic levels. In spite of the apparent simplicity of the problem, the physics it contains is very rich. Indeed, spinor condensates allow us to address many interesting phenomena from the Andreev-Bashkin effect [5,

6] to the (internal) Josephson effect [7, 8], or Schrödinger-cat- and twin-Fock-like states [9, 10], from dimerized vortices [11, 12, 13], to the study of quenching in classical bifurcations [14, 15, 16]. They represent also the basis for most of the recent realizations of artificial gauges in cold gases [17].

Moreover, thanks to new technological developments, mixtures with high unbalance between the two components have attracted a lot of attention both on the theoretical and experimental side with a huge number of different realizations and regimes (see, e.g., the recent experimental works [18, 19] and reference therein). This is quite obvious being the impurity problem almost ubiquitous in physics, especially in condensed matter physics [20].

Thesis outline

This Thesis is organized as follows. The *first chapter* provides a general introduction to Bose-Einstein condensation and mixtures of of condensates. It includes a derivation of Gross-Pitaevskii equations for the different types of mixtures considered in this Thesis and a description of the theoretical foundation of the topics discussed in next chapters.

In the *second chapter* we focus on homogeneous systems. We describe the different ground states the mixture has with or without coherent coupling and we show the excitation spectra in both cases. In the last section we address the problem of stability of persistent currents in a mixture. We find the criterion for their stability both in the miscible and immiscible regime and, in the first case, we also discover a regime of partial instability. The existence of this regime could be at the origin of the experimental observations in [4].

The *third chapter* is instead devoted to the study of a mixture in an external harmonic potential. We first describe how ground states change from the homogeneous case introducing and characterizing a new solitonic structure (Double Domain Wall Soliton) found in highly unbalanced mixtures. We then analyse the second order ferromagnetic transition occurring in a coherently coupled mixture by studying its static and dynamic response to a spin-dipole perturbation. In the ferromagnetic phase we also observe a phenomena related to ground state selection.

The *fourth chapter* describes the numerical method used for obtaining all the results of previous chapters, namely the time evolving split-operator method. We give the details of its implementation and we describe some tricks used to make the algorithm more efficient.

In the *fifth chapter* I introduce a different numerical method for simulating quantum systems taking into account quantum correlations, namely Tensor Network method. This Chapter is a summary of what I learnt on the last year of my PhD working with Jun. Prof. Matteo Rizzi from the Johannes Gutenberg Universität of Mainz. I give a brief description of the tools needed for understanding this method, I explain why and when it is useful and what are the differences with respect to other methods. I introduce Matrix Product States and Matrix Product Operators that are the building block for the implementation of the variational algorithm and for the algorithms used for getting the time evolution of a quantum state. In the last section I describe and compare different types of time evolving algorithms applying them to some literature results.

List of publications

The original results presented in this thesis have been published in the following articles:

(i) A. Sartori and A. Recati, Dynamics of highly unbalanced Bose-Bose mixtures: miscible vs immiscible gases, *Eur. Phys. J. D*, **67**, 260 (2013), Ref. [21]

(ii) M. Abad, A. Sartori, S. Finazzi and A. Recati, Persistent currents in two-component condensates in a toroidal trap, *Phys. Rev. A*, **89**, 053602 (2014), Ref. [22]

(iii) A. Sartori, J. Marino, S. Stringari and A. Recati, Spin dipole oscillation and relaxation of coherently coupled Bose-Einstein condensates, *New. J. Phys.*, **17**, 093036 (2015), Ref. [23]

CHAPTER

1 Bose-Einstein Condensation and Bose-Bose mixtures

In this first introductive Chapter we lay the theoretical foundation of Bose-Einstein condensation and Bose-Bose mixtures. We introduce the Gross-Pitaevskii equation and coherently coupled condensates reporting the main equations that will be used in the next chapters.

Contents

1.1 The Gross-Pitaevskii equation

In this Section we give a brief derivation of the Gross-Pitaevskii equation, for a more detailed analysis please see [24] or [25].

Let us consider an atomic Bose gas of N particles enclosed in a volume V. The position and momentum of each particle will be denoted by $\mathbf{r}_i$ and $\mathbf{p}_i$, respectively, with $i \in \{1,2,...,N\}$ the particle index. Each couple of atoms interacts through some interatomic potential $V(\mathbf{r}_i - \mathbf{r}_j)$ depending on their relative position. For neutral atoms, any realistic interatomic potential is typically isotropic (it depends only on the relative distance $r_{ij} = |\mathbf{r}_i - \mathbf{r}_j|$ of the atoms) and short-range (there exists a distance r_0 called range of the potential beyond which the potential is negligible). In a dilute atomic gas the mean interparticle distance $d = n^{-1/3}$, fixed by the average density $n = N/V$, is much larger than the range of the potential r_0, i.e. the inequality

$$n{r_0}^3 \ll 1 \tag{1.1}$$

holds. Condition (1.1) implies that the probability of finding three or more particles simultaneously within a sphere of radius r_0 is much smaller than the probability of finding only two atoms within this distance. As a consequence, one is allowed to consider only configurations involving pairs of interacting particles, i.e. to take into account only binary collisions.

Another consequence of inequality (1.1) is that the large distance between particles allows for the use of the asymptotic expression for the wave function of their relative motion, which is fixed by the scattering amplitude. Therefore the specific details of the two-body potential will not matter and all the properties of the system will depend only on this quantity. In addition, at temperatures smaller than the critical temperature for Bose-Einstein condensation, the scattering amplitude becomes independent of energy as well as of the scattering angle, and can be safely replaced with its low-energy value. The latter, according to standard scattering theory, is determined by the so-called s-wave scattering length a (see, for example, [24]). In conclusion, one expects that all the effects of the interactions on the physical properties of the gas are determined by one single parameter, which is exactly the s-wave scattering length a. In particular the small interactions condition can be written as

$$n|a|^3 \ll 1. \tag{1.2}$$

The quantity $n|a|^3$ is usually referred as the gas parameter.

The many-body Hamiltonian of an atomic Bose gas of N particles can be written as

$$H = \sum_{i=1}^{N} \left(\frac{-\hbar^2 \nabla^2}{2m} + V_{\text{ext}}(\mathbf{r}_i) \right) + \frac{1}{2} \sum_{i,j=1}^{N} \mathcal{V}(\mathbf{r}_i - \mathbf{r}_j) \tag{1.3}$$

where m is the atomic mass, and we have introduced an external potential $V_{\text{ext}}(\mathbf{r})$. Let us now rewrite H in the formalism of second quantization, introducing the atomic field operator ψ

$$H = \int \mathrm{d}\mathbf{r}\, \psi^\dagger(\mathbf{r}) \left(\frac{-\hbar^2 \nabla^2}{2m} + V_{\text{ext}}(\mathbf{r}_i) \right) \psi(\mathbf{r}) + \frac{1}{2} \int \mathrm{d}\mathbf{r}'\, \mathrm{d}\mathbf{r}\, \psi^\dagger(\mathbf{r}) \psi^\dagger(\mathbf{r}') \mathcal{V}(\mathbf{r}' - \mathbf{r}) \psi(\mathbf{r}) \psi(\mathbf{r}') \tag{1.4}$$

The field operator can be conveniently written in the form

$$\psi(\mathbf{r}) = \sum_j \varphi_j(\mathbf{r})\, a_j \tag{1.5}$$

where the summation runs over all the possible values of a complete set of quantum numbers j, φ_j represents a convenient basis of single-particle wave functions, and a_j ($a_j^\dagger$) are the annihilation (creation) operators of a particle in the state φ_j.

Bose-Einstein condensation occurs when one of the single-particle states ($j = 0$) is occupied in a macroscopic way, i.e. its occupation number N_0 is of the order of N. In this case, it is useful to rewrite Eq. (1.5) separating the contribution of the condensate term from the other ones:

$$\psi(\mathbf{r}) = \varphi_0(\mathbf{r})\, a_0 + \sum_{j \neq 0} \varphi_j(\mathbf{r})\, a_j \tag{1.6}$$

The advantage of this representation is that it allows to naturally introduce the so-called Bogoliubov approximation, which consists in replacing the operators a_0 and $a_0^\dagger$ with the c-number $\sqrt{N_0}$. This is equivalent to neglecting the non-commutativity of a_0 and $a_0^\dagger$, which is reasonable when dealing with Bose-Einstein condensation, where the occupation number $N_0 = \langle a_0^\dagger a_0 \rangle$ is large. Indeed, the commutator between a_0 and $a_0^\dagger$ is equal to 1, while the operators themselves are of the order of $\sqrt{N_0}$. Equation (1.6) then becomes

$$\psi(\mathbf{r}) = \psi_0(\mathbf{r}) + \delta\psi(\mathbf{r}) \tag{1.7}$$

where we have defined $\psi_0 = \sqrt{N_0}\varphi_0$ and $\delta\psi = \sum_{j \neq 0} \varphi_j a_j$. In the case of a dilute weakly interacting Bose gas at very low temperatures the non-condensate component $\delta\psi$ is negligible, and the system can be described by means of the classical field ψ_0 only, which hereafter will be referred to as the condensate wave function or the order parameter. It is characterized by a modulus and a phase

$$\psi_0(\mathbf{r}) = |\psi_0(\mathbf{r})| \mathrm{e}^{\mathrm{i}S(\mathbf{r})} \tag{1.8}$$

where the modulus determines the particle density $n(\mathbf{r}) = |\psi_0(\mathbf{r})|^2$ of the condensate while the phase characterizes the coherence and superfluid phenomena. The condensate wave function is normalized to the total number of particles, $\int d\mathbf{r}|\psi_0(\mathbf{r})|^2 = N_0 = N$. The order parameter ψ_0 characterizes the Bose-Einstein condensed phase, and vanishes above the critical temperature needed for the condensation to occur. The Hamiltonian of Eq. (1.3) is invariant for $\psi \to \psi e^{i\phi}$ ($U(1)$ symmetry). This is the manifestation of gauge symmetry of the problem: in the BEC phase transition, a condensate spontaneously chooses a particular phase. Making an explicit choice for the phase is referred to as a spontaneous breaking of the gauge symmetry and, according to Goldstone theorem, this implies that the condensed phase has a gapless mode (see Section 2.2).

The Bogoliubov ansatz, Eq. (1.7), for the field operator can be interpreted by saying that the expectation value $\langle\psi\rangle$ of the field operator is different from zero. Of course, this statement is not correct if the states on the left and on the right had exactly the same number of particles. Its exact meaning can be explained as follows: since the occupation number N_0 is much greater than 1, adding one single particle to the condensate does not affect the physical properties of the system. Therefore, a state $|N\rangle$ is in practice physically equivalent to the states $|N+1\rangle \propto a_0^\dagger|N\rangle$ and $|N-1\rangle \propto a_0|N\rangle$. Thus, it makes sense to write $\psi_0 = \langle\psi\rangle$, provided that the states on the left have one less particle than the states on the right. From a quantum field theoretical point of view, the condensate is in a coherent state defined by

$$\hat{a}|\alpha\rangle = \alpha|\alpha\rangle \tag{1.9}$$

where $|\alpha|^2 = N_0$ is the average particle number in the condensate. The coherent state $|\alpha\rangle$ can also be expanded in particle number eigenstates as

$$|\alpha\rangle = \sum_n \frac{e^{-|\alpha|^2/2}}{\sqrt{n!}}\alpha^n|n\rangle. \tag{1.10}$$

This allows to consider the replacement of ψ by ψ_0 as a mean-field approximation, which is essentially the analogue of the classical limit of quantum electrodynamics, where the classical electromagnetic field entirely replaces the microscopic description in terms of photons.

In order to derive the equation governing the field ψ_0 we first switch to the Heisenberg picture. In this representation the quantum field $\psi(\mathbf{r}, t)$ fulfils the exact equation

$$\begin{aligned} i\hbar\frac{\partial}{\partial t}\psi(\mathbf{r}, t) &= \left[\psi(\mathbf{r}, t), H\right] \\ &= \left[-\frac{\hbar^2\nabla^2}{2m} + V_{ext}(\mathbf{r}) + \int d\mathbf{r}'\psi^\dagger(\mathbf{r}', t)\mathcal{V}(\mathbf{r}' - \mathbf{r})\psi(\mathbf{r}', t)\right]\psi(\mathbf{r}, t). \end{aligned} \tag{1.11}$$

The next step is to get rid of the field operators ψ and substitute them with ψ_0 however, for a realistic interatomic potential $\mathcal{V}$, such a replacement is not generally correct. Indeed, a realistic potential always contains a short-range term which varies rapidly at distances of the order of r_0, thus making quantum correlations important. However, in virtue of the above discussion on the diluteness criteria, we know that the actual form of the two-body potential is not important for describing the macroscopic properties of the gas, the only relevant parameter being the s-wave scattering length. As a consequence, one can replace the bare potential by an effective potential

$$\mathcal{V}_{\text{eff}}(\mathbf{r}' - \mathbf{r}) = g\delta(\mathbf{r}' - \mathbf{r}) \tag{1.12}$$

where the coupling constant g is related to the s-wave scattering length a through

$$g = \frac{4\pi\hbar^2 a}{m}. \tag{1.13}$$

Hence, we can legitimately make the simultaneous replacement of ψ by ψ_0 and of $\mathcal{V}$ by $\mathcal{V}_{\text{eff}}$, and Equation (1.11) becomes

$$\mathrm{i}\hbar\frac{\partial}{\partial t}\psi_0(\mathbf{r},t) = \left(-\frac{\hbar^2\nabla^2}{2m} + V_{\text{ext}}(\mathbf{r}) + g|\psi_0(\mathbf{r},t)|^2\right)\psi_0(\mathbf{r},t). \tag{1.14}$$

Equation (1.14) corresponds to the well-known time-dependent Gross-Pitaevskii equation for the order parameter of the condensate. It was derived independently by Gross [26] and Pitaevskii [27], and it is the main theoretical tool for investigating non-uniform weakly interacting dilute Bose gases at low temperatures. The Gross-Pitaevskii equation has the typical form of a mean-field equation, where the order parameter must be calculated in a self-consistent way. Its validity has been rigorously proved by Lieb, Seiringer, Solovej and Yngvason in [28].

It is worth mentioning that the GP equation, Eq. (1.14), can also be obtained using a variational procedure. In fact, by imposing the stationarity condition

$$\delta\left[\int \mathrm{d}t\,\mathrm{d}\mathbf{r}\left(-\mathrm{i}\hbar\psi_0^*\frac{\partial}{\partial t}\psi_0\right) + \int \mathrm{d}t\,E\right] = 0 \tag{1.15}$$

to the action, one obtains the equation

$$\mathrm{i}\hbar\frac{\partial\psi_0}{\partial t} = \frac{\delta E}{\delta\psi_0^*} \tag{1.16}$$

for the order parameter, where the energy functional E is given by

$$E[\psi_0] = \int \mathrm{d}\mathbf{r}\,\left[\frac{\hbar^2}{2m}|\nabla\psi_0|^2 + V_{\text{ext}}(\mathbf{r})|\psi_0|^2 + \frac{g}{2}|\psi_0|^4\right]. \tag{1.17}$$

Let we now consider a stationary, zero-temperature condensate described by the Gross-Pitaevskii equation, Eq. (1.14). For such a system the condensate density is time invariant and the wave function evolution consist solely of a spatially uniform phase rotation due to the condensate's energy. Hence we can separate the time-dependent condensate wave function using the usual ansatz

$$\psi_0(\mathbf{r}, t) = \psi_0(\mathbf{r}) \mathrm{e}^{-\mathrm{i}\mu t/\hbar}, \tag{1.18}$$

where $\psi_0(\mathbf{r})$ is now the time-independent condensate wave function and μ is the characteristic energy of the condensate whose meaning will be discussed below. Applying this ansatz to the Gross-Pitaevskii equation, Eq. (1.14), we straightforwardly arrive at the time-independent Gross-Pitaevskii equation

$$\left(-\frac{\hbar^2\nabla^2}{2m} + V_{\mathrm{ext}}(\mathbf{r}) + g\left|\psi_0(\mathbf{r})\right|^2\right)\psi_0(\mathbf{r}) = \mu\psi_0(\mathbf{r}), \tag{1.19}$$

To ensure consistency between these two equations, Eqs. (1.14)-(1.19), μ must be the condensate chemical potential. Indeed the wave function phase factor reflects the fact that microscopically ψ_0 is equal to the matrix element of the annihilation operator ψ between the ground state with N particles and that with $N-1$ particles,

$$\psi_0(\mathbf{r}, t) = \langle N-1|\psi(\mathbf{r})|N\rangle \propto \exp\left[-\mathrm{i}(E_N - E_{N-1})\, t/\hbar\right]. \tag{1.20}$$

For large N the difference in ground state energies for states with N and $N-1$ particles is equal to $\partial E/\partial N$ which is exactly the chemical potential. The chemical potential μ is fixed by imposing the normalization of the wave function to the total number of particles, $\int \mathrm{d}\mathbf{r}\, |\psi_0(\mathbf{r})|^2 = N$.

Equation (1.19) has the form of a non-linear Schrödinger equation, with the non-linearity coming from the mean-field term, proportional to the particle density. In the absence of interactions ($g = 0$), this equation reduces to the usual Schrödinger equation for the single-particle Hamiltonian $-\hbar^2\nabla^2/(2m) + V_{\mathrm{ext}}(\mathbf{r})$, and the condensate wave function becomes equal, up to a factor $\sqrt{N}$, to the corresponding ground-state wave function.

1.2 BEC mixtures

For a weakly interacting mixture of two Bose-Einstein condensed gases the theoretical description can be derived through a natural generalization of the Gross-Pitaevskii equation, Eq. (1.14), each condensate being described by its own wave function. The first

theoretical work on binary mixtures was provided by Ho and Shenoy [29]. Considerations similar to the ones developed in last Section yield to the following expression for the energy of the mixture of two Bose-Einstein condensates:

$$E = \int \mathrm{d}\mathbf{r} \left[\frac{\hbar^2}{2m_a}|\nabla\psi_a|^2 + \frac{\hbar^2}{2m_b}|\nabla\psi_b|^2 + V_a^{\mathrm{ext}}|\psi_a|^2 + V_b^{\mathrm{ext}}|\psi_b|^2 + \right. \\ \left. + \frac{1}{2}g_a|\psi_a|^4 + \frac{1}{2}g_b|\psi_b|^4 + g_{ab}|\psi_a|^2|\psi_b|^2 \right], \tag{1.21}$$

where ψ_a and ψ_b are the wave functions for the two components of the mixture, with masses m_a and m_b respectively, which are subjected to the external potentials $V_a^{\mathrm{ext}}(\mathbf{r})$ and $V_b^{\mathrm{ext}}(\mathbf{r})$. The coupling constants $g_a = 4\pi\hbar^2 a_a/m_a$ and $g_b = 4\pi\hbar^2 a_b/m_b$ are fixed by the scattering lengths a_a and a_b, while $g_{ab} = 2\pi\hbar^2 a_{ab}/m_r$ with $1/m_r = 1/m_a + 1/m_b$ is determined by the scattering length a_{ab} where an atom in the state a scatters with an atom in the state b.

Equation (1.21) for the energy functional ignores the possible coupling between the velocity fields of the two fluids, which lead to physical phenomena such as the Andreev-Bashkin effect [5]. This effect is however small in weakly interacting gases [6].

The coupled Gross-Pitaevskii equations can be derived from the variational principle $\mathrm{i}\hbar\partial\psi_\sigma/\partial t = \delta E/\delta\psi_\sigma^*$ with $\sigma = a, b$. One finds:

$$\mathrm{i}\hbar\frac{\partial}{\partial t}\psi_a = \left(-\frac{\hbar^2\nabla^2}{2m_a} + V_a^{\mathrm{ext}}(\mathbf{r}) + g_a|\psi_a|^2 + g_{ab}|\psi_b|^2\right)\psi_a, \tag{1.22}$$

$$\mathrm{i}\hbar\frac{\partial}{\partial t}\psi_b = \left(-\frac{\hbar^2\nabla^2}{2m_b} + V_b^{\mathrm{ext}}(\mathbf{r}) + g_b|\psi_b|^2 + g_{ab}|\psi_a|^2\right)\psi_b, \tag{1.23}$$

or, in the time-independent version,

$$\mu_a\psi_a = \left(-\frac{\hbar^2\nabla^2}{2m_a} + V_a^{\mathrm{ext}}(\mathbf{r}) + g_a|\psi_a|^2 + g_{ab}|\psi_b|^2\right)\psi_a, \tag{1.24}$$

$$\mu_b\psi_b = \left(-\frac{\hbar^2\nabla^2}{2m_b} + V_b^{\mathrm{ext}}(\mathbf{r}) + g_b|\psi_b|^2 + g_{ab}|\psi_a|^2\right)\psi_b, \tag{1.25}$$

where the two chemical potentials μ_a and μ_b are in principle different and fixed by the normalization of the wave functions, $\int \mathrm{d}\mathbf{r}|\psi_\sigma(\mathbf{r})|^2 = N_\sigma$, $\sigma = a, b$.

As we will see in the next chapter the system has two gapless Goldstone modes that correspond to the fact that there is no cost for changing the phase of the two wave functions ψ_a and ψ_b.

1.3 Coherently coupled Bose-Einstein condensates

Equations (1.22)-(1.23) conserve the numbers of atoms of each component. However, the application of an oscillating radio frequency (*rf*) field tuned close to the hyperfine splitting $V_{\rm hf}$ can result in the possibility of transfer of atoms from one state to the other. In this situation the wave function of the system becomes a vector with a component for each hyperfine level,

$$\psi = \begin{pmatrix} \psi_a \\ \psi_b \end{pmatrix}, \tag{1.26}$$

and it can be described by adding a term proportional to ψ_a to the equation for ψ_b and vice versa. In the rotating wave approximation we find

$$\mathrm{i}\hbar\frac{\partial}{\partial t}\psi_a = \left(-\frac{\hbar^2\nabla^2}{2m_a} + V_{\rm ext}(\mathbf{r}) + g_a|\psi_a|^2 + g_{ab}|\psi_b|^2\right)\psi_a - \Omega(t)\,\mathrm{e}^{\mathrm{i}\omega_{rf}t}\psi_b \tag{1.27}$$

$$\mathrm{i}\hbar\frac{\partial}{\partial t}\psi_b = \left(-\frac{\hbar^2\nabla^2}{2m_b} + V_{\rm ext}(\mathbf{r}) + V_{\rm hf} + g_b|\psi_b|^2 + g_{ab}|\psi_a|^2\right)\psi_b - \Omega^*(t)\,\mathrm{e}^{-\mathrm{i}\omega_{rf}t}\psi_a \tag{1.28}$$

where ω_{rf} is the frequency of the *rf* wave and the Rabi energy $\Omega(t)$ plays the role of the coupling constant for the transition. Notice that the phase of Ω defining the phase of the *rf* field is arbitrary. In the following Ω will be assumed real and positive. For simplicity, we have assumed that the external potential felt by the two spin components is the same, apart from the hyperfine splitting $V_{\rm hf}$ fixed by the magnetic field.

Notice that the physical meaning of the amplitude Ω is different for different types of transitions. If the transfer can be obtained via one-photon transitions, Ω is proportional to the field amplitude. However, in other cases the transition requires two units of angular momentum and can be activated only with two-photon transitions. In this case the amplitude Ω is quadratic in the *rf* field.

The application of this radio frequency field is useful not only to add new features and to enrich the physics of the mixture (as we will see in following Chapters) but also for creating the initial desired population unbalance in the system. This is done using the following procedure. Starting from a configuration where all the atoms are in the state $|a\rangle$ (and hence $\psi = \begin{pmatrix}\sqrt{n_0} & 0\end{pmatrix}$) an *rf* pulse of short duration will bring some atoms into the state $|b\rangle$ without changing their space distribution. In this case one can write the solutions of the Gross-Pitaevskii equations in the form

$$\psi(\mathbf{r},t) = \begin{pmatrix} \psi_a(\mathbf{r},t) \\ \psi_b(\mathbf{r},t) \end{pmatrix} = \begin{pmatrix} A_a(t)\sqrt{n_0(\mathbf{r})} \\ A_b(t)\sqrt{n_0(\mathbf{r})} \end{pmatrix}. \tag{1.29}$$

By further assuming $g_a \sim g_b \sim g_{ab}$, the equation for the amplitudes A becomes

$$i\hbar \frac{d}{dt}\begin{pmatrix} A_a \\ A_b \end{pmatrix} = \begin{pmatrix} \mu_a & -\Omega e^{i\omega_{rf}t} \\ -\Omega e^{i\omega_{rf}t} & \mu_b \end{pmatrix}\begin{pmatrix} A_a \\ A_b \end{pmatrix} \tag{1.30}$$

where μ_a and $\mu_b = \mu_a + V_{\rm hf}$ are the chemical potentials of the two components. For brief pulses of duration t such that $t \gg 1/\delta$, where $\delta = \omega_{rf} - V_{\rm hf}/\hbar \ll V_{\rm hf}/\hbar$, the solution takes the form

$$A_a(t) = e^{-i\mu_a t/\hbar}\left(C_1 e^{-i\Omega t/\hbar} + C_2 e^{+i\Omega t/\hbar}\right), \tag{1.31}$$

$$A_b(t) = e^{-i\mu_b t/\hbar}\left(-C_1 e^{-i\Omega t/\hbar} + C_2 e^{+i\Omega t/\hbar}\right) \tag{1.32}$$

where C_1 and C_2 are fixed by the initial conditions ($C_1 = C_2 = 1/2$ in our case). Then, after the time $\tau = (\pi/2)(\hbar/2\Omega)$ ("$\pi/2$ pulse"), one gets $|A_a|^2 = |A_b|^2 = 1/2$ and the atoms will be equally distributed between the two hyperfine states. A pulse of double duration ("π pulse") will instead convert completely the system from the state $|a\rangle$ into $|b\rangle$.

However, if the π pulse is split into two $\pi/2$ pulses with an intermediate time delay t_0, the wave functions of the condensates, after the first pulse, will evolve according to the laws $A_a \sim e^{-i\mu_a t/\hbar}$ and $A_b \sim e^{-i\mu_b t/\hbar}$. As a consequence, after the time t_0, the relative phase between the two condensates has varied by the amount $(\mu_a - \mu_b)t_0/\hbar$. On the other hand, in the same time interval also the phase of the coupling field has evolved by the amount $\omega_{rf}t_0$. One can see that the fraction of atoms that, after the second $\pi/2$ pulse, will be converted to the state $|b\rangle$, is given by

$$N_b = \frac{N}{2}\left\{1 + \cos\left[\left(\omega_{rf} - \frac{\mu_a - \mu_b}{\hbar}\right)t_0\right]\right\} \tag{1.33}$$

Since the difference between the two chemical potentials coincides with the hyperfine splitting ($\mu_a - \mu_b = V_{\rm hf}$), the frequency of the oscillation is given by the detuning $\delta = \omega_{rf} - V_{\rm rf}/\hbar$.

It is also interesting to discuss the solutions of the Gross-Pitaevskii equations, Eqs. (1.27)- (1.28), in the presence of stationary *rf* coupling between the two hyperfine states. To this purpose it is convenient to introduce a unitary transformation yielding $\psi_a \rightarrow e^{-i\omega_{rf}t/2}\psi_a$ and $\psi_b \rightarrow e^{+i\omega_{rf}t/2}\psi_b$, corresponding to a rotation in spin space around the third spin axis by the angle $\omega_{rf}t$. The new Hamiltonian in the rotated frame becomes time independent and, choosing the *rf* frequency equal to the hyperfine splitting ($\hbar\omega_{rf} =$

V_{hf}), the Gross-Pitaevskii equations take the form

$$\mathrm{i}\hbar\frac{\partial}{\partial t}\psi_a = \left(-\frac{\hbar^2\nabla^2}{2m} + V_{\mathrm{ext}}(\mathbf{r}) + g_a|\psi_a|^2 + g_{ab}|\psi_b|^2\right)\psi_a - \Omega\psi_b \tag{1.34}$$

$$\mathrm{i}\hbar\frac{\partial}{\partial t}\psi_b = \left(-\frac{\hbar^2\nabla^2}{2m} + V_{\mathrm{ext}}(\mathbf{r}) + g_b|\psi_b|^2 + g_{ab}|\psi_a|^2\right)\psi_b - \Omega\psi_a \tag{1.35}$$

These equations can be also derived starting from the energy functional, Eq. (1.21), containing the additional *rf* term

$$E_\Omega = -\Omega\int \mathrm{d}\mathbf{r}\,\left(\psi_a^*\psi_b + \psi_b^*\psi_a\right) = -2\Omega\int \mathrm{d}\mathbf{r}\,|\psi_a||\psi_b|\cos(\phi_b - \phi_a), \tag{1.36}$$

which depends explicitly on the relative phase $(\phi_b - \phi_a)$ between the two order parameters.

Also in this case we can easily derive the time-independent version of GP equations:

$$\mu\psi_a = \left(-\frac{\hbar^2\nabla^2}{2m} + V_{\mathrm{ext}}(\mathbf{r}) + g_a|\psi_a|^2 + g_{ab}|\psi_b|^2\right)\psi_a - \Omega\psi_b \tag{1.37}$$

$$\mu\psi_b = \left(-\frac{\hbar^2\nabla^2}{2m} + V_{\mathrm{ext}}(\mathbf{r}) + g_b|\psi_b|^2 + g_{ab}|\psi_a|^2\right)\psi_b - \Omega\psi_a. \tag{1.38}$$

Now, because of the presence of the Rabi coupling Ω, only the total number of particles N_{tot} is conserved and the spinor wave function is characterized by a single chemical potential μ fixed by its normalization to $N_{tot} = \int \mathrm{d}\mathbf{r}\left(|\psi_a(\mathbf{r})|^2 + |\psi_b(\mathbf{r})|^2\right)$.

As we will see in Section 2.2 the system has one gapless Goldstone mode corresponding to the fact that there is no cost to change the global phase of the spinor and one gapped mode corresponding to the energy cost that must be paid for changing the relative phase, see Eq. (1.36).

CHAPTER

2 Homogeneous gas

In this chapter we investigate the different ground states and the dynamics of a Bose-Bose mixture in an homogeneous external potential. In particular we first show the different phases this system can exhibit with or without the Rabi coupling: miscible vs. immiscible and paramagnetic vs. ferromagnetic regimes. We then describe its excitations focusing on the differences between density and spin modes and finally we address the problem of persistent currents in a BEC mixture: we derive a criterion for their stability and we check it by means of imaginary- and real-time simulations of the Gross-Pitaevskii equations.

Contents

Trapping cold atoms in a box-shaped external potential is not so simple. Only recently, thanks to the use of dark optical traps and phase-imprinting spatial light modulators (SLM), the condensation of an atomic gas in a three dimensional (quasi)uniform potential has become possible [30]. Most of the experiments are thus done with harmonic-shaped trapping potentials. Despite that, we first discuss homogeneous systems not only because they are simpler to study but also because most of the characteristics we will encounter here can be retrieved in the case of trapped mixtures be means of Local Density Approximation (LDA).

2.1 Ground state phases

2.1.1 $\Omega = 0$, miscible vs. immiscible phase

We start our analysis from the easiest situation in which there is no Rabi coupling between the two components, $\Omega = 0$.

In this case the ground state can be either a uniform mixture of the two components, or phase separated. The condition for the miscibility can be easily established investigating the energies of the two configurations in the homogeneous case (see Equation (1.21) of Chapter 1):

$$E_{\text{unif}} = \frac{g_a}{2}\frac{N_a^2}{V} + \frac{g_b}{2}\frac{N_b^2}{V} + g_{ab}\frac{N_a N_b}{V} \tag{2.1}$$

$$E_{\text{separ}} = \frac{g_a}{2}\frac{N_a^2}{V_a} + \frac{g_b}{2}\frac{N_b^2}{V_b} \tag{2.2}$$

where V_a and V_b are the volumes occupied by the two separated phases and $V_a + V_b = V$. To ensure the mechanical equilibrium between the two phases they must satisfy the condition $\partial E_{\text{separ}}/\partial V_a = \partial E_{\text{separ}}/\partial V_b$ that implies the relationship $g_a(N_a/V_a)^2 = g_b(N_b/V_b)^2$. Using this last expression we can rewrite the phase separation energy, Eq. (2.2), in a more suitable form:

$$E_{\text{separ}} = \frac{g_a}{2}\frac{N_a^2}{V} + \frac{g_b}{2}\frac{N_b^2}{V} + \sqrt{g_a g_b}\frac{N_a N_b}{V}. \tag{2.3}$$

So, comparing Equation (2.1) with Equation (2.3), we see that, in order to have phase separation ($E_{\text{separ}} < E_{\text{unif}}$), we must require [31]

$$g_{ab} > \sqrt{g_a g_b}. \tag{2.4}$$

At the critical value the system undergoes a first order phase transition creating two regions in which only one component of the gas is present separated by a domain wall (for a detailed discussion see [32, 29, 33]).

2.1.2 $\Omega \neq 0$, paramagnetic vs. ferromagnetic phase

When the Rabi coupling is switched on the energy per unit volume is

$$e(n_a, n_b) = \frac{1}{2} g_a {n_a}^2 + \frac{1}{2} g_b {n_b}^2 + g_{ab} n_a n_b + 2|\Omega| \cos\phi \sqrt{n_a n_b} - \mu(n_a + n_b) \tag{2.5}$$

where we have rewritten the spinor components wave functions in terms of densities n_σ and phases ϕ_σ, $\psi_\sigma = \sqrt{n_\sigma} e^{i\phi_\sigma}$, and we have introduced the phase $\phi \equiv \phi_r + \phi_\Omega$ in terms of the phase difference $\phi_r = \phi_b - \phi_a$ and the phase of the Rabi coupling defined by $\Omega = |\Omega| e^{i\phi_\Omega}$.

The ground state of the system [34, 15, 35, 36] is given by the values of densities and phases which minimize this energy. This configuration corresponds to $\cos\phi = -1$. For Ω real ($\phi_\Omega = 0, \pi$) this means $\phi_r = \pi$ for $\Omega > 0$ and $\phi_r = 0$ for $\Omega < 0$; for Ω complex, the equilibrium value of ϕ_r is such that $\phi_r + \phi_\Omega = (2l+1)\pi$ with $l \in \mathbb{Z}$. Notice that the condition $\cos\phi = +1$ can give rise to an extremum of the energy [34, 37, 38] but it will never be the global minimum (in fact it is a saddle-point in the energy landscape). In the following, without any loss of generality, we assume Ω to be real and positive that implies $\phi_r = \pi$.

The structure of the ground state is better understood in the $\mathbb{Z}_2$ symmetric case $g_a = g_b \equiv g$ and, since the total density n is fixed, the equilibrium configuration is characterised by the density difference or polarization $P = (n_a - n_b)/n$. Neglecting the gradient term and subtracting the two GP equations, Eqs. (1.37)-(1.38), we get a simple relation the equilibrium solutions must satisfy:

$$\left(g - g_{ab} + \frac{\Omega}{\sqrt{n_a n_b}} \right) (n_a - n_b) = 0. \tag{2.6}$$

The latter equation admits two possible solutions

$$\text{(GSU)} \quad (n_a - n_b) = 0, \tag{2.7}$$

$$\text{(GSP)} \quad (n_a - n_b)_\pm = \pm n \sqrt{1 - \left(\frac{2|\Omega|}{(g - g_{ab})n} \right)^2}; \tag{2.8}$$

corresponding to an unpolarized (GSU) and to a polarized (GSP) ground state. Introducing the critical interspecies interaction value as $\bar{g}_{ab} = g + 2\Omega/n$ one can easily find that the energetically favoured state is GSU when $g_{ab} < \bar{g}_{ab}$ and GSP for $g_{ab} > \bar{g}_{ab}$.

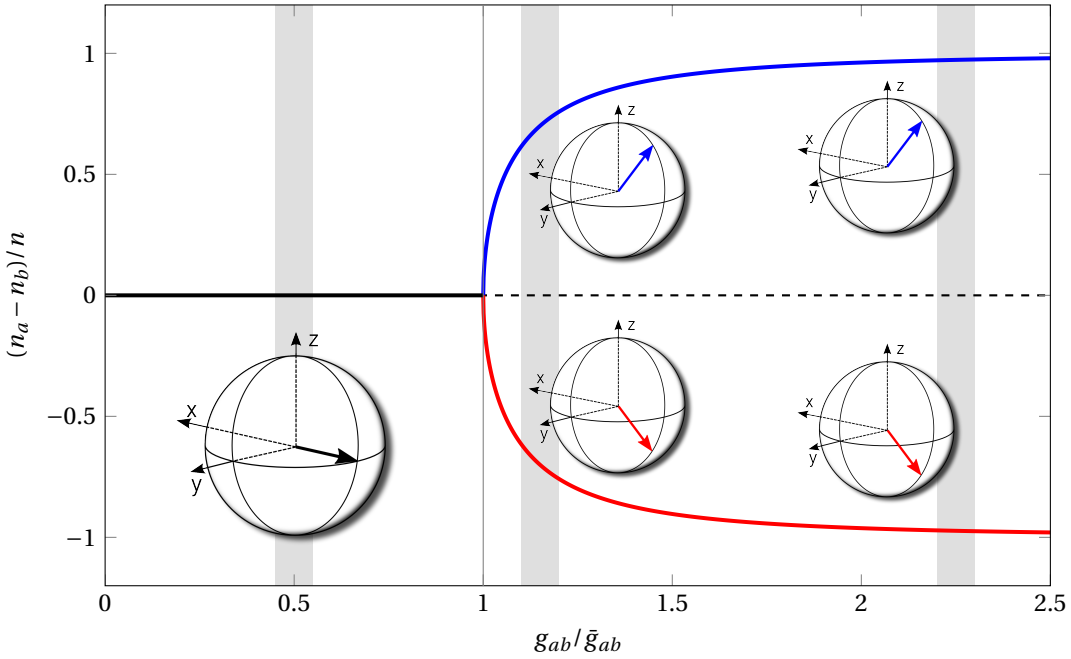

FIGURE 2.1: Polarization of the condensate as a function of the interspecies interaction g_{ab} with $\Omega = 0.3gn$. Insets: Bloch sphere representation, the Rabi coupling tries to maintain the spinor order parameter in the x-y plane, while the unbalance between inter- and intra-species interaction favour a non zero projection along the z axis, i.e. a finite polarization.

As shown in Fig. 2.1, at the critical point $g_{ab} = \bar{g}_{ab}$ there exists a bifurcation in the ground state solutions which hints a second-order phase transition. This bifurcation has been measured experimentally by M. Oberthaler group, see Ref. [8]. This phase transition is very different from the miscible-immiscible one occurring in the mixture without Rabi coupling. In the latter the presence of coherent coupling shifts the critical point to higher values of interspecies interaction and prevents phase separation by instead creating a finite polarization.

2.2 Excitations: density vs. spin modes

The whole spectrum of the system is captured using a Bogoliubov approach. To address small amplitude excitations above the ground state we write the time-dependent order parameter as

$$\Psi_\sigma(\mathbf{r}, t) = \mathrm{e}^{-\mathrm{i}\mu t/\hbar}\left[\psi_\sigma + \mathrm{e}^{\mathrm{i}\phi_\sigma}\delta\Psi_\sigma(\mathbf{r}, t)\right], \tag{2.9}$$

with μ the chemical potential of the complete system, ψ_σ the ground state wave functions $\psi_\sigma = \sqrt{n_\sigma}e^{i\phi_\sigma}$ and $\sigma = a, b$. Since we are dealing with an homogeneous system we can write the perturbations $\delta\Psi_\sigma$ as plane waves with complex amplitudes u_σ and v_σ,

$$\delta\Psi_\sigma = u_\sigma e^{i(\mathbf{k}\cdot\mathbf{r}-\omega t)} \tag{2.10}$$

$$\delta\Psi^*_\sigma = v_\sigma e^{i(\mathbf{k}\cdot\mathbf{r}-\omega t)}. \tag{2.11}$$

After some algebra an eigenvalue equation is reached

$$\hbar\omega \begin{pmatrix} u_a \\ v_a \\ u_b \\ v_b \end{pmatrix} = \mathscr{L} \begin{pmatrix} u_a \\ v_a \\ u_b \\ v_b \end{pmatrix}, \tag{2.12}$$

where the linear operator $\mathscr{L}$ is given by

$$\mathscr{L} = \begin{pmatrix} h_a & g_a n_a & g_{ab}\sqrt{n_a n_b} - |\Omega| & g_{ab}\sqrt{n_a n_b} \\ -g_a n_a & -h_a & -g_{ab}\sqrt{n_a n_b} & -g_{ab}\sqrt{n_a n_b} + |\Omega| \\ g_{ab}\sqrt{n_a n_b} - |\Omega| & g_{ab}\sqrt{n_a n_b} & h_b & g_b n_b \\ -g_{ab}\sqrt{n_a n_b} & -g_{ab}\sqrt{n_a n_b} + |\Omega| & -g_b n_b & -h_b \end{pmatrix} \tag{2.13}$$

and we have defined

$$h_a = \frac{\hbar^2 k^2}{2m} + 2g_a n_a + g_{ab} n_b - \mu_a \tag{2.14}$$

$$h_b = \frac{\hbar^2 k^2}{2m} + 2g_b n_b + g_{ab} n_a - \mu_b \tag{2.15}$$

$$\mu \equiv \mu_a = \mu_b = \frac{1}{2}\left[g_a n_a + g_b n_b + g_{ab} n - \frac{n}{\sqrt{n_a n_b}}|\Omega| \right] \quad \text{for } \Omega \neq 0 \tag{2.16}$$

$$\mu_a = g_a n_a + g_{ab} n_b \quad \text{for } \Omega = 0 \tag{2.17}$$

$$\mu_b = g_b n_b + g_{ab} n_a \quad \text{for } \Omega = 0 \tag{2.18}$$

In order to obtain the main characteristics of the dispersions it is easiest to take equal intraspecies interactions, $g_a = g_b \equiv g$. We start analysing excitations above the symmetric unpolarized ground state GSU which corresponds to $n_a = n_b = n/2$ as shown in Fig. 2.1. In this situation the solutions, that clearly exist only for $g_{ab} < g + 2\Omega/n$, take the

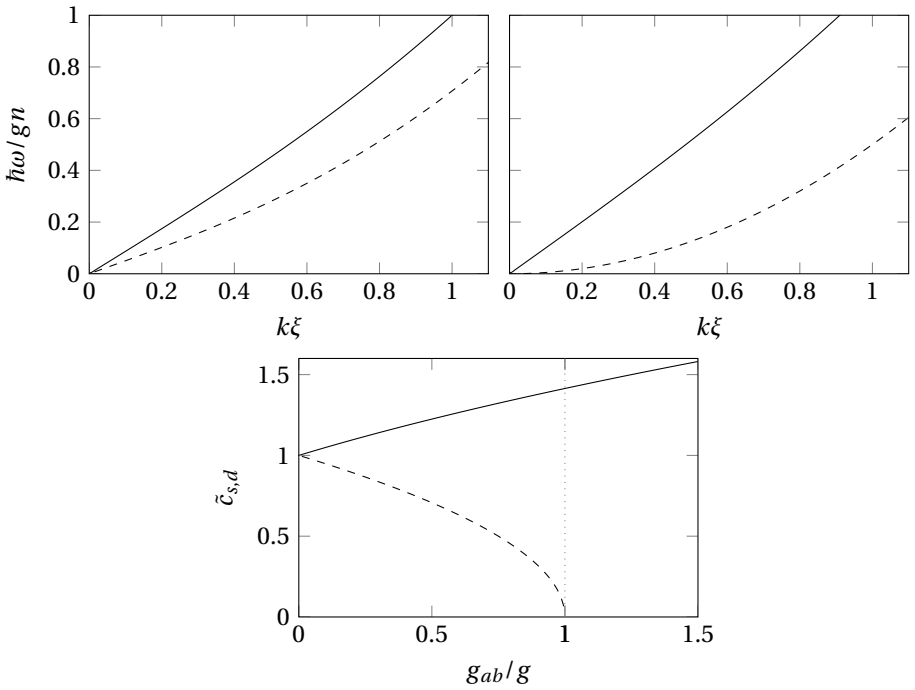

FIGURE 2.2: Upper panels: dispersion relations for $\Omega = 0$, density (full line) and spin mode (dashed line) for $g_{ab} = 0.5g$ (left panel) and $g_{ab} = g$ (right panel). Lower panel: density (full line) and spin (dashed line) speed of sound as a function of g_{ab}/g, dotted line represents the phase separation point. $\xi = \hbar/\sqrt{mgn}$ is the healing length and $\tilde{c} = (\sqrt{2m/gn})c$vis the speed of sound in adimensional units.

form [39]:

$$\hbar\omega_d = \sqrt{\frac{\hbar^2k^2}{2m}\left[\frac{\hbar^2k^2}{2m} + (g+g_{ab})n\right]} \tag{2.19}$$

$$\hbar\omega_s = \sqrt{\frac{\hbar^2k^2}{2m}\left[\frac{\hbar^2k^2}{2m} + (g-g_{ab})n + 4|\Omega|\right] + 2|\Omega|\left[(g-g_{ab})n + 2|\Omega|\right]} \tag{2.20}$$

2.2.1 $\Omega = 0$, normal mixture

When $\Omega = 0$ we get two Bogoliubov-like dispersion relations, linear at low k and quadratic at high k (see upper left panel of Fig. 2.2). These two modes, hereafter called respectively density and spin, are the dispersion laws in which the two components of the system moves in phase (Eq. 2.19) or counterphase (Eq. 2.20). They represent the two gapless Goldstone modes due to the breaking of the U(1) × U(1) symmetry possessed by the system. The linear slopes are different for density and spin excitations and are given by the

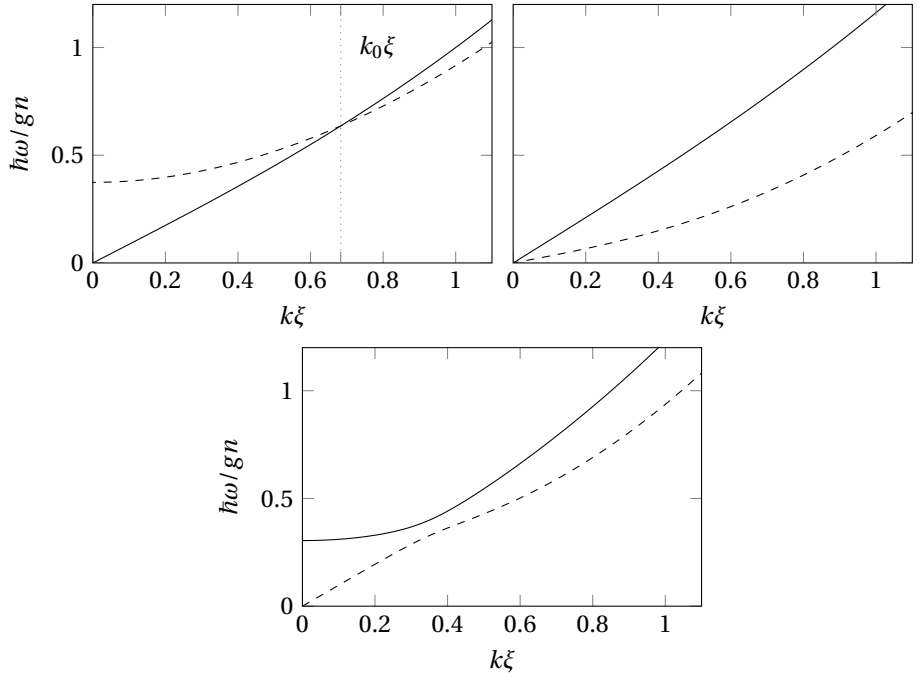

FIGURE 2.3: Dispersion relations for $\Omega \neq 0$: density (full line) and spin mode (dashed line). Upper left panel: below the transition, above the unpolarized ground state (GSU), with $g_{ab} = 0.5g$ and $\Omega = 0.1gn$. Upper right panel: at the transition point, with $g_{ab} = 1.2g$ and $\Omega = 0.1gn$. Lower panel: above the transition, above the polarized ground state (GSP), with $g_{ab} = 1.3g$ and $\Omega = 0.02gn$. Dotted line represents the position of the crossing point k_0.

density and spin speeds of sound (see lower panel of Fig. 2.2),

$$
\begin{aligned}
{c_{d,s}}^2 &= \frac{{c_a}^2 + {c_b}^2}{2} \pm \frac{1}{2}\sqrt{{c_a}^4 + {c_b}^4 + 2{c_a}^2{c_b}^2\left(\frac{2{g_{ab}}^2}{g_a g_b} - 1\right)} \\
&= \frac{gn}{2m}\left(1 \pm \frac{g_{ab}}{g}\right) \quad \text{for } g_a = g_b \equiv g \text{ and } n_a = n_b = n/2
\end{aligned}
\tag{2.21}
$$

where ${c_\sigma}^2 = g n_\sigma / m$ and $\sigma = a, b$. At the demixing point $g = g_{ab}$, the spin speed of sound vanishes (see lower panel of Fig. 2.2) and the spin-sector becomes quadratic also at low k (see upper right panel of Fig. 2.2) underlining the first order phase transition between a mixed and a phase separated state taking place in the system.

2.2.2 $\Omega \neq 0$, spinor condensate

As shown in the upper left panel of Fig. 2.3, for $\Omega \neq 0$, the density sector, being the Goldstone mode related to the total particle number conservation, remains linear and gapless

at low k, it does not depend on Ω, see Eq. 2.19. In contrast, the frequency ω_s corresponds to a gapped spin mode with a $\sim k^2$ behaviour for $k \to 0$ above the gap

$$\hbar\omega_G = \sqrt{2|\Omega|\left[(g - g_{ab})n + 2|\Omega|\right]}. \tag{2.22}$$

In addition there is a crossing between the two branches at momentum

$$k_0 = \sqrt{\frac{2m|\Omega|}{\hbar^2}\left(\frac{g}{g_{ab} - 2|\Omega|/n} - 1\right)}. \tag{2.23}$$

Notice that k_0 exists only provided $g_{ab} < g + 2|\Omega|/n$ which is exactly the condition we discuss in the previous Section for GSU to be the lowest energy state. From the dispersion relations Eqs. (2.19) and (2.20) it is also clear that such an unpolarized phase can be stable against polarisation only if $g_{ab} < g + 2|\Omega|/n$.

As the critical condition is approached, the crossing occurs at lower k and the gap energy approaches zero. At the critical point the gap ω_G closes and the dispersion relation becomes linear at low k, as can be seen in upper right panel of Fig. 2.3. Such a behaviour is very different from the softening of the mode in the $\Omega = 0$ case at the demixing point because in that situation the spin-sector is gapless with a linear dispersion relation before the phase separation point and quadratic at phase transition.

Finally, for $g_{ab} > \bar{g}_{ab}$ the frequency ω_s (calculated above GSU) becomes imaginary, leading to instability, since the real ground state under this condition is the polarized one (GSP). In this case (as well as for $g_a \neq g_b$) due to $\mathbb{Z}_2$ symmetry breaking the crossing becomes an avoided crossing (lower panel of Fig. 2.3 and [34] for an analytical expression of the dispersion in the general case). Therefore a density (spin) mode at low momentum becomes a spin (density) mode after the avoided crossing. For the GSP the point where the avoided crossing occurs depends strongly on the specific location along the bifurcation curve [39].

2.3 Superfluid current stability

The evolution of experimental apparatuses and of experimental techniques has led to the possibility of trapping condensates in toroidal potentials [40, 41]. This has opened the doors to the creation and study of persistent currents in these systems. Persistent currents are dissipationless flows representing one of the strongest signatures of superfluidity. They are topological long-lived metastable states of quantum fluids which are

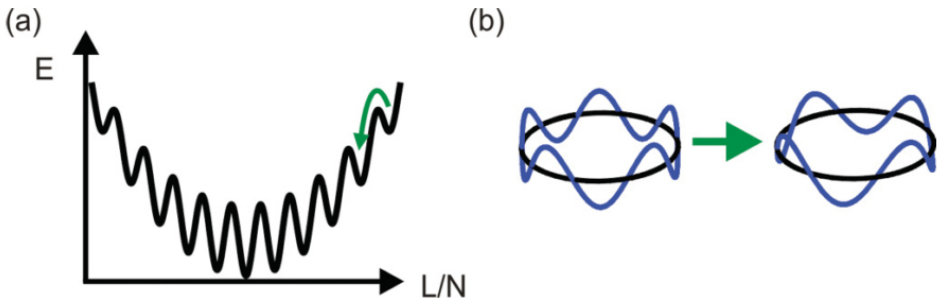

FIGURE 2.4: Metastability and decay of persistent currents. (a) Energy landscape of a superfluid gas in a ring. Local minima correspond to metastable states with quantized angular momentum. (b) Decay from a $q = 5$ state to a $q = 4$ state via a vortex-mediated phase slip. Figure taken from [41].

described by a macroscopic wave function (order parameter in Bose-Einstein condensates). The phase of this wave function must wind around the ring (torus) by an integer multiple of 2π, corresponding to the charge q of a vortex trapped inside the ring.

In Figure 2.4 we show qualitatively the physical origin of the supercurrent metastability. In general, for N atoms in a ring trap, the average angular momentum per particle does not need to be quantized but, when the system is superfluid this quantization becomes energetically preferred. In this situation the typical landscape of energy E as a function of angular momentum L has a parabolic behaviour with local minima corresponding to topologically distinct metastable states with $L/N = \hbar q$. Although the true ground state of the system corresponds to the global minimum $q = 0$, a current state with $q \neq 0$ can be extremely long-lived and almost immune to perturbations such as thermal fluctuations and disorder. A transition between two adjacent minima involves a 2π phase slip [41] in the condensate wave function and it occurs when a single charged vortex crosses the ring.

Persistent currents become unstable above a certain critical velocity (or equivalently above a certain critical q) [42] and their decay in the absence of a weak link is a complex, stochastic process related to the existence of barriers to the excitations to cross the bulk superfluid [43, 44, 45].

These currents have been studied for decades in liquid helium and solid states systems [46, 47, 48, 49]. More recently it has become possible to trap an atomic BEC in a ring geometry and induce rotational superflow in the system. This has opened the doors to a lot of experiments where both long-lived superflows [41, 50] and quantized phase slips

corresponding to vortices crossing the superfluid [41, 51] have been observed. These first experiments were limited to spinless, single-component condensates; only in the last few years they have been extended to multicomponent systems, essential for understanding superfluids with a vector order parameter and for applications in atom interferometry.

In particular, in a recent experiment of Z. Hadzibabic group [4], the stability of persistent currents in a toroidal two-component Bose gas was studied for different polarizations of the mixture. They drew the stability diagram of the system finding a critical polarization P_c below which currents decay very fast. In the opposite situation of high polarization the currents persist for over 2 minutes eventually disappearing due to total atom number decay.

Despite the growing number of experiment on these systems, the superfluid properties of BEC mixtures are still controversial, especially regarding the stability of persistent currents. Indeed, existing theoretical predictions [1, 52, 3, 53, 54] do not explain the recent experimental observations in [4]. Also, very recently the dynamics of the persistent currents have been numerically simulated using spin-1 Gross-Pitaevskii equations [55], but a deep theoretical understanding of the results in [4] is missing. Furthermore, arguments related to the continuous twisting of the order parameter can be applied neither to the mixture configuration nor in the presence of coherent coupling because in both cases the Hamiltonian is generally not invariant under $SU(2)$ transformations.

In order to get an insight in the problem we consider a 2-dimensional mixture in an external ring-shaped trapping potential. In particular, for better comparison with experiment [4], in all numerical simulations the potential is obtained as the sum of harmonic and Gaussian potentials,

$$V = \frac{1}{2} m {\omega_\perp}^2 r^2 + V_0 \mathrm{e}^{-2r^2/{\sigma_0}^2} \tag{2.24}$$

where $\omega_\perp$ is the radial trapping frequency, $r^2 = x^2 + y^2$ the radial coordinate, σ_0 the beam waist and V_0 the strength of the laser beam which is proportional to its intensity. The analytical results are instead obtained for a homogeneous ring potential of the form

$$V = \begin{cases} 0 & \text{if } R_0 - r_0 < r < R_0 + r_0 \\ V_0 & \text{otherwise.} \end{cases} \tag{2.25}$$

Different ring traps change the results quantitatively but not qualitatively.

To characterize the rotation of the condensates, we can use the mean value of the angular momentum along z, L_z, and the circulation, Γ. The first one has the advantage

of being independent on the circuit of integration, but the disadvantage of not being quantized if the system is not axially symmetric. The circulation, on the other hand, depends on the integration circuit but it is always quantized.

The angular momentum is given by

$$L_z = \langle\psi|\hat{L}_z|\psi\rangle = \int \mathrm{d}\,\mathbf{r}\psi^*\hat{L}_z\psi \tag{2.26}$$

with

$$\hat{L}_z = -\mathrm{i}\hbar\frac{\partial}{\partial\varphi} = -\mathrm{i}\hbar\left(x\frac{\partial}{\partial y} - y\frac{\partial}{\partial x}\right) \tag{2.27}$$

where φ is the azimuthal angle and the second form is the one used in the numerical code.

The circulation is given by

$$\Gamma = \oint \mathbf{v}\cdot\mathbf{d}l = \frac{\hbar}{m}\oint \nabla\phi\cdot\mathbf{d}l \tag{2.28}$$

where we have used the definition of the superfluid velocity in terms of the phase of the wave function, ϕ. It is easy to see that, in case of vortex-like solution, where $\phi = \kappa\varphi$, the circulation is quantized

$$\Gamma = \frac{\hbar}{m}\oint \frac{1}{r_\perp}\frac{\partial}{\partial\varphi}(\kappa\varphi)r_\perp \mathrm{d}\varphi = \frac{\kappa\hbar}{m}\oint \mathrm{d}\varphi = \frac{2\pi\kappa\hbar}{m} = \frac{h}{m}\kappa \tag{2.29}$$

where $r_\perp$ is the radius of the integration contour and we have taken an infinitesimal contour element $\mathrm{d}l = r_\perp \mathrm{d}\varphi\hat{e}_\varphi$. In contrast to the angular momentum, this result is independent of the density distribution. Numerically, if we are working in a Cartesian coordinate system, it is convenient to introduce a square circuit on the plane xy. If this square has vertices $ABCD$, we can write

$$\Gamma = \frac{\hbar}{m}\left[\int_A^B \frac{\partial\phi}{\partial x}\mathrm{d}x + \int_B^C \frac{\partial\phi}{\partial y}\mathrm{d}y - \int_C^D \frac{\partial\phi}{\partial x}\mathrm{d}x - \int_D^A \frac{\partial\phi}{\partial y}\mathrm{d}y\right]. \tag{2.30}$$

To calculate Γ it might be better to use the current instead of the phase, that is

$$\mathbf{j} = n\mathbf{v} = \frac{\hbar}{2m\mathrm{i}}\left(\psi^*\nabla\psi - \psi\nabla\psi^*\right) = \frac{\hbar}{m}\mathrm{Im}\left[\psi^*\nabla\psi\right]. \tag{2.31}$$

Using this definition we obtain

$$\Gamma = \int_A^B \frac{j_x}{n}\mathrm{d}x + \int_B^C \frac{j_x}{n}\mathrm{d}y - \int_C^D \frac{j_x}{n}\mathrm{d}x - \int_D^A \frac{j_y}{n}\mathrm{d}y. \tag{2.32}$$

In this way we avoid the problem of calculating ϕ through trigonometric functions and worrying about the sign of the angles. This is the method used in the numerical code.

2.3.1 Miscible regime

The main result we find is that, in the miscible regime and without coherent coupling between the two components, the stability of persistent currents is closely related to the Bogoliubov spectrum.

Dispersion relations above states with finite velocities

Since we are interested in the stability of states with superfluid currents we need to calculate the Bogoliubov spectrum above a mean-field state where components a and b move at velocities $\mathbf{v}_a$ and $\mathbf{v}_b$, respectively,

$$\Psi_\sigma(\mathbf{r},t) = \left(\psi_\sigma + \delta\Psi_\sigma(\mathbf{r},t)\right) e^{-i\mu_\sigma t/\hbar} e^{-im\mathbf{v}_\sigma\cdot\mathbf{r}/\hbar} \tag{2.33}$$

where $\mu_a = mv_a^2/2 + g_a n_a + g_{ab} n_b$ is the chemical potential for component a and μ_b is the corresponding expression for component b (see Eqs. (2.17)-(2.18) plus the kinetic energy associated with the rotation). The superfluid velocities $\mathbf{v}_\sigma$ are related to the phase of the order parameters, S_σ, as $\mathbf{v}_\sigma = \hbar/m\nabla S_\sigma$, where $\sigma = a,b$. To find the equations for the (small) perturbations $\delta\Psi_\sigma$, we proceed as in Sec. 2.2 obtaining a linear operator $\mathscr{L}$ with a shift given by the velocities

$$\mathscr{L} = \begin{pmatrix} h_a - \hbar\mathbf{v}_a\cdot\mathbf{k} & g_a n_a & g_{ab}\sqrt{n_a n_b} & g_{ab}\sqrt{n_a n_b} \\ -g_a n_a & -h_a - \hbar\mathbf{v}_a\cdot\mathbf{k} & -g_{ab}\sqrt{n_a n_b} & -g_{ab}\sqrt{n_a n_b} \\ g_{ab}\sqrt{n_a n_b} & g_{ab}\sqrt{n_a n_b} & h_b - \hbar\mathbf{v}_b\cdot\mathbf{k} & g_b n_b \\ -g_{ab}\sqrt{n_a n_b} & -g_{ab}\sqrt{n_a n_b} & -g_b n_b & -h_b - \hbar\mathbf{v}_b\cdot\mathbf{k} \end{pmatrix} \tag{2.34}$$

where now h_σ are defined as $h_\sigma = \hbar^2 k^2/(2m) + g_\sigma n_\sigma$, with $\sigma = a,b$.

We first analyse the situation in which the mixture is at rest, $\mathbf{v}_\sigma = 0$. In this case the diagonalization of the eigenproblem gives again the dispersion relations of last Section that, generalised to $n_a \neq n_b$ and rewritten in terms of the total density $n \equiv n_a + n_b$ and of the polarization of the mixture $P = (n_a - n_b)/n$, read

$$\hbar\omega_{d,s} = \sqrt{\frac{\hbar^2 k^2}{2m}\left(\frac{\hbar^2 k^2}{2m} + 2m{c_{d,s}}^2\right)} \tag{2.35}$$

with

$${c_{d,s}}^2 = \frac{gn}{2m}\left(1 \pm \sqrt{P^2 + (1-P^2)\frac{{g_{ab}}^2}{g^2}}\right). \tag{2.36}$$

As one can see from Fig. 2.5, in the limit of $P \to 1$ the density mode is dominated by the majority component, $c_a \to c_d$, while the spin mode is dominated by the minority

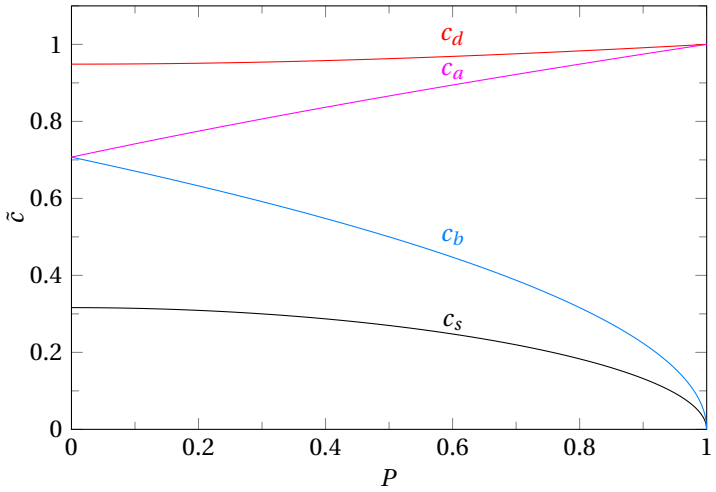

FIGURE 2.5: Spin, density and single species speeds of sound for $g_{ab} = 0.8g$ with $\tilde{c} = c\sqrt{gn/m}$.

component, $c_b \to c_s$. Notice also from Eq. (2.36) that at the demixing transition point, i.e. $g_{ab} = g$, the spin speed of sound vanishes for any polarization P, or equivalently the susceptibility of the mixture diverges. Stability of persistent currents in this critical regime has been addressed in Refs. [1, 3] for a one-dimensional ring, and in Ref. [52] in two dimensions.

The second situation we study is when $\mathbf{v}_a = \mathbf{v}_b = \mathbf{v}$. It is easy to see that this gives rise to a shift in the frequencies by the quantity $\mathbf{v}\cdot\mathbf{k}$, which has the role of a classical Doppler shift

$$\hbar\omega_{d,s} = \sqrt{\frac{\hbar^2 k^2}{2m}\left(\frac{\hbar^2 k^2}{2m} + 2mc_{d,s}{}^2\right)} - \hbar\mathbf{v}\cdot\mathbf{k}. \tag{2.37}$$

As one can see in Fig. 2.6, when the system is in the proximity of the criticality, $g_{ab} \lesssim g$, the effect of a non zero velocity is small for the density mode that is higher in energy. In contrast, the spin mode is much more sensitive and adding a velocity can have strong consequences on the dispersions. In particular, they are bended toward the k-axis and, for large enough velocities they can become negative leading to an energetic instability which, as shown in the next Section, is responsible for a great extent to the decay of persistent currents. Notice also that in Fig. 2.6 we indicate the velocity values by means of the parameter κ that takes into account the quantization of the circulation in a ring geometry, $|\mathbf{v}| = \hbar\kappa/mR_0$ where R_0 is the central radius of the ring.

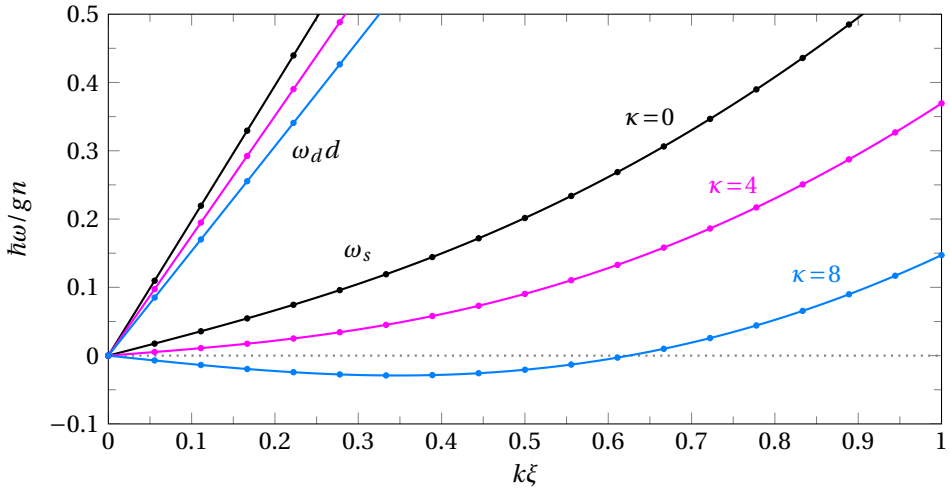

FIGURE 2.6: Bogoliubov excitation spectra for density (ω_d) and spin (ω_s) modes. Different colors correspond to different quanta of circulation in the ring, points correspond to discretized values of k arising from the ring geometry. Parameters used are $P = 0$, $g_{ab} = 0.95g$, radius of the ring $R_0 = 18\xi$.

Stability diagram

For $\kappa = 0$ the Bogoliubov dispersion relations are linear at low k with slope given by the spin or density speed of sound so, for $\kappa \neq 0$, when the flow velocity equals the speed of sound, the dispersion becomes tangent to the $\omega = 0$ axis and triggers a Landau instability. Since the spin mode has the lower speed, the instability appears first in the spin channel leading to the following criterion for the stability of persistent currents: *when the flow velocity is larger than the spin speed of sound the currents become energetically unstable.*

In order to check our prediction we have numerically solved the coupled GP equations (see Chapter 4) with a vortex-like initial configuration

$$\Psi_\sigma(\tau = 0) = \psi_\sigma \left(\frac{x + i\,y}{\sqrt{x^2 + y^2}} \right)^{\kappa_\sigma} \tag{2.38}$$

with $\sigma = a, b$, τ the imaginary time variable, $\kappa_a = \kappa_b = \kappa$. The functions ψ_σ have been built from both random density and phase distributions, in order to prevent the algorithm from reaching false metastable states. The system is then allowed to evolve freely in imaginary time until convergence is reached. After convergence, we calculate the expectation value of the angular momentum per particle, $L_z^{(\sigma)}$, and the circulation integral, Γ_σ, evaluated in a closed circuit around the central hole.

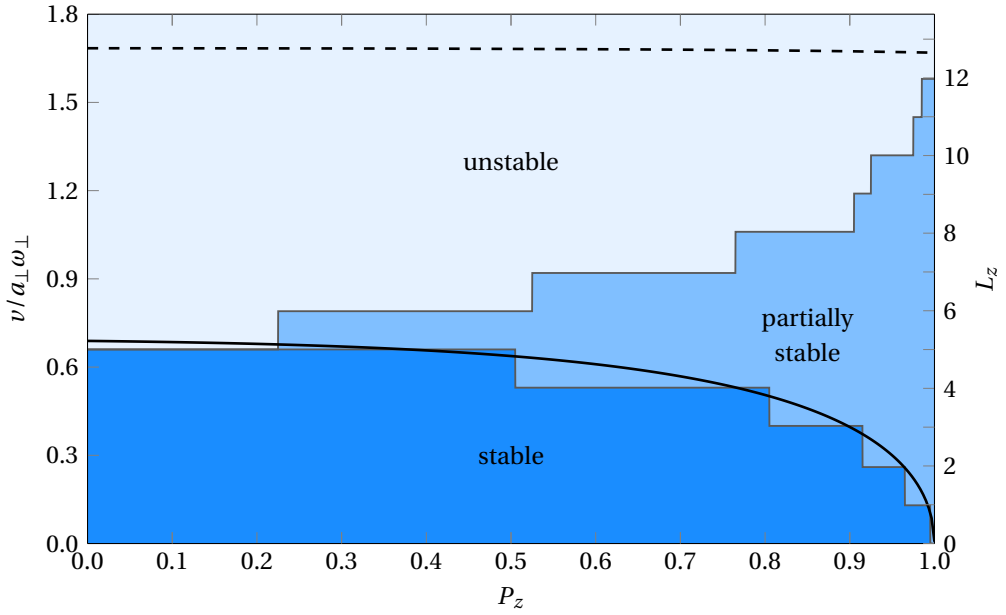

FIGURE 2.7: Stability diagram of persistent currents in the miscible regime obtained from imaginary-time simulations. The left y-axis shows the initial velocity and the right y-axis the initial angular momentum per particle, which is quantized in multiples of κ. The solid line represents the spin speed of sound c_s [see Eq. (2.36)] computed at the density maxima by taking into account the corrective factor for 2D geometries (see Appendix A). The upper dashed line represents the boundary for dynamical instability when $v_b = 0$ obtained from Bogoliubov analysis. $a_\perp$ is the harmonic oscillator length $a_\perp = \sqrt{\hbar/m\omega_\perp}$.

The result are summarized in Fig. 2.7. The metastability of the initial states is shown as different shaded regions, corresponding to different stability regimes. The supercurrent is stable (dark region) if the velocity at the density maximum is smaller than the spin speed of sound (black solid line), in good agreement with the above criterion relating supercurrent instability to the Landau instability of the spin mode (see also [3]). The spin speed of sound has been renormalized by the factor $\sqrt{2/3}$ that takes into account the effect of the transverse width of the condensate (see Appendix A). This factor has been obtained in Thomas-Fermi limit and for a very long prolate harmonic trap with periodic boundary conditions. There might thus exist a small correction due to the anharmonicity of the trapping potential used in the numerical simulations (see Eq. 2.24) and to the bending introduced by the ring geometry. As one can see in Figure 2.7, these corrections do not seem to have any appreciable effect on the numerical data.

Furthermore, the numerical simulations allow us to distinguish between two unstable regions:

(i) a *partially stable* one, where the current in the majority component is stable, while it decays in the minority component;

(ii) an *unstable* one where both currents are unstable.

While the boundary between the partially stable and the stable region is determined by the spin speed of sound, the boundary between the partially stable and the unstable region is not fixed by any universal criterion and its exact position depends on the geometry of the system, as is discussed in the next paragraph.

Partially stable region

The existence of a criterion for the stability of currents is quite obvious but the presence of a region in which only the current in the minority component decays can be surprising. In this paragraph we give a physical interpretation of the mechanism that lead to this behaviour.

If we go back to Fig. 2.5 we see that in the limit of $P \to 1$ the spin mode is dominated by the minority component. In physical terms, the minority component is more sensitive to spin excitations, whereas the majority component becomes more stable, being less affected by spin-density excitations. In mathematical terms, further insight is provided by considering the case where the two components have different velocities, $v_a \neq v_b$. Clearly, once the minority component has lost a part of its initial angular momentum, the dispersion relation is no longer given by Eq. (2.36) and a non-linear Doppler shift is originated by the velocity difference. As a result, the system becomes more stable.

An example of this analysis is shown in Fig. 2.8. This figure shows the maximum velocity that component a can sustain for a fixed (quantized) initial velocity of b, such that the energy of the spin excitations remains positive. The different curves have been obtained by diagonalizing the operator $\mathscr{L}$, see Eq. (2.34), with the parameters and the densities taken from the ground state of the GP equations in the absence of currents. The factor $\sqrt{2/3}$ (see Section A.2) has been applied to all curves. For comparison, we have also plotted the spin sound velocity for equal flow velocities, c_s, and the line of dynamical instability for $v_b = 0$ (see next Section). We see from the figure that, at fixed P, as the velocity difference grows (that is, κ_b decreases), the allowed maximum velocity for component a is larger. This means that the superflow can be stabilized by losing velocity in one of the components (in this case the minority component b). This argument justifies the presence of the partially stable region in Fig. 2.7.

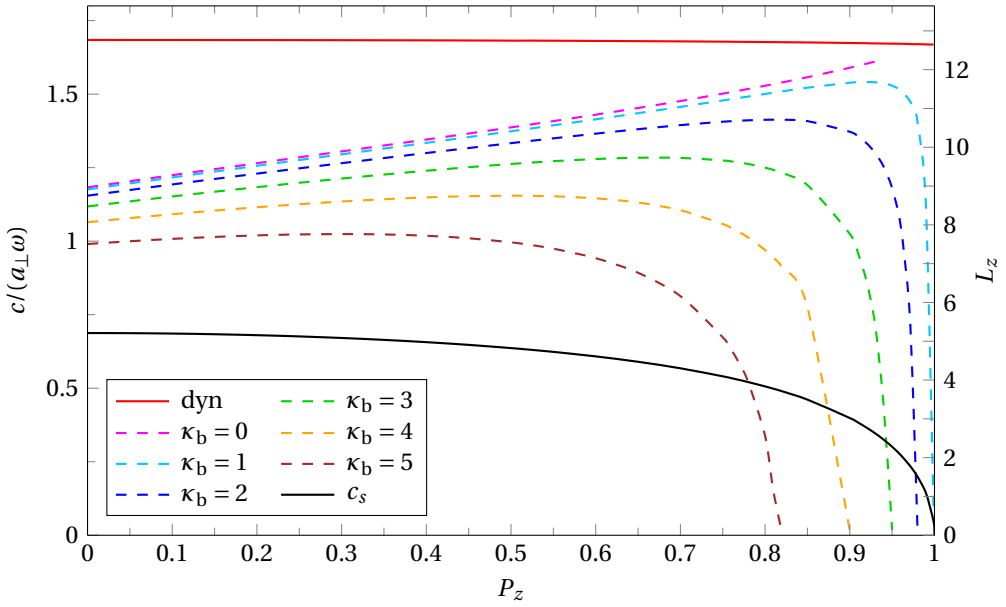

FIGURE 2.8: Lines of energetic instability for $v_b = \hbar\kappa_b/mR_0$ for different values of κ_b (dashed lines). The left y-axis shows the initial velocity and the right y-axis the initial angular momentum per particle, which is quantized in multiples of κ. The instability corresponds to the maximum velocity for the a component that leads to a positive spin-mode frequency. Dynamical instability for $v_b = 0$ (red full line) and spin speed of sound for equal velocities (black full line).

In order to further check these results and to avoid any spurious effect due to imaginary time evolution, we also ran some simulation in real time adding a dissipation term (see Chapter 4) in the GP equations. In Fig. 2.9 are represented the obtained results. As one can see from the upper panel, the current in the majority component remains stable throughout all the dynamics while the current in the minority one decays. The decay is indeed induced by the creation of vortices that enter through the internal ring surface, travel across the ring and exit from the external ring surface as is shown in the density snapshots of Fig. 2.9 for the majority (upper row) and minority components (lower row). These snapshots show the dynamical process explained above very clearly:

(a)-(b) the spin instability kicks in as out-of-phase density oscillations in the azimuthal direction

(c)-(d) since the minority component is more sensitive to this perturbation, its density oscillations grow enough to allow the penetration of vortices inside the ring

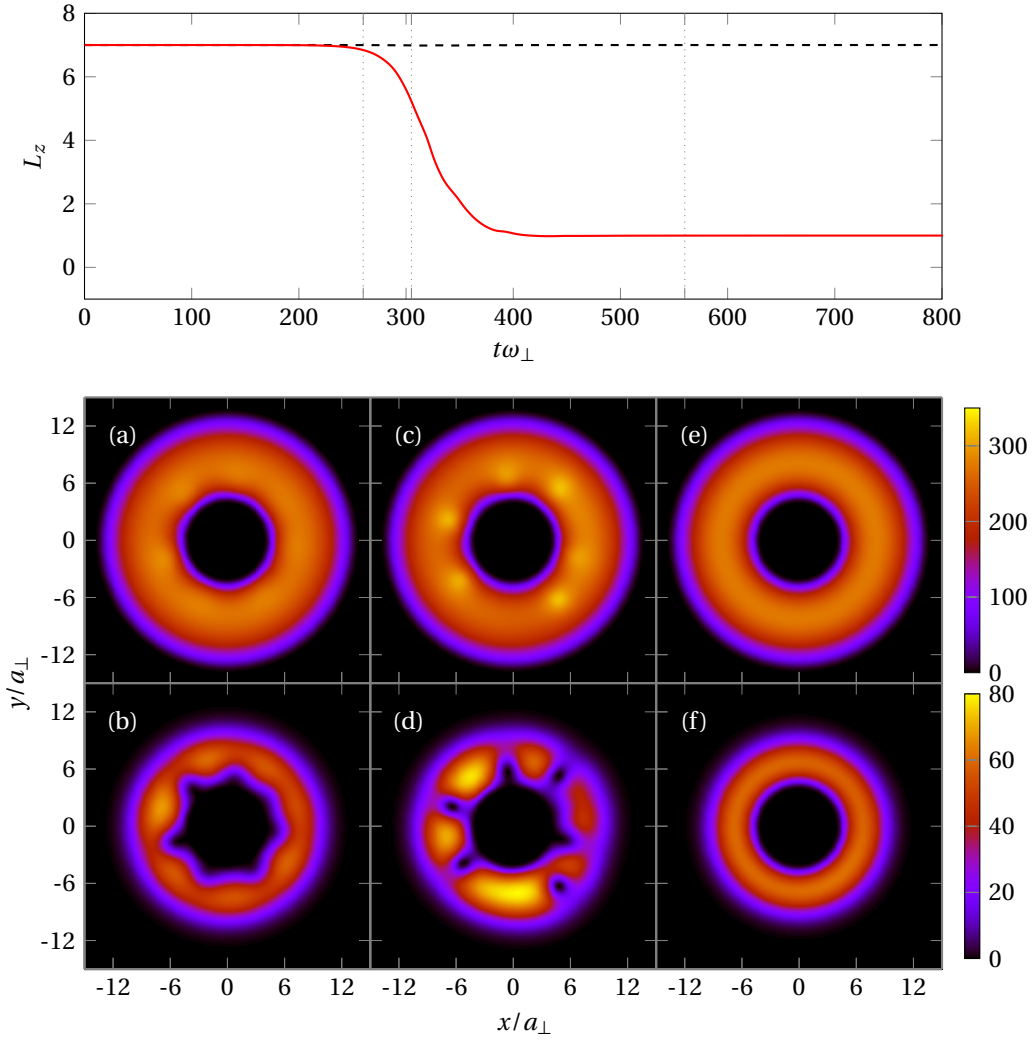

FIGURE 2.9: Upper panel: time-dependence of angular momentum of components a (dashed line) and b (solid line) in real-time dynamics in the partially stable region. Dotted lines represent time at which snapshots are taken. Lower panels: density snapshots of components a (upper row) and b (lower row) at times: $t = 260\omega_\perp^{-1}$ in panels (a) and (b), $t = 305\omega_\perp^{-1}$ in panels (c) and (d), and $t = 560\omega_\perp^{-1}$ in panels (e) and (f). The density (in units of $a_\perp^{-2}$) is represented by the color scale. For this case $P_z = 0.8$ and $\kappa = 7$.

(e)-(f) finally, after losing angular momentum, the system is stabilized through the new stability criterion shown in Fig. 2.8

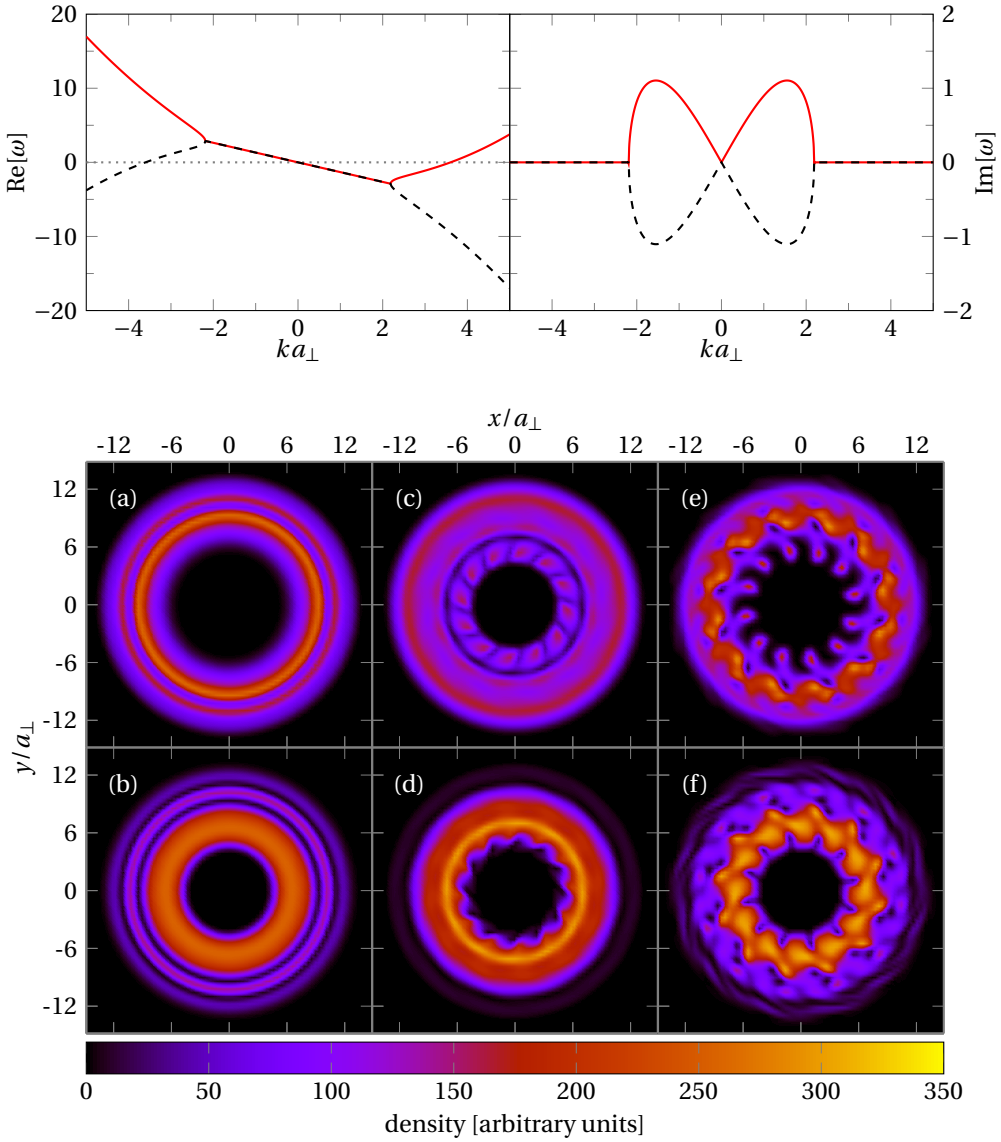

FIGURE 2.10: Dynamical instability for $\kappa_a = 20$, $\kappa_b = 0$. Top row: real and imaginary parts of the dispersion relation for the spin mode. Positive- (negative-) norm solutions are represented in solid (dashed). Bottom rows: Snapshots of majority [(a),(c),(e)] and minority [(b),(d),(f)] component densities (in units of $a_\perp^{-2}$) during imaginary-time dynamics.

Dynamical instability

The energetic instability, although being the relevant one when the two superfluids have the same velocity, is not the only mechanism that can trigger the decay of persistent cur-

rents in a binary mixture. Indeed, when the difference between the velocities of the two components, $|v_a - v_b|$, exceeds some critical value the eigenfrequencies corresponding to the spin-density mode acquire an imaginary part, leading to an exponential growth of the spin excitations that makes the flow dynamically unstable.

This dynamical instability is a more general result due to the breaking of Galilean invariance and in the context of binary mixtures is know as counterflow instability. It has been studied both theoretically [56, 57, 58, 59] and experimentally [60, 61] and recently also in the context of spin-orbit coupled condensates [62].

In the top panel of Fig. 2.10 the structure of the dispersion relations is shown. In a range around 0 the frequencies acquire an imaginary part and the real part, in the limit of small k, is nonzero in contrast to the case of the demixing instability driven by interspecies interaction.

Also in this case we can distinguish three different regimes in the (this time imaginary) time dynamics (see density snapshots of Fig. 2.10):

(a)-(b) in a first stage the two components oscillates in a radial breathing mode;

(c)-(d) in a second stage the dynamical instability shows up and deformations in the condensate densities appear;

(e)-(f) in a third stage vortices enter in the mixture stabilizing the angular momentum to $L_z^{(a)} = L_z^{(b)} = L_z/2$.

Notice that the maxima of density in one component correspond to the minima of the other component thus confirming that the instability is driven by the spin mode. Since our imaginary time evolution has no dissipation terms, the total angular momentum is conserved and the vortices can not escape the torus. However if we add a small imaginary term on the left-hand of GP equations we get an evolution in which both energy and angular momentum decrease in time thus allowing the vortices to exit.

2.3.2 Immiscible regime

In the last Section we learned that the criterion for the stability of currents in miscible mixture is related to the Bogoliubov spectrum and in particular to the spin speed of sound. When the mixture is in the immiscible regime things are very different. The ground state is formed by two single-species condensates separated by a domain wall and, excluding the modes located in the vicinity of the wall, the Bogoliubov spectrum in

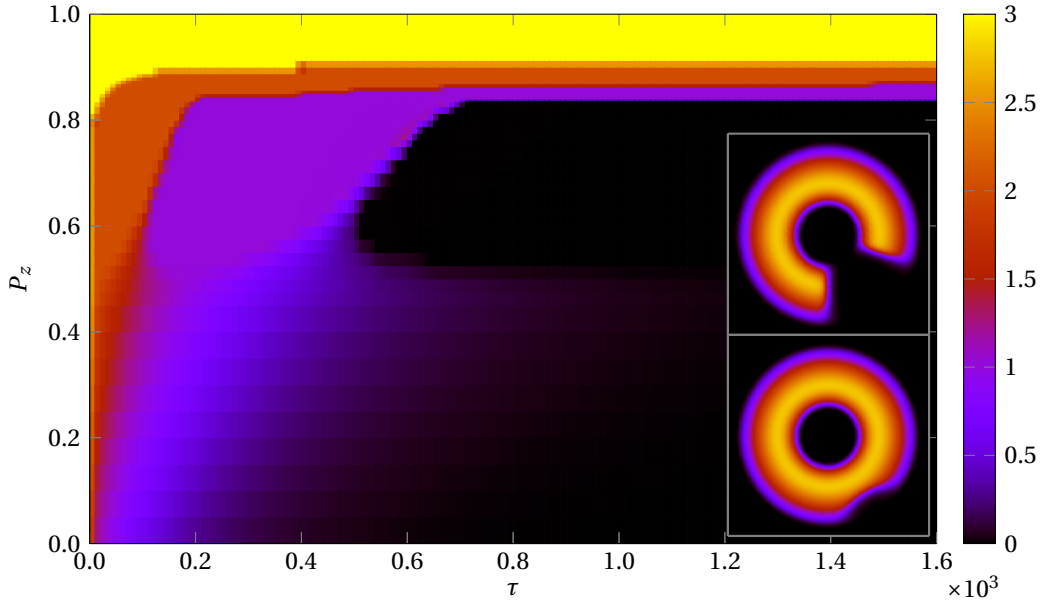

FIGURE 2.11: Stability diagram in the phase separated regime for the majority component, for different values of the polarization and as a function of the imaginary time, τ. The color scale represents the value of the circulation. In the insets the final density of the majority component for $P = 0.6$ (top) and $P = 0.95$ (bottom) are plotted.

the bulk is that of a single component. In this case we can not rely on simple analytical arguments and the results strongly depend on the geometry of the system. For these reasons we show only some numerical results.

In Fig. 2.11 the stability diagram for the majority component is plotted. As one can see the current is stable only for very high polarization, $P > 0.9$. In order to explain such a behaviour we take a look at the density profiles for different polarization (see insets of Fig. 2.11, the minority component is not shown but it occupies the empty region of the ring). When P is small, the two components occupy two sectors of the ring whose length is determined by the value of P (top inset). Conversely, when P is large, the minority component occupies only a small region, creating a barrier (or weak link, depending on the value of the penetration length) for the majority component (bottom inset). These two kinds of density distributions correspond, respectively, to ground states characterized by $\mu_a = \mu_b$ and by $\mu_a > \mu_b$.

The current in the minority component is always unstable, since it occupies a simply connected region in the torus. The persistence of the current in the majority component depends instead on satisfying two conditions: (i) it occupies a multiply connected re-

gion, and (ii) the barrier formed by the minority component is small enough to prevent vortices from escaping (similarly to what happens in weak-link systems [**Wright2013**, 50, 63] and in dipolar condensates [64]). In the present situation, we identify three regimes: for $P_z > 0.9$ persistent currents are stable, for $0.6 < P_z < 0.9$ the decay consists in a series of jumps through states with integer circulation, and for $P_z < 0.6$ the decay is continuous. Despite not being real time, imaginary time evolution gives an idea of whether the system reaches its ground state, or else remains blocked in a metastable state. Qualitatively similar behaviour is expected in an experiment due to dissipative effects.

2.3.3 Coherently coupled mixture

For the sake of completeness, we briefly discuss the case in which particle exchange is allowed by the presence of a linear coupling, $\Omega \neq 0$. Since in this case a gap opens in the spin-density mode, the Landau critical velocity becomes larger than in the binary mixture. Consequently, the spinor two-component condensate becomes stable in configurations where the normal mixture was unstable. Stability is also reinforced by the presence of Ω, which ensures $P = 0$. This result fully agrees with the experimental observations of [4]. In the polarized regime, the criterion for stability is more complex since the neutral and polarized phases always coexist in the trap [39]. However, phase coherence still guarantees that the two species decay together. For a more detailed and recent analysis of persistent currents in coherently coupled Bose-Einstein condensates please see Ref. [65].

CHAPTER

3 Trapped case

In this Chapter we extend the results of the previous one to a system trapped with harmonic shaped potentials. In particular we show the different ground states the mixture can have with or without Rabi coupling and we analyse its dynamics in some interesting regimes: we study the behaviour of a solitonic structure and the dipole oscillations of the mixture across the Ω-induced phase transition. In this last case we characterize an interesting phenomenon of ground state relaxation.

Contents

The experimental realization of Bose Einstein condensates has been achieved in atomic gases where the shape of the trapping potential is, in many cases, well approximated by a harmonic shape.

In the presence of harmonic trapping the GP equation should be solved numerically except for some special limits, one of this is the so called Thomas-Fermi limit. When the interaction is repulsive ($g > 0$) its effect is to spread the gas, increasing the size of the cloud with respect to the non-interacting case. Eventually, if the effect of the interaction is very important, the width of the gas will become so large and the density profile so smooth that one can ignore the kinetic energy term in the GP equation.

When density is a smooth function of the spatial coordinate one can also use the Local Density Approximation describing every point of the cloud as an homogeneous system with density equal to the local density of the inhomogeneous one.

3.1 Phase separated configuration

For what regards the transition between a miscible and an immiscible phase the results of Section 2.1.1 hold equally within LDA. The criterion for phase separation is the same ($g_{ab} > \sqrt{g_a g_b}$) and the only difference is that changing the trap shape or the system parameters we can have a wider zoology of configurations (see for instance [32] for more details).

We now focus on the particular case of a highly unbalanced mixture and for concreteness we consider $N_a \gg N_b$ [1]. For a mixture with equal masses, equal traps, equal intraspecies interactions, $g_a = g_b \equiv g$, and in the phase separation regime ($g_{ab} > g$), the ground state densities are plotted in the left panel of Figure 3.1. Let us remind that in obtaining the phase separated density profiles with numerical methods one has to be a little careful. The ground states in Figure 3.1 have been obtained inserting some asymmetry in the initial wave functions, if they have been perfectly symmetric one would have found the wrong ground state in which the smaller component remains at the centre of the bigger one or it splits up in two parts located on the sides (both these solutions have a bigger energy). A recent and detailed discussion about this issue can be found in [66].

In order to get a configuration where the minority component is at the centre of the trap (as shown in the right panel of Figure 3.1) we take, for equal masses, the trapping frequency of the minority component bigger than the one of the majority component. Indeed, in this case, the energy gained by separation is less than the energy lost by going

[1] In such a regime LDA does not generally hold.

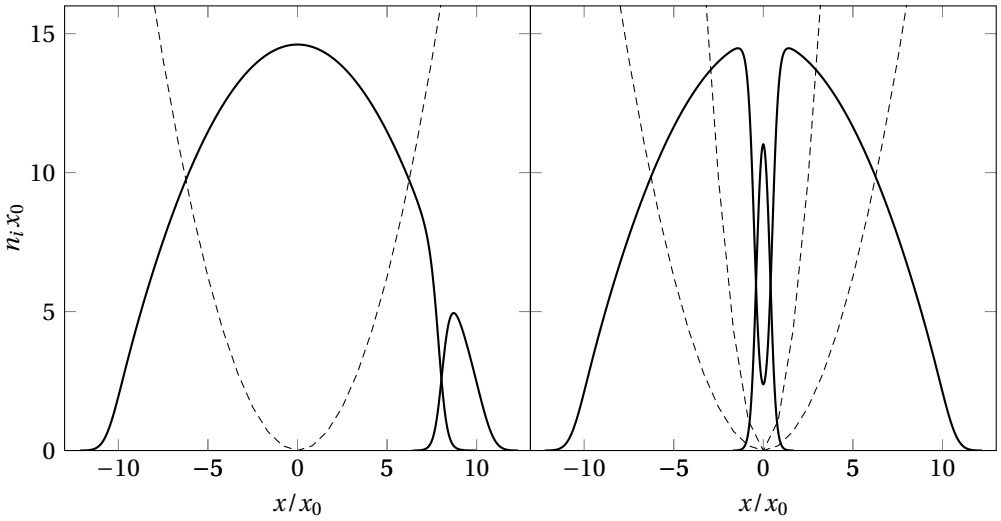

FIGURE 3.1: Ground state configurations in the phase separated regime. Left panel: a typical configuration for equal trapping frequencies. Right panel: the same system with $\omega_b = 2.5\omega_a$. Parameters are $N_a = 200$, $N_b = 10$, $g_{ab} = 1.5g$.

in a region in which the trapping potential is higher. When we have very few particles in the minority component (in Fig. 3.1 $N_a = 200$ and $N_b = 10$) the quantum pressure plays an important role and makes the majority component connected.

It is interesting to notice that in this last configuration the density profiles do not show any drastic change by going across the phase transition point $g_{ab} = \sqrt{g_a g_b}$ (see Figure 3.2). As we will see in Section 3.2, the dynamics of such structure is instead very much affected by the interaction values showing two completely different behaviours in miscible and immiscible regimes.

Let us here just mention that, if we remove the minority trapping potential for $g_{ab} < g$, the minority component will escape while, for $g_{ab} > g$, it will remain there.

3.2 Breathing and dipole modes across phase separation

In this section we will focus on the dynamics of an unbalanced mixture going across the phase separation point. In particular we will study two different modes of the minority components of the system: breathing and dipole mode.

In the former the system is initially in the ground state obtained with both traps centred in zero but with a bigger trapping frequency for the minority component (see right plot of Figure 3.1). At time $t = 0$ this frequency is suddenly set to the value of the majority

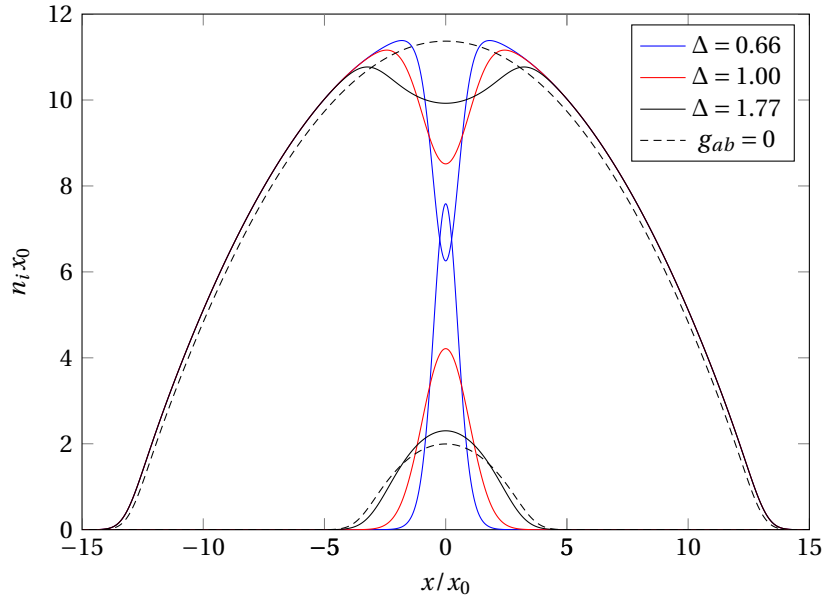

FIGURE 3.2: Majority and minority density profiles for different values of the parameter $\Delta = g_a g_b / g_{ab}^2$. We change the value of g_b and we take $g_{ab} = g$. The mixture is miscible for $\Delta > 1$ and the case $g_{ab} = 0$ corresponds to $\Delta = \infty$.

component trap and the system starts its oscillations. At regular real time intervals we calculate and record the expectation value of our breathing operator B,

$$B = \frac{1}{N_b} \int x^2 |\Psi_b(x)|^2 \mathrm{d}x. \tag{3.1}$$

For the dipole mode the system is again prepared with a narrower trap for the minority component but this time this second trap is shifted and centred in a position x_D. At time $t = 0$ the trap of the minority component is suddenly centred in zero and its frequency set to the value of the majority component one so the system starts to oscillate in a species independent external potential. At regular real time intervals we calculate and record the expectation value of our dipole operator D,

$$D = \frac{1}{N_b} \int x |\Psi_b(x)|^2 \mathrm{d}x. \tag{3.2}$$

3.2.1 Double Domain Wall Soliton

As explained in Ref. [21] and Ref. [67], for a very unbalanced mixture it is possible to describe the dispersion law of the minority component simply as a correction to the one

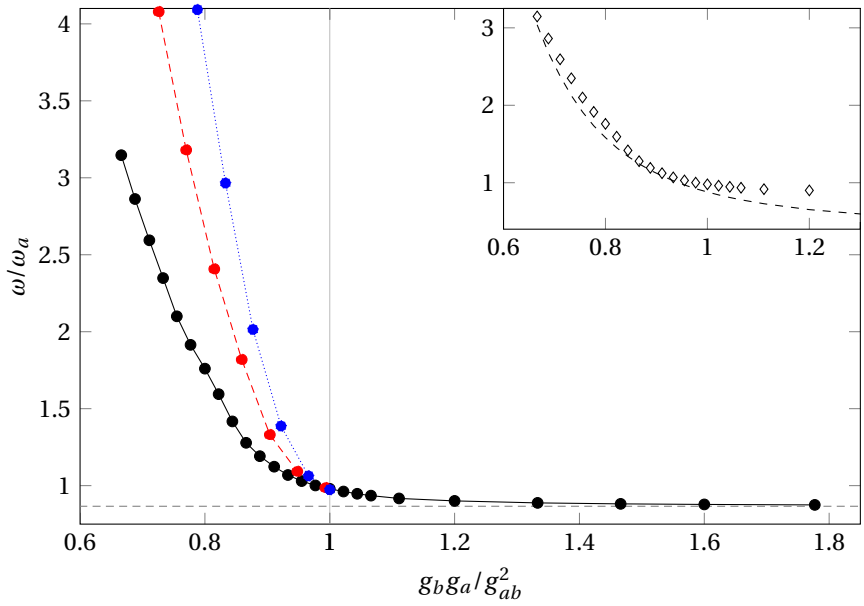

FIGURE 3.3: Breathing mode frequencies across phase separation point as a function of g_b. Dashed grey line represents the value of frequency in miscible regime given by Eq. (3.3). Parameters are $N_a/N_b = 20$, $m_a = m_b$, $g_a = 2g_{ab} \equiv g$ for the black points, $g_a = 2g_{ab} = 1.5g$ for the red ones and $g_a = 2g_{ab} = 2g$ for the blue ones. Lines connecting points are only a guide to the eyes. Inset: breathing mode frequency for $g_a = 2g_{ab} \equiv g$ (diamonds) and function $1/(kd)$ (dashed line).

of a single component gas. In particular, being b the minority one, one has

$$\omega_{k,b}{}^2 = \omega_b{}^2 \, \frac{k(k+1)}{2} \left(1 - \frac{g_{ab} m_a \omega_a{}^2}{g_a m_b \omega_b{}^2}\right) \tag{3.3}$$

where the first fraction is the usual dispersion for a one dimensional single component gas [68] while the term in parenthesis is the correction. The modes that we consider here corresponds to $k = 1$ (dipole mode) and $k = 2$ (breathing, lowest compressional mode).

Notice that in this regime the minority component modes coincide essentially with the out-of-phase mode and it is interesting that the parameter g_b does not enter at all in Equation (3.3). This means that the out-of-phase frequency can go to zero, but such softening has nothing to do with the the phase separation. In the homogeneous case, instead, as shown in Chapter 2, the lowest out-of-phase mode is linear (sound like) in the momentum and it becomes quadratic, i.e. the speed of sound becomes zero or equivalently the susceptibility diverges, precisely at the phase transition.

This result is obtained considering a miscible system, we will now figure out how things change going through the phase transition. A clever way for doing so is modify

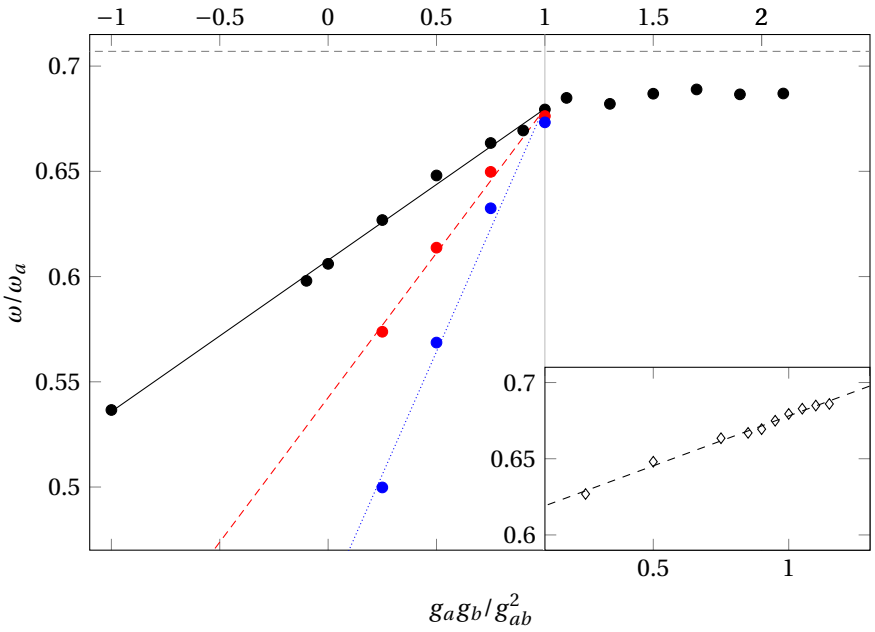

FIGURE 3.4: Dipole mode frequencies across phase separation point as a function of g_b. Dashed grey line represents the value of frequency in miscible regime given by Eq. (3.3). Parameters are $N_a/N_b = 20$, $m_a = m_b$, $g_a = 2g_{ab} \equiv g$ for the black points, $g_a = 2g_{ab} = 1.5g$ for the red ones and $g_a = 2g_{ab} = 2g$ for the blue ones. Lines are linear fits to the data points. Inset: dipole mode frequency for $g_a = 2g_{ab} \equiv g$ (diamonds) and fitted function $A + Bkd$ (dashed line).

only g_b: if Eq. (3.3) correctly describes the dispersion then, since it does not depend on g_b, we should get a constant frequency no matter the value of the minority component intraspecies interaction. The results of such analysis are shown in Figure 3.3 for the breathing mode and in Figure 3.4 for the dipole mode.

From both these Figures one immediately sees the differences between the miscible and immiscible regime. In the first one the frequencies are almost constant varying g_b while in the second one the behaviour is very different and not universal. The general trend is however quite natural. For the breathing mode the narrower the density hole (see Figure 3.2), the larger is the frequency. Indeed the frequency increases both decreasing g_b or increasing g_a. For the dipole mode instead, the narrower the density hole the smaller is the frequency and it decreases both decreasing g_b or increasing g_a.

We know that in the immiscible regime the mixture has a tendency in forming domain walls. Indeed if one tries to fit the soliton solutions with a simple double domain

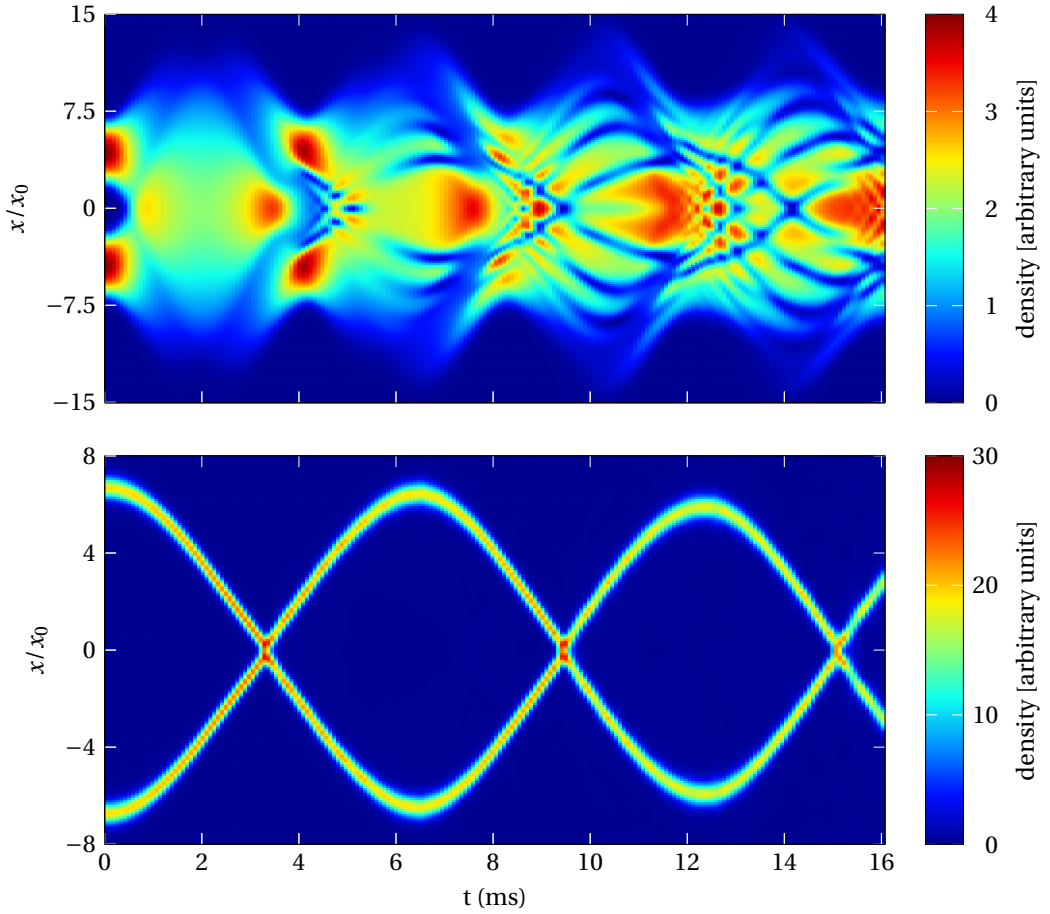

FIGURE 3.5: Density maps describing the time evolution of a collisional event in miscible regime (top plot) and immiscible regime (bottom plot).

wall ansatz in analogy with the single DW profile (see, e.g., [69])

$$\psi_{\mathrm{DDW}}(x) \propto \tanh[k(x+d)] - \tanh[k(x-d)], \tag{3.4}$$

with k and d positive real numbers, the agreement is perfect. Moreover as it can been seen from the insets of Figures 3.3 and 3.4 the mode frequencies are strictly related to the dimensionless parameter kd, which can be interpreted as an effective width of the double domain wall soliton. In particular we find that in the solitonic regime $kd \propto \Delta$ and the breathing mode frequency is inversely proportional to g_b or equivalently to kd at fixed g_a and g_{ab}, while the dependence of the dipole mode frequency is linear (Figs. 3.3 and 3.4). Such a nice behaviour does not work in the miscible regime where domain walls should not be present.

In this Section we often refer to the double domain wall as a soliton, now we want to explain the motivations behind this definition. The first evidence is its dynamics inside the trap during a dipole oscillation. The double domain wall structure remains localized, its motion is not dispersive and the structure is globally well defined also after many periods of oscillation. Vice versa in the miscible case the motion of the impurity is dispersive and it excites phonons in the majority component already after a few periods of oscillation. The oscillation of the minority component (the out-of-phase mode) is damped out already after a few periods [67].

Finally we address the behaviour of the double domain wall against collisions with respect to the the miscible case. For this we simulate a collision between two very small cloud of the minority component. We find that the collisional behaviour is even more different depending on whether the gases are miscible or not as clearly shown in Figure 3.5. In the earlier case, $\Delta > 1$, already after the first collision, dispersion and interference appear and the two impurities lose soon their identity. On the contrary the double domain wall solitons ($\Delta < 1$) keep being well defined objects even after many collisions, justifying the name soliton for such a structure.

3.3 Paramagnetic and ferromagnetic states in trap

As already described in Chapter 2, when the coherent coupling is switched on, things change very much. Phase separation does not occur any more and the mixture shows instead a phase transition between an unpolarized and a polarized configuration. The critical point is no more the geometric mean of the intraspecies interactions but it becomes density dependent with the addition of a term proportional to Ω, $\bar{g}_{ab} = g + 2|\Omega|/n$.

As already discussed, neglecting the kinetic terms in GP equations and subtracting and adding them we obtain

$$\left(g - g_{ab} + \frac{|\Omega|}{\sqrt{n_a n_b}}\right)(n_a - n_b) = V_b - V_a \tag{3.5}$$

$$\left(g + g_{ab} - \frac{|\Omega|}{\sqrt{n_a n_b}}\right)(n_a + n_b) = 2\mu - (V_b + V_a) \tag{3.6}$$

where this time we have also a term taking into account the external trapping potentials. Here we consider two equal harmonic traps of the form

$$V_a(r) = V_b(r) \equiv V(r) = \frac{1}{2} m\omega^2 r^2, \tag{3.7}$$

so the right-hand-side of Eq. (3.5) vanishes and we obtain the same equation of the homogeneous case with the only difference that now the densities are position dependent. This means that, within local density approximation, the system has two different ground states characterized locally by the same solutions of the homogeneous case, Equations (2.7) and (2.8). In particular the system is in the unpolarized ground state (GSU) for $g_{ab} < \bar{g}_{ab}(r)$ and in the polarized one (GSP) for $g_{ab} > \bar{g}_{ab}(r)$.

The differences with the homogeneous case are given by the fact that now also the critical condition is position dependent. Since at low density the Rabi flipping term always dominates, for the two-component spinor condensate in a harmonic trap we can distinguish two different scenarios:

(i) the whole system is in GSU, i.e. the critical condition $g_{ab} < \bar{g}_{ab}(r)$ is fulfilled at the point in which it is more restrictive, that is at $r = 0$ where the total density is maximum;

(ii) GSP is the lowest energy state at the center of the trap, i.e. $g_{ab} > \bar{g}_{ab}(0)$. Then, since the total density goes to 0 moving towards trap edges, there exists always a critical radius R_c above which the lowest energy state becomes GSU, i.e. $g_{ab} < \bar{g}_{ab}(r)$ for $r > R_c$. In this case we have coexistence of the two ground states in the same system with the transition occurring at $r = R_c$.

This allows us to define a critical value also for the Rabi coupling,

$$\Omega_{cr} = \frac{1}{2} n(0)(g_{ab} - g), \tag{3.8}$$

for values $\Omega \geq \Omega_{cr}$ the system is unpolarized everywhere.

When the system is in the GSU (everywhere in the first situation and for $r > R_c$ in the second one) the densities of the two components are equal, $n_a(r) = n_b(r) = n(r)/2$. Inserting these densities into Eq. (3.6), we can easily get an analytical expression for the profiles

$$n(r) = 2\frac{\mu + |\Omega| - V_{ho}(r)}{g + g_{ab}} = \frac{2(\mu + |\Omega|)}{g + g_{ab}} \left(1 - \frac{r^2}{{R_{TF}}^2}\right) \tag{3.9}$$

where

$${R_{TF}}^2 = \frac{2(\mu + |\Omega|)}{m\omega^2} \tag{3.10}$$

and μ is given by imposing the total number of particles

$$\mu = \left[\frac{3}{8} N(g + g_{ab})\right]^{2/3} \left(\frac{m\omega^2}{2}\right)^{1/3} - \Omega. \tag{3.11}$$

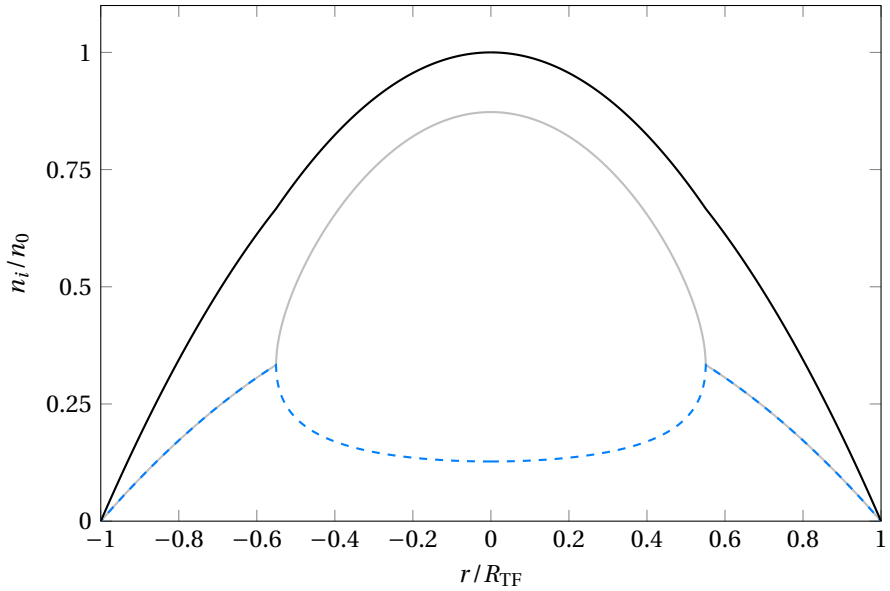

FIGURE 3.6: Ground state of the two component spinor condensate in equal harmonic traps: n_a (light grey), n_b (dashed blue) and n (black). The inner region is described by GSP and the outer one by GSU. Parameters are $g_{ab} = 1.3g$, $\Omega = 0.1\mu$ and $R_c \simeq 0.55R_{TF}$, n_0 represents the total density at the center of the trap.

At the critical radius both the terms in parenthesis on the left-hand-side of Eq. (3.5) must be zero. This means that we still have equal densities in the two components, so $\sqrt{n_a n_b} = n/2$, and setting to zero the first parenthesis we obtain the condition $n(R_c) = 2|\Omega|/(g_{ab} - g)$. Inserting it in Eq. (3.9) we finally find

$$R_c = \sqrt{\frac{1}{m\omega^2}\left(2\mu + 4|\Omega|\frac{g}{g - g_{ab}}\right)}. \tag{3.12}$$

In the internal region, where $r < R_c$ and the system is in GSP, the densities are different between each other and the only way to satisfy Eq. (3.5) is to have the first term equal zero. Solving this condition with the substitution $n_{a,b}(r) = n(r) - n_{b,a}(r)$ one gets

$$n_{a,b}(r) = \frac{n(r)}{2}\left[1 \pm \sqrt{1 - \left(\frac{2|\Omega|}{(g_{ab} - g)n(r)}\right)^2}\right] \tag{3.13}$$

Summarizing all these informations, we obtain the densities plotted in Figure 3.6. Due to the use of the local density approximation the density profiles measurement is a direct mapping of the phase diagram of the corresponding homogeneous system (see Fig. 2.1).

3.4 Narrowing one trap

In Section 3.2 we studied how the system behaves when the trap of one component has a bigger frequency than the trap for the second one. Now we want to analyse the same situation but with coherent coupling between components switched on.

We define the trapping potentials for the two species as

$$V_a = \frac{1}{2} m \omega_{\mathrm{ho}}^2 x^2, \qquad V_b = \frac{1}{2} m \left(\eta \omega_{\mathrm{ho}}\right)^2 x^2. \tag{3.14}$$

In Figure 3.7 we show different ground states for different values of η and in different positions along the paramagnetic-ferromagnetic transition. As one can see, a structure similar to the DDWS of Section 3.2 appears for large values of η and, in general, the effect of Ω above the transition is that of smearing the density profile of the minority component and of flatten the hole in majority one. In order to quantitatively characterize how the ground states are changed by the phase transition, we introduce a quantity named kurtosis and defined as the ratio between the fourth momentum and second momentum squared:

$$\gamma_2 = \beta_2 - 3 = \frac{m_4}{{m_2}^2} - 3. \tag{3.15}$$

In the definition the value 3 is subtracted because a Gaussian distribution has a kurtosis index $\beta_2 = 3$. The quantity γ_2 is a measure of the level of flattening of a distribution: values lower than 0 indicate that our curve is more flattened than a Gaussian, values greater than 0 the opposite, a curve sharper than a Gaussian. In our case it is better to take as reference the situation in which $\eta = 1$ (equal traps) and $\Omega \gg \Omega_{\mathrm{cr}}$ (equal ground state profiles for the two component). The corresponding value for the parameters used in numerical simulations is $\beta_2 \simeq 2.145$. Thus, our modified kurtosis is

$$\gamma_{\mathrm{GP}} = \frac{m_4}{{m_2}^2} - 2.145, \tag{3.16}$$

where

$$m_4 = \frac{1}{N_a} \int x^4 |\psi_a(x)|^2 \mathrm{d}x, \tag{3.17}$$

$$m_2 = \frac{1}{N_a} \int x^2 |\psi_a(x)|^2 \mathrm{d}x. \tag{3.18}$$

We will focus on the minority component since it is the one that, more or less, maintain its shape without drastically changing it on contrary of the majority one in which a central hole appears. In Figure 3.8 we show the result of such analysis for different values of

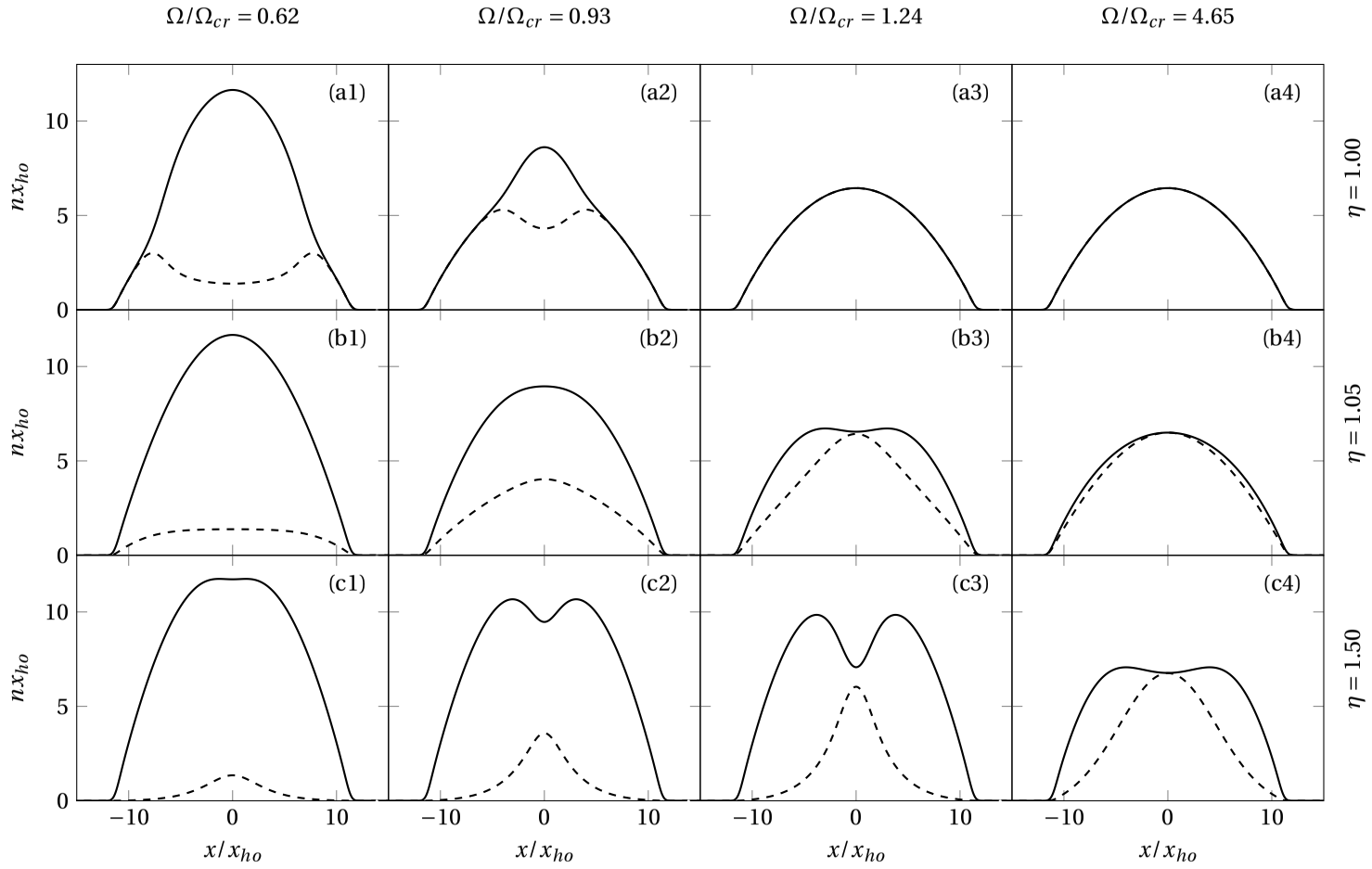

FIGURE 3.7: Ground states of a trapped coherently coupled Bose gas for different values of the narrowing factor η and of the Rabi coupling Ω. We use coupling constant strength $g_{ab}/g = 1.1$ and $g/(\hbar\omega_{\mathrm{ho}}x_{\mathrm{ho}}) = 5$.

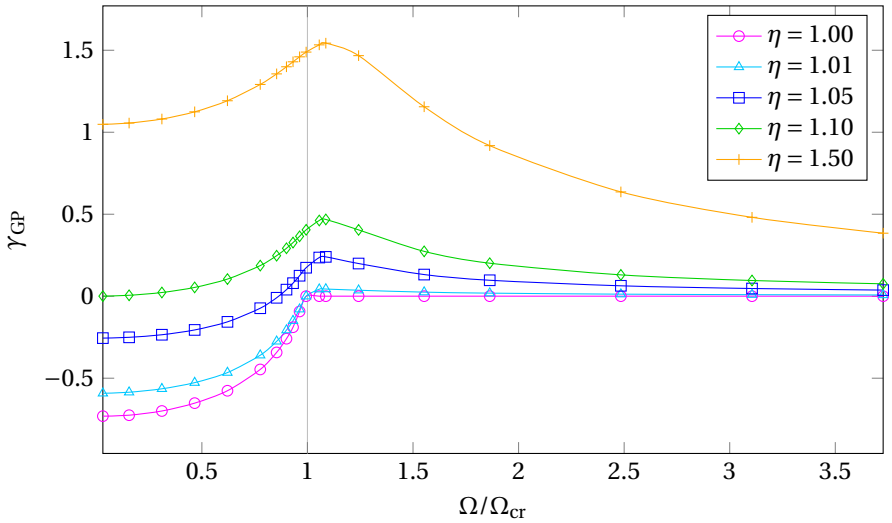

FIGURE 3.8: Kurtosis γ_{GP} for the minority component at different values of the narrowing factor η across phase transition. Values lower than zero correspond to configurations more flattened than the reference case (see Fig. 3.7 plot (a4)) while values bigger than zero correspond to sharper configurations.

η. For equal traps ($\eta = 1$) we see that above the critical point the kurtosis is zero: in this region, without any external perturbation, the system is globally and locally unpolarized and the two densities coincide. Below the critical point instead the minority component starts to flatten and the kurtosis drop below zero. The presence of a narrower trap for one of the components ($\eta > 1$) has the effect of sharpening the density profile of this component, thus increasing its kurtosis; the presence of the phase transition is still visible and, above the critical point the kurtosis falls again toward zero.

The problem of kurtosis is that it tells us nothing about the presence of a central hole in the densities. In order to characterize this factor we plot the second derivative in zero of the density of the majority component. As one can see in Figure 3.9, for η large enough, the second derivative starts from a negative value, for a interval of Ω values it becomes positive (thus indicating the presence of a hole) and then it falls again below zero reaching an asymptotic negative value that we call d_2 and that will play a role in a while. For $\eta - 1 \ll 1$ the trend is different, the hole does not appear in the majority component and instead the derivative decreases before saturating to d_2. The plot for $n_b''(0)$ is not shown because is the almost perfect mirror image of $n_a''(0)$ with the reflection axis at $n''(0) = d_2$. This means that the sum of the second derivatives is somehow conserved varying Ω and d_2 is the value the derivative takes for $\Omega \gg \Omega_{cr}$ when the two clouds coincide.

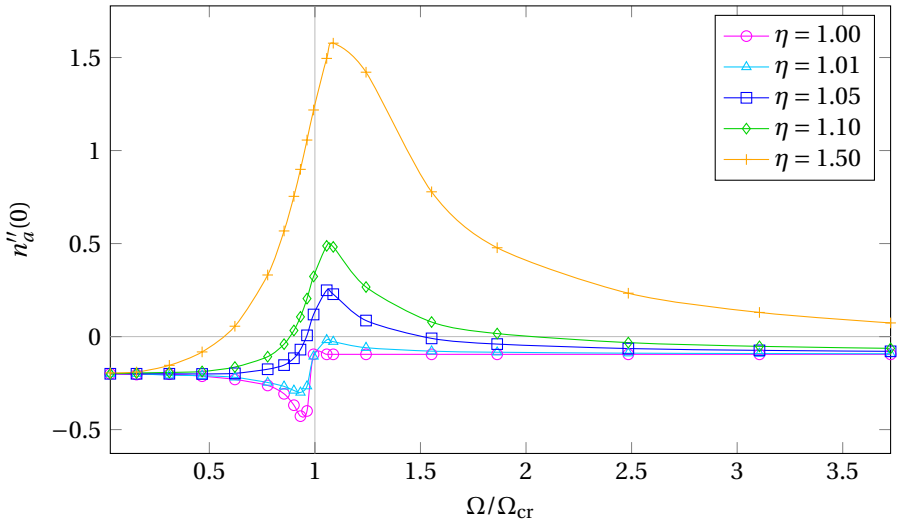

FIGURE 3.9: Second derivative of the density of majority component in $x = 0$ across phase transition. Values lower than zero indicate the presence of a central hole in the density.

3.5 Paramagnetic spin dipole mode

In this and in the next Section we study the response of the Rabi coupled mixture to an out-of-phase (spin) dipole perturbation. As we will see this response is very rich and captures many relevant phenomena related to the paramagnetic/ferromagnetic-like phase transition taking place in the system.

3.5.1 Static dipole polarizability

A relative component perturbation is accessible in cold gases by applying different trapping potentials for different atomic internal levels. In particular the spin-dipole configuration is realized by applying trapping potentials that have the same shape, but that are displaced for the two components of the gas by a quantity d

$$\begin{aligned} V_{a,b} &= \frac{1}{2} m {\omega_{ho}}^2 (x \pm d)^2 \\ &= \frac{1}{2} m\omega_{ho}^2 x^2 \pm m\omega_{ho}^2 x d + \mathrm{O}(d^2), \end{aligned} \tag{3.19}$$

where $d \ll x_{ho}$ and $x_{ho} = \sqrt{\hbar/(m\omega_{ho})}$ is the oscillator length associated with the traps.

The GP ground state solutions for the spinor gas in equal and displaced potentials is reported in Figure 3.10. For the sake of concreteness we take $g_{ab} > g$ in order to show the difference with a phase separated mixture.

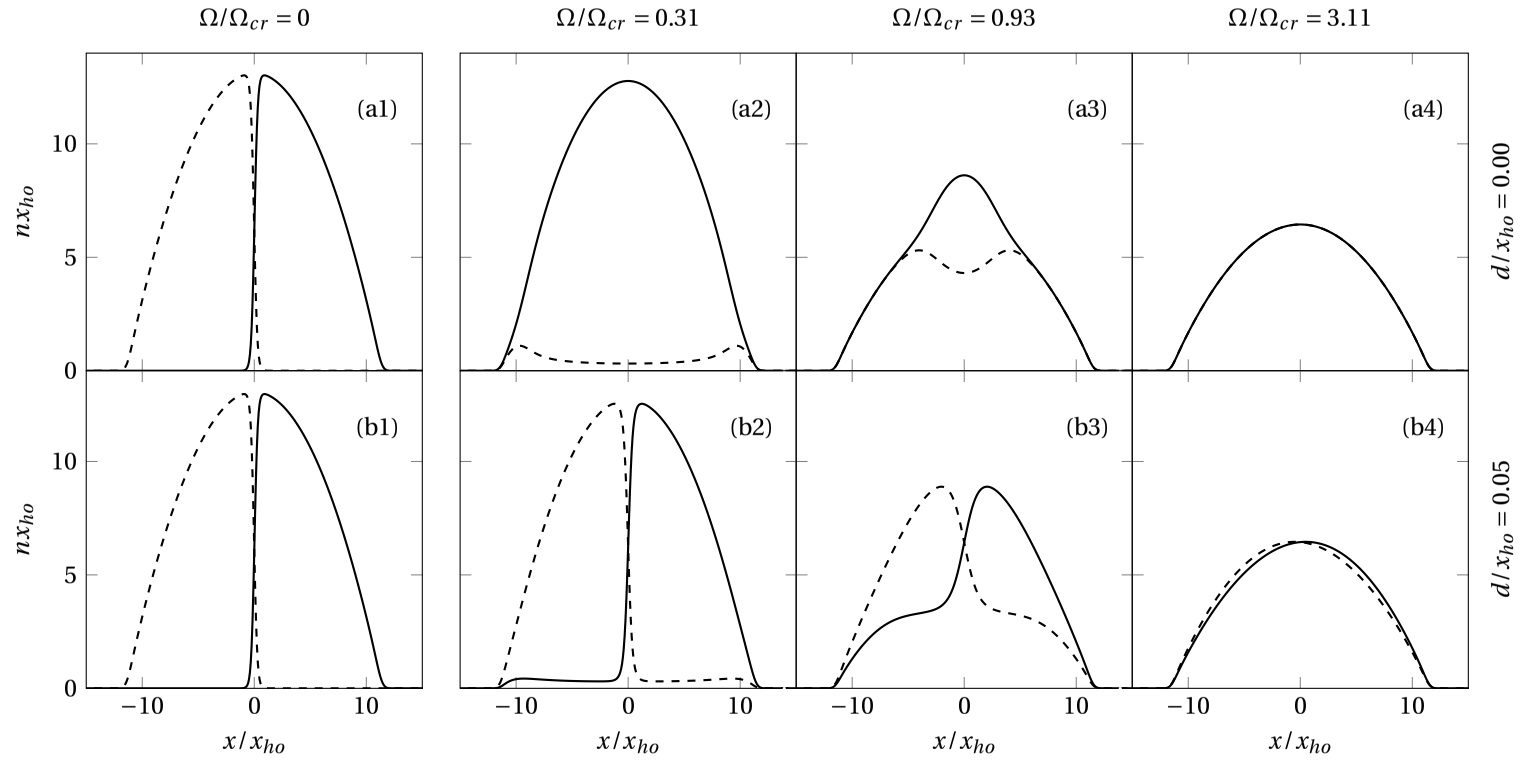

FIGURE 3.10: Ground states of a trapped coherently coupled Bose gas for different values of potential displacement d and Rabi coupling Ω. We use coupling constant strength $g_{ab}/g = 1.1$ and $g/(\hbar\omega_{\rm ho}x_{\rm ho}) = 5$. Plots (a1)-(a4) correspond to $d/x_{\rm ho} = 0$, while plots (b1)-(b4) to $d/x_{\rm ho} = 0.05$. For the ground state in panels 2, 3, and 4 we use the values $\Omega/\Omega_{cr} = 0.31, 0.93, 3.11$, respectively. For comparison we report also the ground state for a Bose-Bose mixture, i.e., $\Omega = 0$. In the latter case, with the number of particles in each component fixed, no global polarization appears, and the ground states (a1) and (b1) are essentially equal. The effect of quantum pressure can be clearly noticed in the plots (a2) and (a3) (analogues to Figure 3.6). In fact, the bifurcation points are not sharp as instead predicted by the Thomas-Fermi approximation.

When the traps are not displaced, $d = 0$ (row a), we see the features of the Ω-induced phase transition: below the critical value the linear coupling prevents the phase separation by creating a finite global polarization in the system (figure 3.10, plot (a2)); approaching the critical value the global polarization decreases (figure 3.10, plot (a3)) and above the critical value the gas is unpolarized (figure 3.10, plot (a4)). In contrast, a normal mixture without Rabi coupling ($\Omega = 0$) would be in a phase separated regime (figure 3.10, plot (a1)).

When instead the traps are displaced, $d \neq 0$ (row b), even a very small difference in the potentials has strong consequences. The ferromagnetic configurations become strongly polarized and as a result a domain wall is created at the center of the trap (figure 3.10, plot (b2) and (b3)). Since with different potentials the right-hand-side of Equation 3.5 is no more vanishing, the local polarization of the system is different from zero everywhere (a part for $x = 0$) and both for the ferromagnetic and paramagnetic cases (see figure 3.10, plot (b4)).

Notice also that without the Rabi coupling the ground state of the mixture in the phase separated regime is almost unchanged by the traps displacement (figure 3.10, plot (b1)).

In order to calculate the spin-dipole susceptibility we first determine the spin-dipole moment D, defined as

$$D = \frac{1}{N} \int x \, [n_a(x) - n_b(x)] \, \mathrm{d}x. \tag{3.20}$$

The spin-dipole susceptibility is then defined by the limit

$$\chi_{\mathrm{sd}} = \lim_{d \to 0} \frac{D}{\lambda} \tag{3.21}$$

where $\lambda = m\omega_{ho}^2 d$ is the perturbation associated with the spin-dependent component of the potential of Eq. (3.19).

In the global paramagnetic phase ($\Omega > \Omega_{cr}$) it is easy to obtain an analytical expression for χ_{sd} within local density approximation. In this case one can employ the energy functional

$$E = \int \left[{\chi_s}^{-1} (n_a - n_b)^2 - \lambda x (n_a - n_b) \right] \mathrm{d}x \tag{3.22}$$

relative to the spin degrees of freedom of the problem, where

$$\chi_{\mathrm{s}} = \frac{2}{g - g_{ab} + 2\Omega/n} \tag{3.23}$$

is the magnetic spin susceptibility for an homogeneous system of total density n (see, e.g., [39]). Since in the paramagnetic region the density profiles are very close to the

ones without the potentials displacement we can treat the density difference as a small quantity. Variation of the energy with respect to the spin density $(n_a - n_b)$ yields the result

$$n_a(x) - n_b(x) = x\lambda\chi_s[n_0(x)], \tag{3.24}$$

where $n_0(x)$ is the total density of the system in the GSU from Eq. (3.9). After substituting this expression into Eq. (3.20) the spin-dipole polarizability finally reads

$$\chi_{\mathrm{sd}} = \frac{1}{N}\int x^2\chi_s[n_0(x)] \tag{3.25}$$

After integration we obtain the result

$$\frac{D}{d} = \frac{g+g_{ab}}{g-g_{ab}}\left[1+f\left(\frac{\Omega}{(g-g_{ab})n_0}\right)\right] \tag{3.26}$$

for the dimensionless ratio $D/d = m\omega_{ho}^2\chi_{sd}$ where we used the notation $n_0 = n_0(0)/2$, being n_0 the maximum density of each component in the paramagnetic regime, and we have introduced the function

$$f(\alpha) = 3\alpha\left[1-(\sqrt{1+\alpha})\mathrm{arccoth}(\sqrt{1+\alpha})\right]. \tag{3.27}$$

Notice that the domain of the function $f(\alpha)$ to be real, i.e. $1/\alpha \geq -1$, is precisely the region in which the system is fully paramagnetic when we take $\alpha = \Omega/(g-g_{ab})n_0$ as in Eq. 3.26

A couple of comments are due on this result. First of all we consider the case of a normal Bose-Bose mixture, i.e. $\Omega \to 0$. In this case $f(\alpha \to 0) \to 0$ and thus the spin-dipole susceptibility is simply proportional to the magnetic susceptibility of equation (3.23). Therefore, also χ_{sd} diverges at the miscible/immiscible transition point $g_{ab} \to g^-$. Physically this is due to the fact that the two gases become globally immiscible at this point since the latter condition is density independent. As we will see in the next section, the divergence of the spin-dipole susceptibility leads to a zero frequency spin-dipole mode. At the same point but for finite Ω we have instead $f(\alpha \to \infty) \to -1+2/(5\alpha)$ and therefore $D/d = gn_0/(5\Omega)$.

By contrast, for finite Ω, the paramagnetic/ferromagnetic transition point, $g_{ab} = g+2\Omega/n_0$, depends on the density. This means that the spinor gas starts becoming ferromagnetic at the center of the trap only. The spin-dipole susceptibility, χ_{sd}, being density integrated, remains finite at the transition point (indeed $f(-1) = -3$) leading to a finite frequency for the spin-dipole frequency (see next Section). This behaviour is very general

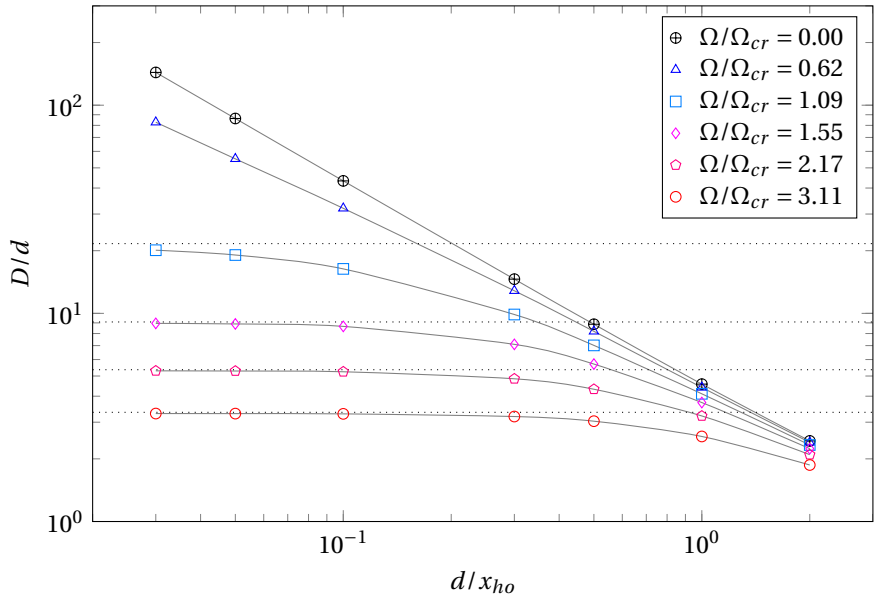

FIGURE 3.11: Dipole D as a function of traps displacement d for different values of Ω/Ω_{cr} and for $g_{ab}/g = 1.1$. Dotted lines are analytical results from equation (3.26) for the four bigger values of Ω, points are numerical data and grey full lines are only a guide for the eye.

and it has already been pointed out for the Stoner (or itinerant ferromagnetic) instability in the context of cold gases [70].

Above the critical point the response of the system is no longer linear. The system is partially ferromagnetic and has the tendency to form a magnetic domain wall at the centre of the trap.

A detailed analysis of the behaviour of D/d is shown in Figure 3.11 where we calculate numerically the spin-dipole of the gas as a function of the trap separation d with the choice $g_{ab}/g = 1.1$. Above the critical Rabi frequency we see that indeed linear response applies and the analytical expression of equation (3.26) works very well for low d. Notice that the spin-dipole moment allows for a clear identification of the phase transition point, above which the induced dipole moment D changes its behaviour as a function of d.

3.5.2 Sum rule approach for spin-dipole dynamics

In this Section we study the dynamics of the system in the paramagnetic phase. In particular we let the ground state obtained in displaced traps to evolve in time after we sud-

denly set the displacement to zero. Notice that for two independent condensates ($\Omega = 0$ and $g_{ab} = 0$) the spin-dipole frequency simply coincides with the trapping one, ω_{ho}.

As shown in Figure 3.10, plots (a4)-(b4), in the paramagnetic phase a small trap displacement corresponds to a small deviation in density profiles with respect to the ground states in same traps. This allows us to apply linear response theory in order to find an analytical expression for the spin-dipole frequency. In particular, a very powerful tool to estimate collective modes frequencies is the so called sum rule approach [71, 72], a method that has been successfully applied for the dynamics of both cold gases and nuclei.

Sum rules are defined for an operator $\hat{F}$ as

$$m_k(F) = \sum_n |\langle 0|\hat{F}|n\rangle|^2 \left(E_n - E0\right)^k, \tag{3.28}$$

and they represent the moments of the strength distribution function relative to $\hat{F}$. The sum rule approach has the merit of providing a direct way to obtain an upper bound of collective modes frequency through the ratio of different momenta, and therefore gives an understanding of the collective mode frequency in terms of static macroscopic quantities [72].

For the sake of concreteness we are here considering the response of the system to the application of the spin-dipole operator

$$\hat{S}_d = \sum_{i=1}^{N} x_i \hat{\sigma}_{z,i}, \tag{3.29}$$

and we want to use the energy weighted and the inverse energy weighted sum rules, i.e.,

$$\hbar^2 {\omega_{\mathrm{sd}}}^2 \leq \frac{m_1(\hat{S}_d)}{m_{-1}(\hat{S}_d)}. \tag{3.30}$$

The energy weighted one (m_1) can be easily rewritten in terms of a double commutator [72] as

$$m_1 = \frac{1}{2}\langle 0|\left[\hat{S}_d, [H, \hat{S}_d]\right]|0\rangle. \tag{3.31}$$

The only terms in the Hamiltonian that do not commute with $\hat{S}_d$ are the kinetic energy and the Rabi coupling that, as spinor operator, can be written as

$$H_R = -\Omega \sum_i \hat{\sigma}_{x,i}. \tag{3.32}$$

The first one gives the usual $N\hbar^2/(2m)$ contribution while the second one, using the commuting properties of Pauli matrices, can be easily evaluated to

$$\begin{aligned}\left[\hat{S}_d,[H,\hat{S}_d]\right] &= -\Omega\left[\sum_i x_i\hat{\sigma}_{z,i},\left[\sum_i \hat{\sigma}_{x,i},\sum_i x_i\hat{\sigma}_{z,i}\right]\right]\\ &= -2\Omega\mathrm{i}\left[\sum_i x_i\hat{\sigma}_{z,i},\sum_i x_i\hat{\sigma}_{y,i}\right]\\ &= 4\Omega\sum_i {x_i}^2\hat{\sigma}_{x,i}.\end{aligned} \tag{3.33}$$

Averaging on the ground state (in Thomas-Fermi approximation) we obtain

$$\begin{aligned}m_1 &= N\frac{\hbar^2}{2m}+8\Omega\int_o^{R_{TF}} x^2 n_0(x)\mathrm{d}x\\ &= \hbar\omega_{ho}{x_{ho}}^2\frac{N}{2}\left[1+\frac{8}{5}\frac{\Omega}{\hbar\omega_{ho}}(n_0 x_{ho})\frac{(g+g_{ab})}{\hbar\omega_{ho}x_{ho}}\right]\end{aligned} \tag{3.34}$$

The inverse energy weighted sum rule (m_{-1}) is instead directly proportional to the spin-dipole susceptibility of the ground state through the relation [72]

$$m_{-1} = \frac{N}{2}\chi_{\mathrm{sd}}, \tag{3.35}$$

so, using the definition of Equation (3.21) and the result of Equation (3.25), one obtains the following upper bound to the spin-dipole frequency

$${\omega_{\mathrm{sd}}}^2 = {\omega_{ho}}^2\left(\frac{g-g_{ab}}{g+g_{ab}}\right)\left[\frac{1+8\Omega n_0(g+g_{ab})/(5\hbar^2{\omega_{ho}}^2)}{1+f\left(\Omega/[(g-g_{ab})n_0]\right)}\right]. \tag{3.36}$$

We here remind that this is only an upper bound to the frequency and that the equality in Equation (3.30) is attained only when a single mode is excited in the system.

Before analysing the numerically extrapolated frequency values, we show in Figure 3.12 an example of motion of the two clouds. The last plot shows the dipole D as a function of time. As one can see, in general there is more than one mode (more than one frequency) excited in the system and this is reflected in snapshots for $t = 0$ and $t > 0$ of the first row. The density profiles in fact become slightly deformed with time evolution and some "surface" modes appear. The second row show the map of the density of component a as a function of time.

In Figure 3.13 the sum rule results are compared with the frequencies extrapolated by a numerical real time evolution of the Gross-Pitaevskii equations. The frequencies are extracted by the data via a Fourier analysis, the shown data points correspond to the maximum amplitude components of the Fourier spectrum.

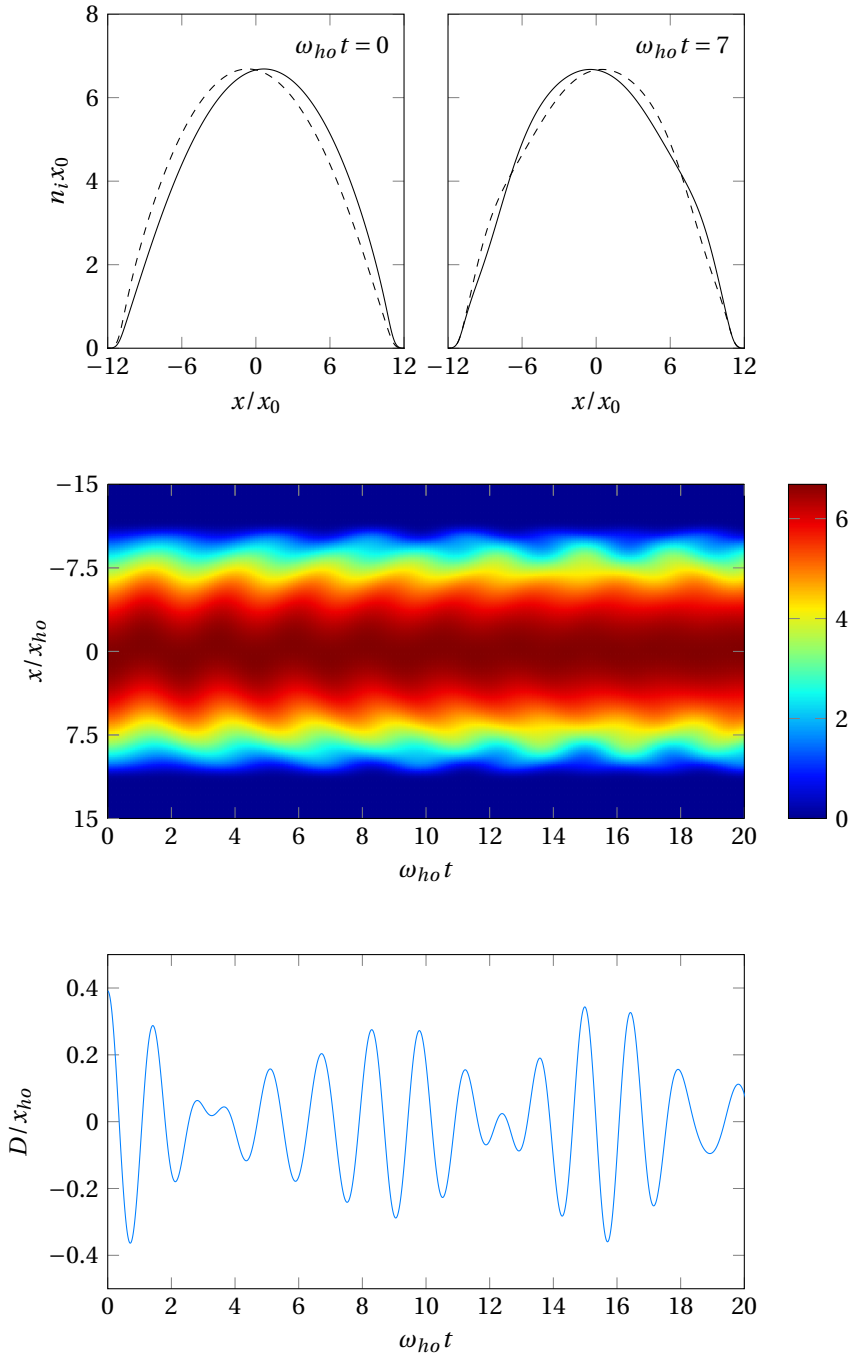

FIGURE 3.12: Spin dipole oscillations in paramagnetic regime for $\Omega = 1.5\hbar\omega_{ho}$ and $g_{ab} = 0.9g$. Top row: density snapshots at time $\omega_{ho}t = 0$ (left plot) and $\omega_{ho}t = 7$ (right plot). Central row: density map of component a as a function of time. Bottom row: time evolution of the dipole D. A movie of such dynamics can be seen in [73] or in the Supplementary Material of [23].

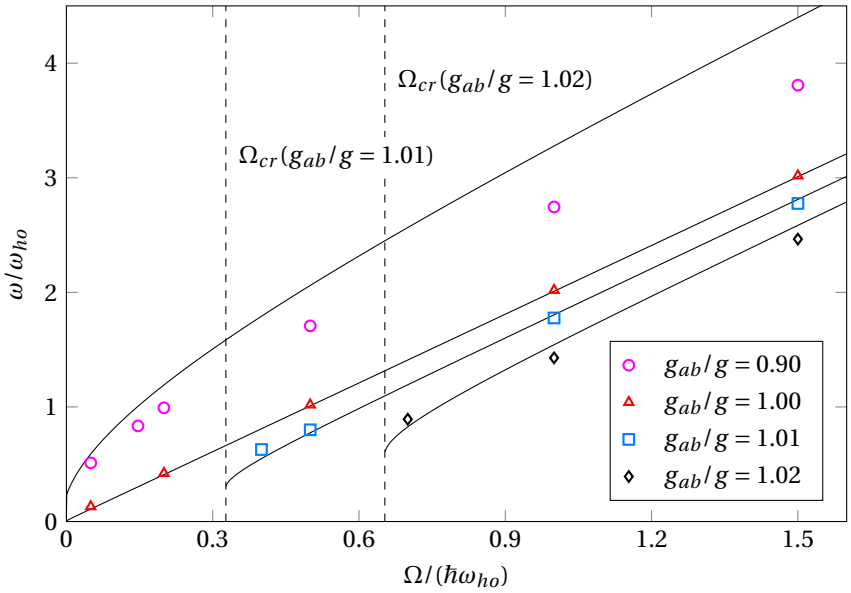

FIGURE 3.13: Spin-dipole frequency as a function of Ω for different values of interactions. Lines are analytical prediction from Equation (3.36) and points are numerical data. In order to have a fully paramagnetic phase for $g_{ab} > g$ we must require $\Omega \geq \Omega_{cr}$ (see text and Equation (3.8)), the values of Ω_{cr} for $g_{ab}/g = 1.01$ and $g_{ab}/g = 1.02$ are shown by dashed lines.

We first notice that at the transition point the frequency does not go to zero, since for the reasons explained in the previous section χ_{sd} (or m_{-1}) does not diverge at that point. Below the transition point no more data are shown because we enter in the ferromagnetic regime in which clearly linear response is no more applicable. If we compare these results with the mixture case (recovered sending $\Omega \to 0$), we see that in this situation the spin-dipole frequency vanishes close to the critical point following the law

$$\omega_{\mathrm{SD}}(\Omega = 0) = \omega_{\mathrm{ho}} \sqrt{\frac{g - g_{ab}}{g + g_{ab}}} \tag{3.37}$$

and the sum-rule approach gives the exact result as shown in Figure 3.14. This happens because the magnetic spin susceptibility diverges at the critical point (see Eq. (3.23)) and, since it does not depend any more on the density, the integration of Equation (3.25) does not fix the divergence.

Sum-rules give the exact result also for the intrinsic $SU(2)$ symmetric point $g_{ab} = g$ (and $\Omega \neq 0$ in general) as it can be seen in Figure 3.13 (red triangles). The magnetic energy of the spinor gas in this regime depends on the relative density only through the Rabi coupling, which breaks the $SU(2)$ symmetry of the system. The spin-dipole frequency

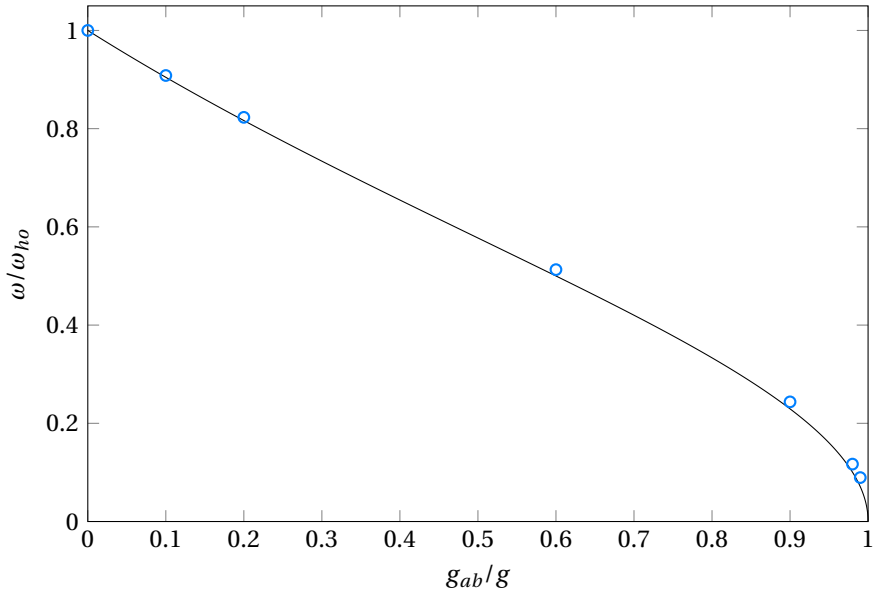

FIGURE 3.14: Spin-dipole frequency for a Bose-Bose mixture, i.e. $\Omega = 0$, as a function of g_{ab}/g. Line is the analytical result of Equation (3.37) and points are numerical data. In this case the spin-dipole frequency goes to zero at the phase separation point.

behaves in this case as

$$\hbar\omega_{\mathrm{SD}}(g_{ab} = g) = 2\Omega\sqrt{1 + \frac{5}{16}\frac{\hbar^2{\omega_{\mathrm{ho}}}^2}{g n_0 \Omega}} \tag{3.38}$$

which is essentially twice the Rabi frequency and therefore almost independent of the tapping frequency. The latter unusual result for a trapped gas is due to the correlation between the internal and external degrees of freedom that in particular leads to the modification of the f-sum rule, see Equation (3.34). An example of this dynamics exactly captured by sum-rule approach is given in Figure 3.15. The real time evolution shows clearly the presence of a single frequency, as opposed to $g_{ab} \neq g$ (see Figure 3.12).

In the more general case, when both Ω and $(g_{ab} - g)$ are different from zero, the frequency is given by the full Equation (3.36) in which both the coherent and the interspecies s-wave couplings play a role. In this more general case one observes that the sum-rule approach provides only an upper bound to the numerical solution, due to the appearance of more frequencies in the numerical signal resulting in beating effects (see Figure 3.12).

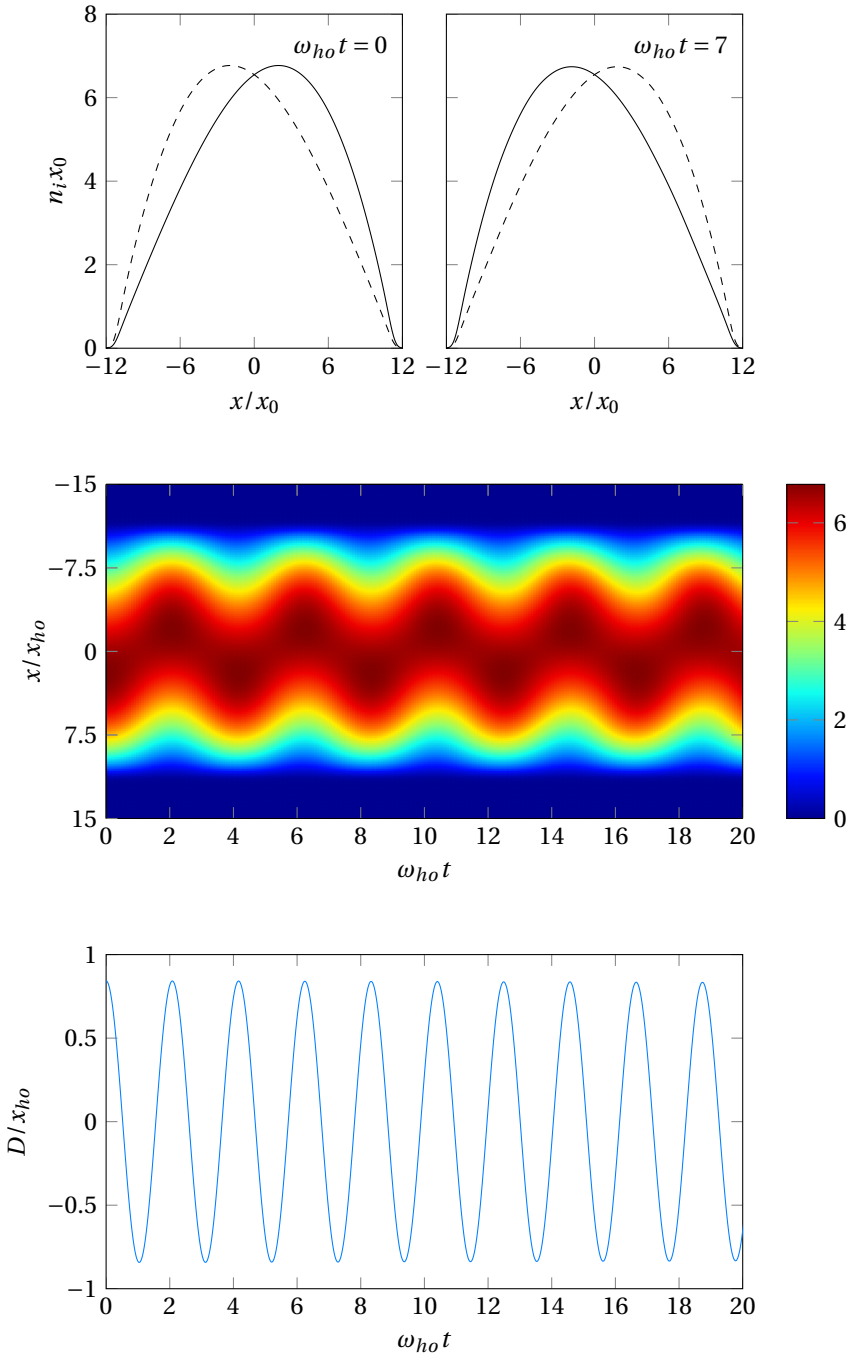

FIGURE 3.15: Spin dipole oscillations in paramagnetic regime for $\Omega = 1.5\hbar\omega_{ho}$ and $g_{ab} = g$. Top row: density snapshots at time $\omega_{ho}t = 0$ (left plot) and $\omega_{ho}t = 7$ (right plot). Central row: density map of component a as a function of time. Bottom row: time evolution of the dipole D. A movie of such dynamics can be seen in [74] or in the Supplementary Material of [23].

3.6 Ferromagnetic phase: ground state relaxation

In the previous section we studied the dynamics of a completely paramagnetic gas, i.e., $\Omega > \Omega_{cr}$. The behaviour is very different when the system is in the ferromagnetic regime. In this case the ground state of the system with equal trapping potentials is polarized as shown in Figure 3.10 plots (a2) and (a3). When the traps are shifted, the ground state is instead globally unpolarized ($N_a = N_b$) but with a large spin-dipole moment (depending on the values of Ω and d) as one can see in Figure 3.10, plots (b2) and (b3). Therefore, the initial state and the ground state are very far from each other. This circumstance results in a non-trivial and highly non-linear dynamics that clearly is no more captured by a sum-rule approach.

Let us first show in Figure 3.16 a typical dynamics in this regime. At the beginning, the spinor gas oscillates around the initial configuration, trapped in the unpolarized state. After a certain time, τ_{wait}, the domain wall starts moving and a finite polarization appears. The system then bounces back and forth between the initial magnetic state and its magnetic ground state to eventually relax to the latter one. The system is closed, energy conserving and still able, in the long time limit, to approach and select one of the two possible ground states. The final state obviously presents small oscillations around the true ground state. If the global polarization of the ground state is large, the effects of non-linearity and the number of bounces are large. When the system is slightly in the ferromagnetic regime, no bounces are observed and the system after τ_{wait} soon reaches its ground state. Figure 3.17 summarizes these different types of dynamics.

Notice that even if the system is isolated, it can approach in the long time limit an asymptotic steady state as a result of destructive interference of several time oscillating factors, present in the evolution of expectation values of observables. Specifically, in the case of a large and dense collection of frequencies, the interference phenomenon results in a dephasing mechanism similar to inhomogeneous dephasing. The total energy of the system is still conserved, the algorithm used (see Chapter 4) does not contains any dissipative mechanism and we explicitly check that the total energy does not change during the evolution. At the end of the real time evolution we get the ground state profile superposed with some high frequency perturbations carrying the extra energy.

As we have already mentioned, the initial configuration in the ferromagnetic case contains a domain wall at the centre of the trap. The properties of this domain wall clearly depends on the value of Ω, i.e. on how much is the system in the ferromagnetic phase. From Figure 3.17 one can easily see that also the waiting time τ_{wait} strongly de-

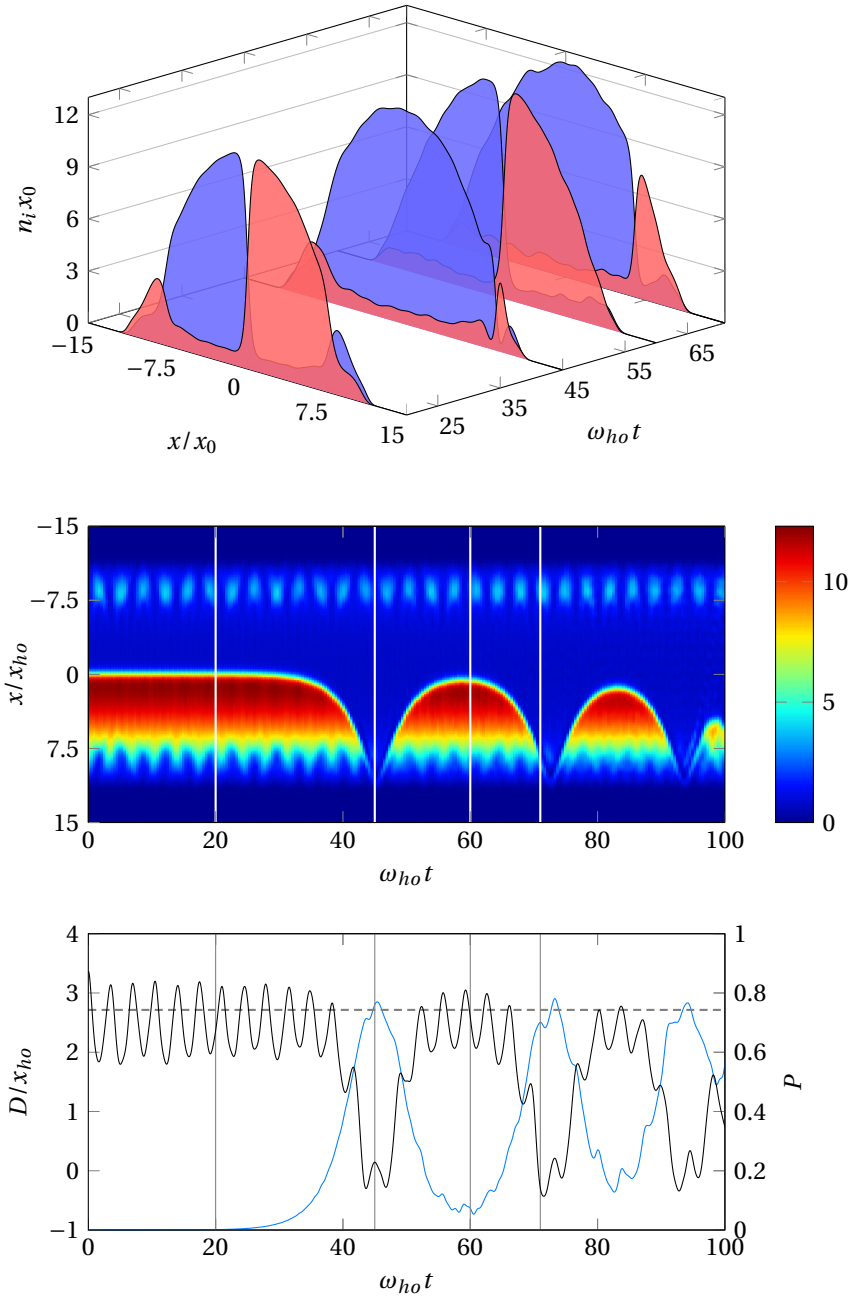

FIGURE 3.16: Spin dipole oscillations in ferromagnetic regime for $\Omega = 1.5\hbar\omega_{ho}$ and $g_{ab} = 1.1g$. Top row: density snapshots showing the evolution from the initial state ($\omega_{ho} t < 20$) to real ground state ($\omega_{ho} t = 45$) and the bouncing back an forth between these two states. Central row: density map of component a as a function of time. Bottom row: time evolution of the dipole D (black line, left y-axis) and of the polarization of the system (blue line, right y-axis). A movie of such dynamics can be seen in [75] or in the Supplementary Material of [23].

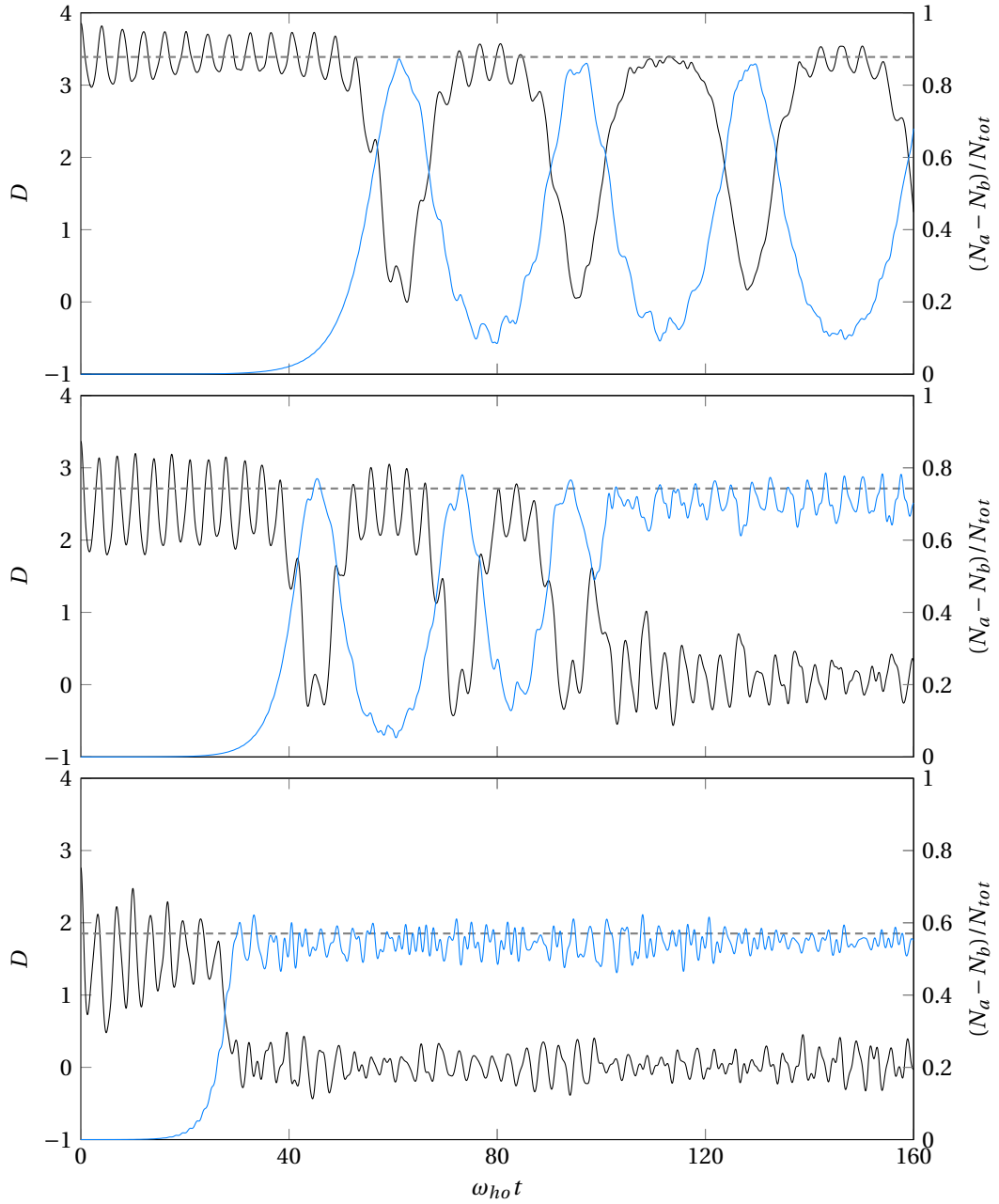

FIGURE 3.17: Real time spin-dipole oscillation (black solid lines, left y-axis) and polarization of the system (blue solid lines, right y-axis) as a function of time. Dashed lines represent the ground state polarization values. Parameters are $g_{ab} = 1.1g$, $g/(\hbar\omega_{ho}x_{ho}) = 5$ and $\Omega/(\hbar\omega_{ho}) = 1$ (top panel), $\Omega/(\hbar\omega_{ho}) = 1.5$ (middle panel) and $\Omega/(\hbar\omega_{ho}) = 2$ (bottom panel).

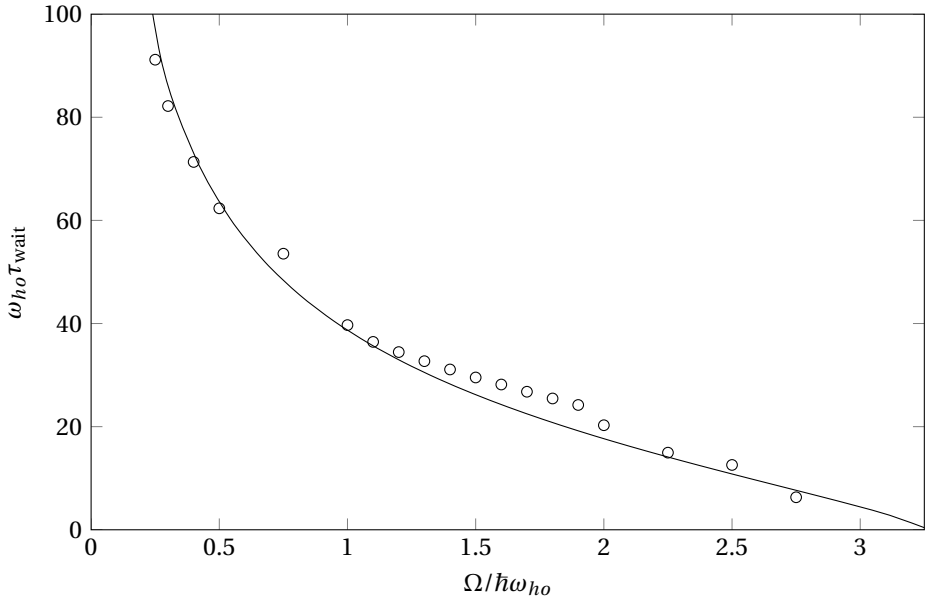

FIGURE 3.18: Waiting time τ_{wait} as a function of Ω. Points are numerical data and line is a fit to the data with fit function $A\sqrt{\sigma}$ where σ is the surface tension of equation (3.43).

pends on this parameter, so we looked for a relation between τ_{wait} and the energy characterizing the domain wall, that is its surface tension σ. In order to calculate the surface tension it is useful to first approximate the energy functional for the magnetization of our spinor condensate with a classical one-dimensional ϕ^4 theory (Ginzburg-Landau for the phase transition) [76]. In the symmetric case $g_a = g_b = g$ and considering a uniform total density $n = n_a + n_b$, the relative density or magnetization $M = (n_a - n_b)/n$ enters in the energy density as

$$E(M) = \int \mathrm{d}x \left[\frac{\hbar^2 n (\nabla M)^2}{8m(1-M^2)} + W(M) \right], \tag{3.39}$$

where the first term arises from the kinetic energy and the term

$$W(M) = \frac{n^2}{4}(g - g_{ab})M^2 - \Omega n\sqrt{1-M^2}, \tag{3.40}$$

accounts for the density-density interaction and for the coherent Rabi coupling. For a homogeneous magnetization, minimisation $\delta E/\delta M = 0$ leads to the usual equation for the paramagnetic- and ferromagnetic-like states. From equation (3.39) one sees that close to the phase transition, i.e. $M \ll 1$, a standard Ginzburg-Landau theory for the order parameter M is valid, since in this case the kinetic energy term is just the square of

the gradient of M and the effective potential takes the usual quadratic plus quartic form

$$W(M) = \frac{n^2}{4}\left(g - g_{ab} + \frac{2\Omega}{n}\right)M^2 + \frac{n\Omega}{8}M^4 \tag{3.41}$$

$$\equiv \frac{r}{2}M^2 + \frac{u}{4}M^4. \tag{3.42}$$

As usual, the $\mathbb{Z}_2$ symmetry broken ground state is obtained for $r < 0$. A kink in M is the field solution interpolating between the two degenerate minima. Its surface tension, σ, which coincides with its energy in a one-dimensional situation, can be easily computed [77] yielding the result

$$\sigma \propto \sqrt{\frac{\hbar^2 n^2}{m}}\frac{|r|^{3/2}}{u} \propto \sqrt{\frac{\hbar^2 n^2}{m}}\frac{\left|(g - g_{ab})n + 2\Omega\right|^{3/2}}{\Omega} \tag{3.43}$$

From an intuitive point of view, the higher is the energy of the domain wall, σ, the more time is required for the system to relax from the kink into one of the ground states of the system; accordingly, a relation of proportionality between the waiting time and σ is expected. A standard field theoretical estimate of the average tunnelling time cannot be straightforwardly performed since only close to the transition does our field theory resemble an ordinary ϕ^4 theory; for this reason, we took advantage of a numerical fit to extract with surprising accuracy the relation, $\tau_{\text{wait}} \propto \sqrt{\sigma}$, as shown in Figure 3.18.

The fact that for $\Omega \to 0$ the waiting time diverges can be easily understood noticing that the initial state and the ground state are very far from each other (see, e.g., panels (a2) and (b2) of figure 3.10). Eventually, in the strict $\Omega = 0$ case, the system cannot reach the totally polarized ground state and it remains in the phase separated state (see panels (a1) and (b1) of figure 3.10).

CHAPTER

4 Time evolving split-operator method

The great majority of the data presented in this Thesis are obtained by means of the split-operator method. We use its imaginary time evolution version for finding ground states and its real time evolution one for simulating the dynamics. In this Chapter we derive the main expressions and we give the details of some tricks implemented in our program to make the algorithm more efficient.

Contents

4.1 Real vs. imaginary time

Let us call $\{|\psi_n\rangle\}$ a basis set of non-degenerate eigenfunctions of an Hamiltonian H. They fulfil the eigenvalue equation

$$H|\psi_n\rangle = E_n|\psi_n\rangle, \tag{4.1}$$

with E_n the energy corresponding to the state $|\psi_n\rangle$. We denote the ground state as ψ_0 and the corresponding energy, that is the smallest of the set of eigenvalues $\{E_n\}$, as E_0. Given an arbitrary wave function $|\Phi\rangle$, its expansion in terms of the basis of H is given by

$$|\Phi\rangle = \sum_n \langle\psi_n|\Phi\rangle|\psi_n\rangle = \sum_n a_n|\psi_n\rangle. \tag{4.2}$$

The wave function $|\Phi\rangle$ evolves in time according to H. At a time t the time evolution will be given by the evolution operator, $U(t) = \mathrm{e}^{-\mathrm{i}Ht/\hbar}$, as

$$|\Phi(t)\rangle = \mathrm{e}^{-\mathrm{i}Ht/\hbar}|\Phi(0)\rangle, \tag{4.3}$$

so, in order to find the real time evolution of our starting wave function $\Phi(0)$, we just need a way of exponentiating of the Hamiltonian H applied to it (see next Section).

Equation (4.3) can be rewritten as

$$|\Phi(t)\rangle = \mathrm{e}^{-\mathrm{i}Ht/\hbar}\sum_n a_n|\psi_n\rangle = \sum_n a_n \mathrm{e}^{-\mathrm{i}E_n t/\hbar}|\psi_n\rangle. \tag{4.4}$$

We can now set the time t to be imaginary (whence the name of imaginary time method) and define a new time $\tau \in \mathbb{R}$ where $t = -\mathrm{i}\hbar\tau$. We then separate the summation over n in Eq. (4.4) into a term containing $n = 0$ and the summation over the rest. Notice that this introduction makes the operator in the exponential non-unitary, which means that the norm will not in general be preserved. In terms of τ, Eq. (4.4) is rewritten as

$$|\Phi(\tau)\rangle = a_0\mathrm{e}^{-E_0\tau}|\psi_0\rangle + \sum_{n\neq 0} a_n \mathrm{e}^{-E_n\tau}|\psi_n\rangle \tag{4.5}$$

Since the energies, by definition, fulfill $E_0 < E_1 < \ldots < E_n < \ldots$, in the limit $\tau \to \infty$ the contribution of the states with $n \neq 0$ will be exponentially killed compared to the contribution of $n = 0$. The imaginary time version of the method is based exactly on this fact that we can state as:

$$\lim_{\tau\to\infty} |\Phi(\tau)\rangle \propto \mathrm{e}^{-E_0\tau}|\psi_0\rangle. \tag{4.6}$$

Therefore, for an infinite time, the wave function converges to the ground state of the system. This is true for whatever initial wave function we are using, provided that it has some non-zero component of the ground state, that is $a_0 \neq 0$ in Eq. (4.2).

Before proceeding we must stress one thing. The derivation of this Section has been done for a linear system while the Hamiltonian in Gross-Pitaevskii equation contains non linear terms. However, it has been proven [78, 79] that this method works very well also for non-linear Schrödinger-like problems assuming that sufficiently small time and spatial steps are chosen.

4.2 Splitting of the evolution operator

In order to propagate the initial wave function in real or imaginary time we first split the evolution operator to time τ in N pieces corresponding to time intervals $\Delta\tau$

$$e^{-H\tau} = \left(e^{-H\tau/N}\right)^N = \underbrace{e^{-H\Delta\tau}e^{-H\Delta\tau}\dots e^{-H\Delta\tau}}_{N \text{ times}}. \tag{4.7}$$

We considered here the imaginary time evolution but the same holds with almost no changes for real time.

At this point the only problem is to find a way of exponentiate H. For doing this we refer to our specific Hamiltonian for a BEC mixture possibly with Rabi coupling between the two species:

$$H = \begin{pmatrix} -\frac{\hbar^2\nabla^2}{2m} + V_a + g_a|\psi_a|^2 + g_{ab}|\psi_b|^2 & \Omega \\ \Omega^* & -\frac{\hbar^2\nabla^2}{2m} + V_b + g_b|\psi_b|^2 + g_{ab}|\psi_a|^2 \end{pmatrix} \tag{4.8}$$

To simplify our algorithm we divide our Hamiltonian in a kinetic term H_K, a potential term H_V and a Rabi term H_R,

$$H_K = \begin{pmatrix} -\frac{\hbar^2\nabla^2}{2m} & 0 \\ 0 & -\frac{\hbar^2\nabla^2}{2m} \end{pmatrix} \tag{4.9}$$

$$H_V = \begin{pmatrix} V_a + g_a|\psi_a|^2 + g_{ab}|\psi_b|^2 & 0 \\ 0 & V_b + g_b|\psi_b|^2 + g_{ab}|\psi_a|^2 \end{pmatrix} \tag{4.10}$$

$$H_R = \begin{pmatrix} 0 & \Omega \\ \Omega^* & 0 \end{pmatrix} \tag{4.11}$$

and we use the Lie-Trotter-Suzuki formula to split the exponential as

$$e^{-H\Delta\tau} = e^{-H_K\Delta\tau}e^{-H_V\Delta\tau}e^{-H_R\Delta\tau} + o(\Delta\tau^2). \tag{4.12}$$

In particular, in order to avoid the presence of a derivative in the exponent, we treat the kinetic term in Fourier space [78, 79] using the “Fastest Fourier Transform in the West” (FFTW) library [80].

4.3 Algorithm implementation

The implementations of the two versions of the algorithm are very similar. One has to proceed as follows:

1. Start with two initial normalized guess functions, $\psi_a(x)$ and $\psi_b(x)$.

2. Transform them to the Fourier space by means of FFTW

$$\psi_i(x) \mapsto \tilde{\psi}_i(k). \tag{4.13}$$

3. Multiply the exponential of the transformed kinetic part of the Hamiltonian and then transform back to real space

$$\tilde{\psi}_i(k) \mapsto \mathrm{e}^{-k^2\Delta\tau/2}\tilde{\psi}_i(k), \tag{4.14}$$

$$\tilde{\psi}_i(k) \mapsto \psi_i(x). \tag{4.15}$$

4. Multiply the exponential of the potential part of the Hamiltonian

$$\psi_i(x) \mapsto \mathrm{e}^{-(V_i+g_i|\psi_i(x)|^2+g_{ab}|\psi_j(x)|^2)\Delta\tau}\psi_i(x). \tag{4.16}$$

5. Multiply the exponential of the Rabi part of the Hamiltonian. Since it is not diagonal one must explicitly calculate the exponential of the matrix that gives two different results for imaginary and real time evolutions

$$\psi_i(x) \mapsto \begin{cases} \cosh(\Omega\Delta\tau)\psi_i(x) - \sinh(\Omega\Delta\tau)\psi_j(x) & \text{if imaginary time evolution} \\ \cos(\Omega\Delta t)\psi_i(x) - \mathrm{i}\sin(\Omega\Delta t)\psi_j(x) & \text{if real time evolution} \end{cases} \tag{4.17}$$

6. For imaginary time evolution normalize the obtained wave functions $\psi_i(x,\Delta\tau)$ since in this case the evolution operator is not unitary and the norm is not preserved.

7. Repeat the process n times until convergence (imaginary time evolution) or desired time t (real time evolution) is reached.

The time steps have to be small enough to ensure the stability of the algorithm and to let the system evolve smoothly but large enough to make this process efficient.

4.4 Convergence of imaginary time evolution

In imaginary time evolution the convergence of the solution to the ground state of the system is not easily assessed. A possibility is to track the energy change (or the change in chemical potential) between iterations. Since in general this quantity is small between two subsequent iterations, one can track the energy change every, say, 50 iterations and establish a "self-made" convergence criterion. When the energy change is very small (in our simulations, it is typically of the order of $10^{-12}E_{tot}$, with E_{tot} the total energy) we say that the algorithm is converged and that we have found the ground state of H.

Sometimes, if the energy of the ground state is very close to the energy of an excited state or the imaginary time step is large or there is some symmetry of the initial wave function that has to be broken, the algorithm can stay in a false minimum for an amount of time that can be also very large, looking as if it was already converged to the ground state (this is sometimes called a metastable solution). There are several possibilities to deal with this situation. One of them is to initialize the algorithm with a different trial function: from random numbers, from a particular shape (for instance, from a Thomas-Fermi profile in the case of BEC problems), etc. Another possibility is to reduce the imaginary time step or the grid spacing when the energy change between two iterations becomes smaller than some quantity. A third possibility is to leave the program running for a very long time. We have applied the first and third methods, which are easier to implement, in several of the calculations presented in this Thesis.

Metastable solutions are not always a problem that has to be solved but instead can be very useful, as in the case of persistent currents (Section 2.3). In that situation we explicitly count on the fact that the algorithm would remain trapped in a false ground state (the one with a current different from zero) in order to distinguish between stable and not stable states and to get a state with a current from which calculate its real time evolution.

4.5 Algorithm with dissipation term

The real time version of the algorithm as it was presented in the last sections clearly conserves the energy. This is not always a good thing since sometimes one needs to study the evolution of the system from a metastable or excited state to the ground state therefore to a state with a lower energy. With the standard version of the time evolving split-operator method this can not be done and one gets the ground state with superposed a lot of ex-

citations carrying the extra energy. Furthermore, as already discussed in the previous Section, the imaginary time version of the algorithm can got stuck in a local minimum.

In numerical simulation of GP equations this obstacle can be overcome adding a dissipation term γ to them

$$(\mathrm{i}-\gamma)\hbar\frac{\partial\psi}{\partial t} = H\psi. \tag{4.18}$$

The parameter γ is chosen phenomenologically and it represents an exchange of particles and energy between the condensate and a reservoir. With the addition of dissipations in the code the norm of the wave function is no more preserved neither with real time evolution so, at the end of every step, one must renormalize the state to the total atom number or use a time-dependent chemical potential $\mu(t)$.

In this Thesis we used this method for checking the results on partial stability of persistent currents obtained with the imaginary time evolution algorithm (see Section 2.3). We inserted a dissipation parameter $\gamma = 0.8$ in analogy to what has been done in Ref. [55] and the wave functions have been renormalized at every time step to the initial number of particles following what was done in Ref. [81]. We have also added a very small random noise to the potentials to make the energetic instability appear in shorter time scale checking that this does not change the results obtained without any noise.

4.6 Virial theorem

A useful criterion for checking the correctness and the convergence of a code for solving a GP equation is the virial theorem. Its formulation is very simple and we recall here the main step of its derivation.

If we consider a stationary solution of the Gross-Pitaevskii equation, the energy (see Eq. (1.17)) is a functional of the density and can be rewritten as

$$E[n] = \int \mathrm{d}\mathbf{r}\left[\frac{\hbar^2}{2m}\left|\nabla\sqrt{n}\right|^2 + nV_{\mathrm{ext}} + \frac{gn^2}{2}\right] \tag{4.19}$$

where we can identify three different contributions to the total energy that are respectively the kinetic, external potential and interaction one:

$$E_{\mathrm{kin}} = \int \mathrm{d}\mathbf{r}\,\frac{\hbar^2}{2m}\left|\nabla\sqrt{n}\right|^2, \qquad E_{\mathrm{ext}} = \int \mathrm{d}\mathbf{r}\; nV_{\mathrm{ext}}, \qquad E_{\mathrm{int}} = \frac{g}{2}\int \mathrm{d}\mathbf{r}\; n^2. \tag{4.20}$$

Since the energy functional is stationary for any variation of the the function ψ around the solution ψ_0 of the GP equation, one can choose a scaling transformation and impose

that the energy variation associated with this transformation vanishes at first order in some parameter. We will use the following transformation:

$$\psi(x_1, \dots, x_D) = (1+\nu)^{D/2}\psi_0\left[(1+\nu)x_1, \dots, (1+\nu)x_D\right], \tag{4.21}$$

$$n(x_1, \dots, x_D) = (1+\nu)^{D} n_0\left[(1+\nu)x_1, \dots, (1+\nu)x_D\right]. \tag{4.22}$$

The virial theorem tell us that $(E[n] - E[n_0])/\nu = 0$ so what we have to calculate are the different contributions to $E[n]$ at first order in ν. In doing so it is useful to change the variable of integration from $\mathbf{r}$ to $\mathbf{r}' = (1+\nu)\mathbf{r}$.

We start from the kinetic energy term giving the details of the calculation. For the other two contributions the procedure is similar and we will give only some comment.

$$\begin{aligned} E_{\text{kin}}[n] &= \int \mathrm{d}\mathbf{r} \frac{\hbar^2}{2m} \left|\nabla\sqrt{n(\mathbf{r})}\right|^2 \\ &= \int \mathrm{d}\mathbf{r}' (1-\nu)^{-D} \frac{\hbar^2}{2m} \left|(1-\nu)\nabla'\sqrt{(1-\nu)^D n_0(\mathbf{r}')}\right|^2 \\ &= \int \mathrm{d}\mathbf{r}' \frac{\hbar^2}{2m} (1-\nu)^2 \left|\nabla'\sqrt{n_0(\mathbf{r}')}\right|^2 \\ &= (1-\nu)^2 E_{\text{kin}}[n_0] \end{aligned} \tag{4.23}$$

For the interaction term we have a $(1+\nu)$ factor with power $2D$ arising from the square density and a factor with power $-D$ arising from the integration variable giving:

$$E_{\text{int}}[n] = (1+\nu)^D E_{\text{int}}[n_0]. \tag{4.24}$$

For the external potential contribution things are a little more complicated because now the result depends on the particular potential choice. For the harmonic one we have a $(1-\nu)^{-2}$ arising from the r^2 term, a factor with power D from the density and on with power $-D$ from the integration variable, giving:

$$E_{\text{ho}}[n] = (1+\nu)^{-2} E_{\text{ho}}[n_0]. \tag{4.25}$$

More complicated potentials will be treated in the next section.

Finally, expanding at the first order in ν, we obtain

$$\frac{E[n] - E[n_0]}{\nu} = 2E_{\text{kin}} - 2E_{\text{ho}} + DE_{\text{int}} = 0. \tag{4.26}$$

Since this relation must be satisfied by any solution of the GP equation, one can calculate it sometimes during the simulation to check convergence of the code and eventually the presence of errors.

4.6.1 Toroidal potential: central Gaussian barrier

The toroidal shape of the trapping potential can be obtained using a normal harmonic potential plus a Gaussian one placed at the centre of the previous:

$$V_{\text{ext}}(r) = \frac{1}{2}m\omega^2 r^2 + V_0 \mathrm{e}^{-2r^2/\sigma^2}. \tag{4.27}$$

Let us start by writing this potential as a function of ν and expand it to the first order.

$$\begin{aligned} V_{\text{ext}}(r',\nu) &= \frac{1}{2}m\omega^2 r'^2(1+\nu)^{-2} + V_0 \exp\left[-\frac{2r'^2}{\sigma^2}\frac{1}{(1+\nu)^2}\right] \\ &\simeq V_{\text{ext}}(r') - 2\nu\left[V_{\text{ext}}(r') - \left(1+\frac{2r'^2}{\sigma^2}\right)V_0\mathrm{e}^{-2r'^2/\sigma^2}\right] \end{aligned} \tag{4.28}$$

Using this expression in the calculation of the energy we get

$$\begin{aligned} E_{\text{ext}}[n] &= \int \mathrm{d}\mathbf{r}' n_0 V_{\text{ext}}(r') - 2\nu\int \mathrm{d}\mathbf{r}' n_0 V_{\text{ext}}(r') + 2\nu\int \mathrm{d}\mathbf{r}' n_0\left(1+\frac{2r'^2}{\sigma^2}\right)V_0\mathrm{e}^{-2r'^2/\sigma^2} \\ &= E_{\text{ext}}[n_0] - 2\nu E_{\text{ext}}[n_0] + 2\nu\int \mathrm{d}\mathbf{r}' n_0\left(1+\frac{2r'^2}{\sigma^2}\right)V_0\mathrm{e}^{-2r'^2/\sigma^2}. \end{aligned} \tag{4.29}$$

So in this case the virial theorem for this type of potential reads:

$$2E_{\text{kin}} - 2E_{\text{ext}} + DE_{\text{int}} + 2\int \mathrm{d}\mathbf{r}' n_0\left(1+\frac{2r'^2}{\sigma^2}\right)V_0\mathrm{e}^{-2r'^2/\sigma^2} = 0. \tag{4.30}$$

4.6.2 Toroidal potential: displaced harmonic trap

Another way to obtain the toroidal shape is using a normal harmonic potential centred in a circle or radius R:

$$V_{\text{ext}}(r) = \frac{1}{2}m\omega^2\left(\sqrt{r^2}-R\right)^2. \tag{4.31}$$

Also in this case let us start by writing the potential as a function of ν and expand it to the first order.

$$\begin{aligned} V_{\text{ext}}(r',\nu) &= \frac{1}{2}m\omega^2\left(\sqrt{r'^2}(1+\nu)^{-1}-R\right)^2 \\ &\simeq V_{\text{ext}}(r') - \nu\left[2V_{\text{ext}}(r') - m\omega^2\left(R^2 - \sqrt{r'^2}R\right)\right] \end{aligned} \tag{4.32}$$

Using this expression in the calculation of the energy we get

$$\begin{aligned} E_{\text{ext}}[n] &= \int \mathrm{d}\mathbf{r}' n_0 V_{\text{ext}}(r') - 2\nu\int \mathrm{d}\mathbf{r}' n_0 V_{\text{ext}}(r') + \nu\int \mathrm{d}\mathbf{r}' n_0 m\omega^2\left(R^2 - \sqrt{r'^2}R\right) \\ &= E_{\text{ext}}[n_0] - 2\nu E_{\text{ext}}[n_0] + \nu\int \mathrm{d}\mathbf{r}' n_0 m\omega^2\left(R^2 - \sqrt{r'^2}R\right). \end{aligned} \tag{4.33}$$

So the virial theorem for this type of potential reads:

$$2E_{\text{kin}} - 2E_{\text{ext}} + DE_{\text{int}} + \int \mathrm{d}\mathbf{r}' n_0 m\omega^2 \left(R^2 - \sqrt{r'^2}R\right) = 0. \tag{4.34}$$

CHAPTER

5 Tensor Network methods: Matrix Product State algorithm

In this last Chapter we introduce a numerical method useful in studying ultracold gases on a lattice, namely Tensor Network method. On contrary of Gross-Pitaevskii equation and algorithms for solving it, it takes correctly into account quantum correlations. Here we give a brief introduction of the theory behind this method without entering too much into the details of the implementation. In addition we compare two different ways of time evolving a quantum state written in terms of a tensor network, we apply these two methods to some literature results and we analyse their performances.

Contents

In recent years Tensor Network (TN) methods have become increasingly popular to simulate strongly correlated systems. In these methods the wave function of the system is described by a network of interconnected tensors. To make a practical comparison, the DNA is the fundamental building block of a person in the same way as the tensor is the building block of a quantum state. Therefore we could say that the tensor is the DNA of the wave function in the sense that the whole wave function can be reconstructed from it just following some simple rules. The glue that keeps the tensors together is the entanglement between them. More precisely TN techniques offer an efficient description of wave function based on the entanglement content in it. The amount and structure of entanglement is, as we will see later, a consequence of the chosen network pattern and of the parameters of the tensors. The most famous example of a TN method is the Density Matrix Renormalization Group (DMRG) [82, 83, 84, 85] introduced by White in 1992.

5.1 Advantages

All the existing numerical techniques have their own limitations. For example mean-field theory fails to incorporate faithfully the effect of quantum correlations in the system; exact diagonalization of the quantum Hamiltonian is restricted to systems of small size; quantum Monte Carlo algorithms suffer from the sign problem, etc. As we will see, the main limitation of TN methods is due to the amount and structure of entanglement in quantum many-body states. But this is a new sort of limitation in a computational method and it extends the range of models that can be simulated in new directions.

The bigger advantage is related to the size of the Hilbert space. If we take a system of N spin-1/2 particles the dimension of the Hilbert space is 2^N which is exponentially large in the number of particles. Therefore representing a quantum state by giving the coefficients of its wave function in some basis is a very inefficient representation. Luckily enough, not all the states of the Hilbert space are equal but some of them are more relevant than others. In particular, one can prove that low-energy eigenstates of a gapped Hamiltonian with local interactions obey the so-called area law for the entanglement entropy. This means that the entanglement entropy of a region of space tends to scale as the size of the boundary of the region and not as its volume. Now imagine to pick a state at random from the Hilbert space. It will most likely has an entanglement entropy between subregions that scales like the volume and not like the area. This means that low-energy states of realistic Hamiltonians are heavily constrained by locality so that they must obey the entanglement area law.

The manifold containing the states that satisfy area law is just an exponentially small corner of the whole Hilbert space and this is the point in which TN methods come in play. TN states are in fact the family of states that targets the corner of most relevant states. Thus it is natural to use TN to describe low-energy states of realistic Hamiltonians and it is also natural to use them in Renormalization Group methods where the goal is precisely to discard all the degrees of freedom that are not relevant in describing the system.

Another consequence of having a so big Hilbert space is that also the manifold of states that can be reached evolving a quantum many-body state for a time $O(\text{poly}(N))$ with a local Hamiltonian is exponentially small. This means that, given some initial state that most likely will belong to the relevant corner of area law states, most of the Hilbert space is unreachable in practice. This is the reason why sometimes the Hilbert space is referred to as a convenient illusion [86]: it is convenient from a mathematical point of view but physically it is an illusion because no one will ever see most of it.

5.2 Matrix Product States

Before going to Matrix Product States (MPS) let's introduce some notation and representation of tensors and tensor networks.

For our purposes a tensor is a multidimensional array of complex numbers. The rank of a tensor is the number of indices. Thus, a rank-0 tensor is a scalar (a), a rank-1 tensor is a vector (a_α) and a rank-2 tensor is a matrix ($A_{\alpha\beta}$). We can contract an index, that is summing over all the possible values of the repeated indices of a set of tensors. For instance, the matrix product

$$C_{\alpha\gamma} = \sum_{\beta=1}^{D} A_{\alpha\beta} B_{\beta\gamma} \tag{5.1}$$

is the contraction of index β. Indices that are not contracted are called open indices. In the following, when the summation range is obvious, we will use the convention that repeated indices hide an implicit summation.

A tensor network is a set of tensors where some, or all, of its indices are contracted according to some specific pattern. If the contraction leaves no open indices the result is a scalar, otherwise the result is another tensor.

A very useful way of representing TN is to introduce a diagrammatic notation for tensors in terms of tensor network diagrams. In these diagrams a tensor is represented by some shape and indices of the tensor are represented by lines emerging from the shape.

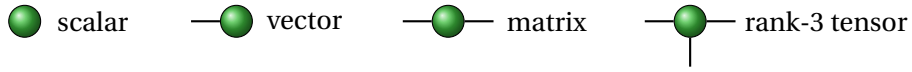

FIGURE 5.1: Diagrammatic representation of different types of tensors: a scalar with no legs, a vector with one leg, a matrix with two legs and a rank-3 tensor with three legs.

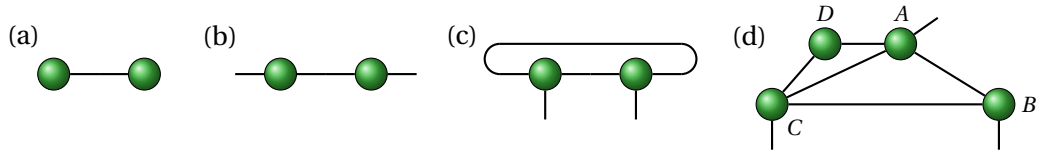

FIGURE 5.2: Tensor network diagrams for a scalar product between two vectors (a), a matrix multiplication (b), a contraction between 2 tensors with 2 open indices (c) and a contraction between 4 tensors with 3 open indices.

Lines connecting tensors between each other correspond to contracted indices while lines with a free endpoint are open indices. In Figure 5.1 one can see tensors with different number of indices (legs): a scalar, a vector, a matrix and a rank-3 tensor. In Figure 5.2 instead different contractions are shown: a scalar product between two vectors, a matrix multiplication, a contraction between two rank-3 tensors forming a matrix:

$$C_{\gamma\sigma} = \sum_{\alpha,\beta=1}^{D} A_{\alpha\gamma\beta} B_{\beta\sigma\alpha} \tag{5.2}$$

and a more strange contraction between 4 tensors forming a rank-3 tensor:

$$E_{\alpha\sigma\nu} = \sum_{\beta,\gamma,\delta,\mu,\omega=1}^{D} A_{\alpha\beta\gamma\delta} B_{\beta\sigma\mu} C_{\mu\gamma\nu\omega} D_{\delta\omega}. \tag{5.3}$$

In doing contractions there is something one has to care about. Namely, that the number of operations that has to be performed to obtain a certain result strongly depends on the order in which indices of TN are contracted. For instance in Figure 5.3, we see two different ways of applying the same overall contraction but in the first case the number of operations to be performed is $O(D^4)$ while in the second one it is $O(D^5)$. Since every TN algorithm has to deal with a lot of contraction one has to be very careful in choosing the order that minimizes the total computational cost.

With these concepts about tensors and tensor networks in mind we can now see how to write a wave function in term of MPS and what MPS really are.

Consider a lattice of L sites with d-dimensional local state spaces $\{\sigma_i\}$ on sites $i =$

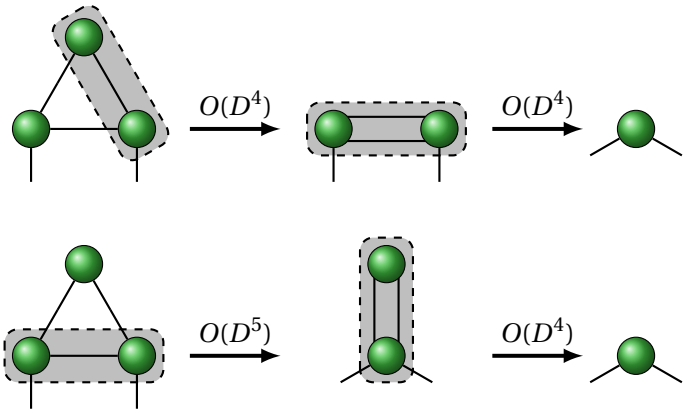

FIGURE 5.3: Contraction of 3 tensors in $O(D^4)$ computational time (top row); contraction of the same 3 tensors in $O(D^5)$ computational time (bottom row).

$1,\ldots,L$. The most general quantum state on the lattice is

$$|\psi\rangle = \sum_{\sigma_1,\ldots,\sigma_L} c_{\sigma_1\ldots\sigma_L}|\sigma_1,\ldots,\sigma_L\rangle, \tag{5.4}$$

where we have exponentially (d^L) many coefficients $c_{\sigma_1\ldots\sigma_L}$. The first step is to find a notation that gives a more local notion of the state and to do this we use Singular Value Decomposition (SVD) on the coefficients $c_{\sigma_1\ldots\sigma_L}$. If we reshape the state vector with d^L components into a matrix Ψ of dimension $(d \times d^{L-1})$ and we apply SVD on it, we obtain

$$c_{\sigma_1\ldots\sigma_L} = \Psi_{\sigma_1(\sigma_2\ldots\sigma_L)} = \sum_{a_1}^{r_1} U_{\sigma_1 a_1} S_{a_1 a_1} (V^\dagger)_{a_1(\sigma_2\ldots\sigma_L)} \equiv \sum_{a_1}^{r_1} U_{\sigma_1 a_1} c_{a_1\sigma_2\ldots\sigma_L}. \tag{5.5}$$

We now decompose the matrix U in a collection of d row vectors A^{σ_1} with entries $A^{\sigma_1}_{a_1} = U_{\sigma_1 a_1}$. At the same time we reshape $c_{a_1\sigma_2\ldots\sigma_L}$ into a matrix $\Psi_{(a_1\sigma_2)(\sigma_3\ldots\sigma_L)}$ of dimension $(r_1 d \times d^{L-2})$ and we apply again SVD on it:

$$c_{\sigma_1\ldots\sigma_L} = \sum_{a_1}^{r_1}\sum_{a_2}^{r_2} A^{\sigma_1}_{a_1} U_{(a_1\sigma_2)a_2} S_{a_2 a_2} (V^\dagger)_{a_2(\sigma_3\ldots\sigma_L)} = \sum_{a_2}^{r_2} A^{\sigma_1}_{a_1} A^{\sigma_2}_{a_1 a_2} \Psi_{(a_2\sigma_3)(\sigma_4\ldots\sigma_L)}, \tag{5.6}$$

where we have replaced U by a set of d matrices A^{σ_2} of dimension $(r_1 \times r_2)$ with entries $A^{\sigma_2}_{a_1 a_2} = U_{(a_1\sigma_2)a_2}$. Iterating this procedure to the end of the chain we obtain

$$c_{\sigma_1\ldots\sigma_L} = \sum_{a_1,\ldots,a_{L-1}} A^{\sigma_1}_{a_1} A^{\sigma_2}_{a_1 a_2} \cdots A^{\sigma_{L-1}}_{a_{L-2} a_{L-1}} A^{\sigma_L}_{a_{L-1}} \tag{5.7}$$

or more compactly, recognizing the sums over a_i as matrix multiplications,

$$c_{\sigma_1\ldots\sigma_L} = A^{\sigma_1} A^{\sigma_2} \cdots A^{\sigma_{L-1}} A^{\sigma_L}. \tag{5.8}$$

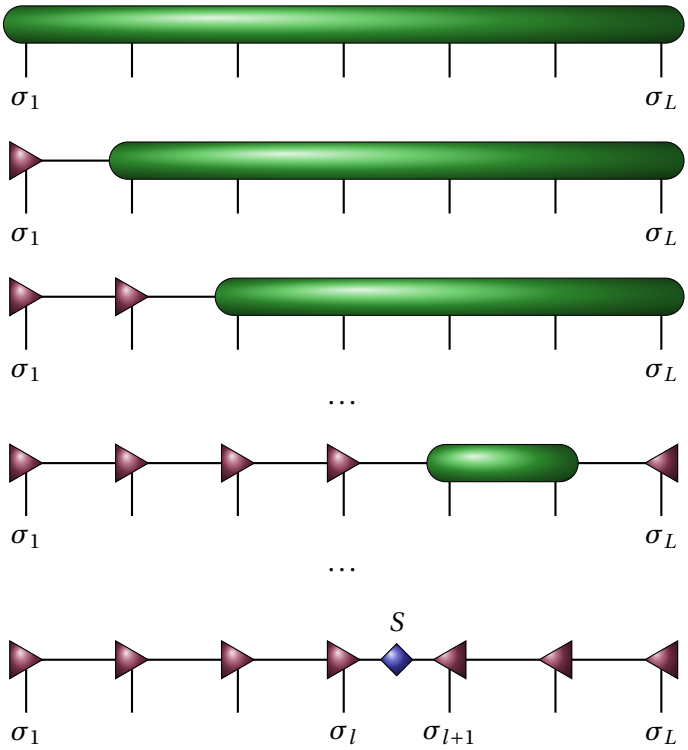

FIGURE 5.4: Graphical representation of an exact MPS obtained by a sequence of singular value decompositions starting from the left and from the right. The diamond represents the diagonal singular value matrix. Matrices to the left are left-normalized, matrices to the right are right-normalized, see Fig. 5.5.

So, the arbitrary quantum state $|\psi\rangle$ is now represented exactly in the form of a matrix product state:

$$|\psi\rangle = \sum_{\sigma_1,\ldots,\sigma_L} A^{\sigma_1} A^{\sigma_2} \cdots A^{\sigma_{L-1}} A^{\sigma_L} |\sigma_1,\ldots,\sigma_L\rangle. \tag{5.9}$$

From the properties of SVD one can easily show that matrices A satisfy the following relation

$$\sum_{\sigma_l} A^{\sigma_l \dagger} A^{\sigma_l} = \mathbb{1}. \tag{5.10}$$

Matrices that obey this condition are referred as left-normalized and matrix product states that consist only of left-normalized matrices are referred as left-canonical. One can obviously apply the same procedure starting from site L, i.e. from the right, in this case we obtain a right-canonical MPS formed by right-normalized matrices B with

$$\sum_{\sigma_l} B^{\sigma_l} B^{\sigma_l \dagger} = \mathbb{1}. \tag{5.11}$$

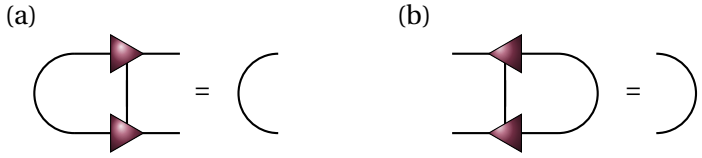

FIGURE 5.5: If two left(right)-normalized tensors are contracted over their left(right) indices, (a) and (b) respectively, an identity matrix represented by a line results.

Lastly, we can also decompose the state from the left up to site l and from the right up to site $l+1$. We therefore end up with a decomposition

$$c_{\sigma_1 \ldots \sigma_L} = A^{\sigma_1} \cdots A^{\sigma_l} S B^{\sigma_{l+1}} \cdots B^{\sigma_L}, \tag{5.12}$$

which contains the singular values on the bond $(l, l+1)$ and that will be referred as mixed canonical matrix product state.

This decomposition process can be viewed also in terms of tensor network diagrams. In Figure 5.4 the initial state vector or, to be more rigorous, the initial state rank-L tensor, is rewritten in the mixed canonical MPS representation. Tensors with triangular shape are those satisfying relations (5.10) and (5.11), graphically represented in Figure 5.5.

We have rewritten our quantum state in terms of a MPS but where are all the advantages? The effect of SVDs is to reshape our initial vector but the size of parameters remains exponentially big. Furthermore, in addition to the initial physical indices $\sigma_1, \ldots, \sigma_L$ (the vertical ones in figure 5.4), we have some new degrees of freedom responsible for gluing together our tensors and represented by contracted horizontal lines in figure 5.4. What are they?

These indices, as we will see in a moment, turn out to have an important physical meaning: they represent the structure of the many-body entanglement in the quantum state $|\psi\rangle$, and the number of different values that each one of them can take is a quantitative measure of the amount of quantum correlations in the wave function. They are usually called bond indices and the number of possible values they can take is referred as bond dimension. In order to reduce the parameters space, we can arbitrary choose a value m and force all bond dimensions to be equal (or lower) to m. Doing this we get only $O(Ldm^2)$ parameters instead of $O(d^L)$.

To better understand what we are cutting with this approximation and how entanglement relates to the bond indices, let us give an example. Imagine of having an MPS with bond dimension m for all indices such as the one in Figure 5.6. Let us now estimate the entanglement entropy of the blocks shown in the figure. For doing this we call α the

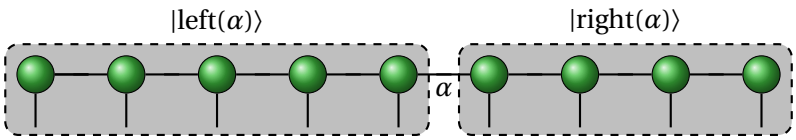

FIGURE 5.6: Partition of an MPS at bond α.

index across the boundary of the block and we write the state in terms of unnormalized kets for the left and right blocks as

$$|\psi\rangle = \sum_{\alpha=1}^{m} |\text{left}(\alpha)\rangle \otimes |\text{right}(\alpha)\rangle \tag{5.13}$$

The reduced density matrix of e.g. the left part is given by

$$\rho_{\text{left}} = \sum_{\alpha,\alpha'} X_{\alpha\alpha'} |\text{left}(\alpha)\rangle\langle\text{left}(\alpha')|, \tag{5.14}$$

where $X_{\alpha\alpha'} = \langle\text{right}(\alpha')|\text{right}(\alpha)\rangle$. This reduced density matrix clearly has a rank that is, at most, m (the same conclusions would apply if we considered the right block). Moreover, the entanglement entropy of the block, $S = -\text{tr}(\rho_{\text{left}} \log \rho_{\text{left}})$, is upper bounded by the logarithm of the rank of ρ_{left}. So, in the end, we get

$$S \leq \log m \tag{5.15}$$

which is a version of the area law for entanglement entropy since in one dimension the boundary between the two blocks has simply dimension 1. In fact, we can also interpret this equation as every broken bond index giving an entropy contribution of at most $\log m$. For more complex TN such as PEPS (Projected Entangled Pair State, a two dimensional grid of tensors) this equation is slightly modified. In that case, choosing e.g. a square block, we cut $4L$ bonds, where L is the number of tensors for each side of the square, and the entanglement entropy is upper bounded by

$$S(L) \leq 4L \log m. \tag{5.16}$$

Let us discuss the above result. First, if $m = 1$ then the upper bound says that $S(L) = 0$ no matter the size of the block. That is, no entanglement is present in the wave function. This is a generic result for any TN: if the bond dimensions are trivial, then no entanglement is present in the wave function, and the TN state is just a product state. This is the type of ansatz that is used in e.g. mean field theory. Second, for any $m > 1$ we have that the ansatz can already handle an area-law for the entanglement entropy. Changing

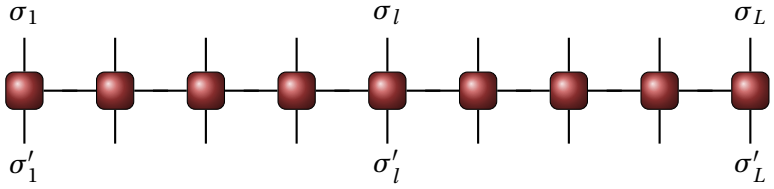

FIGURE 5.7: Graphical representation of a Matrix Product Operator.

the bond dimension m modifies only the multiplicative factor of the area-law. Therefore, in order to modify the scaling with L one should change the geometric pattern of the TN. This means that the entanglement in the TN is a consequence of both m (the size of the bond indices), and also the geometric pattern (the way these bond indices are connected). In fact, different families of TN states turn out to have very different entanglement properties, even for the same m. Third, notice that by limiting m to a fixed value greater than one we can achieve TN representations of a quantum many-body state which are both computationally efficient (as in mean field theory) and quantumly correlated (as in exact diagonalization). In a way, by using TNs one gets the best of both worlds.

The last point that remains to be clarified is how can we cut the bond indices to some fixed dimension m. Also in this case the answer is very easy and singular values decomposition gives us the recipe. The entanglement entropy is directly related to the Schmidt coefficients so one only needs to take only the m most relevant coefficients on each bond index and discard all the others.

5.3 Matrix Product Operators

If we consider a single coefficient $\langle \boldsymbol{\sigma} | \psi \rangle$ of an MPS,

$$\langle \boldsymbol{\sigma} | \psi \rangle = M^{\sigma_1} M^{\sigma_2} \cdots M^{\sigma_{L-1}} M^{\sigma_L}, \tag{5.17}$$

it is a natural generalization to try to write coefficients $\langle \boldsymbol{\sigma} | \hat{O} | \boldsymbol{\sigma}' \rangle$ of operators as

$$\langle \boldsymbol{\sigma} | \hat{O} | \boldsymbol{\sigma}' \rangle = W^{\sigma_1 \sigma'_1} W^{\sigma_2 \sigma'_2} \cdots W^{\sigma_{L-1} \sigma'_{L-1}} W^{\sigma_L \sigma'_L}, \tag{5.18}$$

where the $W^{\sigma\sigma'}$ are matrices just like the M^{σ}, with the only difference that, being representation of operators, they need both outgoing and ingoing physical states:

$$\hat{O} = \sum_{\boldsymbol{\sigma}, \boldsymbol{\sigma}'} W^{\sigma_1 \sigma'_1} W^{\sigma_2 \sigma'_2} \cdots W^{\sigma_{L-1} \sigma'_{L-1}} W^{\sigma_L \sigma'_L} | \boldsymbol{\sigma} \rangle \langle \boldsymbol{\sigma}' |. \tag{5.19}$$

Also the diagrammatic representation introduced for MPS can be easily extended for MPO. The only difference is that now, instead of a single index representing the physical state, we have two vertical indices, one down and one up, for the ingoing and outgoing physical states, see Figure 5.7.

A tensor product operator $W = W^{[1]} \otimes W^{[2]} \otimes \cdots \otimes W^{[L]}$ is already written as an MPO so expectation values of local observables and correlation functions on an MPS can be evaluated efficiently. It can result more difficult to understand how to write standard operators like Hamiltonians. Consider, for example, the Bose-Hubbard Hamiltonian

$$H = -t \sum_{l,l+1} (a_l^\dagger a_{l+1} + a_{l+1}^\dagger a_l) + \frac{U}{2} \sum_l n_l(n_l - 1). \tag{5.20}$$

We can rewrite it using MPO matrices as

$$W^{[l]} = \begin{pmatrix} \mathbb{1} & -t a_l & -t a_l^\dagger & H_l \\ 0 & 0 & 0 & a_l^\dagger \\ 0 & 0 & 0 & a_l \\ 0 & 0 & 0 & \mathbb{1} \end{pmatrix}, \tag{5.21}$$

where the single-site operator is $H_l = U n_l(n_l - 1)/2$. In this formula we interpret the entries in $W^{[l]}$ as indicating which operator in the basis $|\boldsymbol{\sigma}\rangle\langle\boldsymbol{\sigma}'|$ is assigned to what weight.

There is a convenient device for constructing MPOs based on finite state machines. The idea is essentially to consider the matrix $W^{[l]}$ as the adjacency matrix of a directed graph, where all the different paths through the graph correspond exactly to all the terms occurring in the operator formula. In Figure 5.8, the graph associated with the Bose-Hubbard Hamiltonian is shown. By tracing all the possible paths starting at 1 and of length L through the graph, all terms of Eq. (5.20) will be generated. The graph can be translated to Eq. (5.21) by inserting the symbols over the arrow connecting state i and j into the matrix-entry $W_{ij}^{[l]}$. Tracing the paths corresponds to multiplying the matrices W in the MPO formula Eq. (5.19).

Note that is quite easy to create terms with exponentially decaying weight by placing an operator on the diagonal of $W^{[l]}$ or, equivalently, adding a loop in the corresponding finite state machine. For example, inserting a loop on the node 5 with weight $\lambda\mathbb{1}$ in the graph to the right in Figure 5.8 will generate interactions terms $V_2\lambda^k n_l n_{l+k}$ for all l and $k \geq 2$.

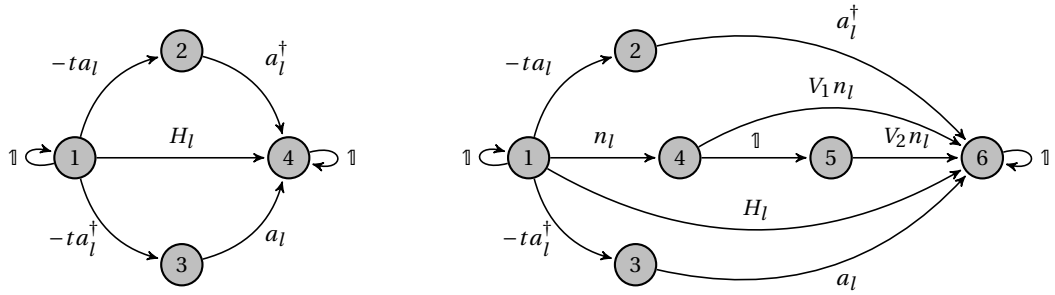

FIGURE 5.8: Finite state machine for the Hamiltonian of Eq. (5.20) (left) and for a Bose-Hubbard model with also nearest ($V_1 n_l n_{l+1}$) and next-nearest ($V_2 n_l n_{l+2}$) density-density interactions (right).

5.4 Variational algorithm

We understood how TN (MPS in case of one dimensional systems) are very good *ansätze* for approximating ground states and low-energy excitations of local Hamiltonians. However, we still need a way for finding the coefficients of the tensors. For doing so there are different ways which depend on the type of the system and on the type of the state that is targeted. Here we explain the basic idea behind the variational optimization of an MPS in order to find the ground state of a one dimensional system.

Assume $\hat{H}$ given in MPO form and consider a class of MPS with predefined matrix dimensions (simply think about a random MPS with matrices M^σ of desired shape and size, but no normalization assumed for the moment). In order to find the optimal approximation to the ground state within this class, we have to find the MPS $|\psi\rangle$ that minimizes

$$E = \frac{\langle\psi|\hat{H}|\psi\rangle}{\langle\psi|\psi\rangle} \tag{5.22}$$

In order to solve this problem, we introduce a Lagrangian multiplier λ, and extremize

$$\langle\psi|\hat{H}|\psi\rangle - \lambda\langle\psi|\psi\rangle. \tag{5.23}$$

In the end, $|\psi\rangle$ will be the desired ground state and λ the ground state energy. The problem with this approach is that the variables (the matrix elements $M^\sigma_{aa'}$) appear in the form of products, making this a highly non-linear optimization problem. But it can be done iteratively, too, and this is the idea that also drives DMRG: while keeping the matrices on all sites but one (l) constant, consider only the matrix entries $M^{\sigma_l}_{a_{l-1}a_l}$ on site l as variables. Then the variables appear in Eq. (5.23) only in quadratic form, for which the determination of the extremum is a benign linear algebra problem. This will lower the

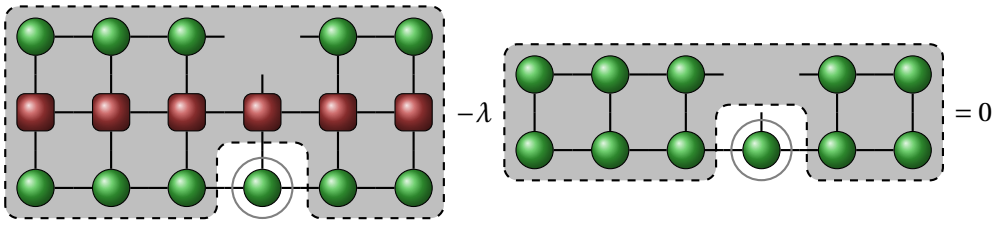

FIGURE 5.9: Generalized eigenvalue problem for the optimization of the $M^{\sigma_l}_{a_{l-1}a_l}$ vector (tensor reshaped to a vector). The unknown vector is the circled one, the left shaded region represents H_{eff} and the right one N.

energy, and find a variationally better state, but of course not the optimal one. Now one continues to vary the matrix elements on another site for finding a state again lower in energy, moving through all sites multiple times, until the energy does not improve any more.

Rewriting the variational equation (5.23) in terms of tensors of our MPS and our MPO we get the expression diagrammatically showed in Figure 5.9. At this point we reshape the unknown tensor $M^{\sigma_l}_{a_{l-1}a_l}$ to a vector v and the two shaded region in Figure 5.9 to matrices H_{eff} and N arriving to a generalized eigenvalue problem of matrix dimension $(dm^2 \times dm^2)$,

$$H_{\text{eff}} v - \lambda N v = 0. \tag{5.24}$$

Solving for the lowest eigenvalue λ_0 gives us a vector $v^0_{\sigma_l a_{l-1} a_l}$ which is reshaped back to $M^{\sigma_l}_{a_{l-1}a_l}$, λ_0 being the current ground state energy estimate. In general dm^2 is too large for an exact diagonalization, but since we are interested only in the lowest eigenvalue and eigenstate we can use eigensolvers suited for this aim like Lanczos solvers. In addition, generalized eigenvalue problems can become numerically very demanding if the condition number of N becomes bad. We can avoid this problem if we ensure that the state is left-normalized up to site $l-1$ and right normalized from site $l+1$. In this situation we can use the properties showed in Figure 5.5 and simplify N to the identity matrix.

To summarize the optimal algorithm runs as follows.

- Start from some guess state $|\psi\rangle$, right-normalized.

- *Right sweep:* Sweep through the lattice starting from site $l = 1$ to site $l-1$ and at each site solve the standard eigenproblem for M^{σ_l}. Left normalize the obtained M^{σ_l} into A^{σ_l} by SVD. The remaining matrices of the SVD are multiplied to the right

into $M^{\sigma_{l+1}}$ which will be the starting guess for the eigensolver in the next site. Move on by one site and repeat.

- *Left sweep:* Sweep through the lattice starting from site $l = L$ to site 2 and at each site solve the standard eigenproblem for M^{σ_l}. Right normalize the obtained M^{σ_l} into B^{σ_l} by SVD. The remaining matrices of the SVD are multiplied to the left into $M^{\sigma_{l-1}}$ which will be the starting guess for the eigensolver in the next site. Move on by one site and repeat.

- Repeat right and left sweeps until convergence is reached.

This variational MPS algorithm is quite prone to getting stuck, thus not giving the correct ground state. Once we arrive in a well-defined symmetry sector then each one of the states will have a good quantum number and their distribution can not change any more. This means that if it does not correspond to the distribution that the variationally optimal state would yield, it can never reach that state.

To overcome this limitation one can use a two-site optimization. In this case the optimization will be done on two nearest sites contracted, i.e. a matrix of dimension $(d^2m^2 \times d^2m^2)$, and the resulting reshaped tensor will have to be split again in two tensors via SVD with the notice of truncating the just created bond link to dimension m.

5.5 Time evolution algorithms

In this section we analyse two different methods for obtaining the time evolution of a quantum state described by an MPS. The first one is the conventional Time Evolving Block Decimation (TEBD) method based on a Lie-Trotter-Suzuki decomposition of the evolution operator. The second is the Dirack-Frenkel Time Dependent Variational Principle (TDVP) based on a splitting of the projector onto the matrix product state tangent space [87, 88].

5.5.1 Time Evolving Block Decimation method

If one has an Hamiltonian H consisting only of nearest-neighbour interactions, i.e. $H = \sum_i h_i$, where h_i contains only the terms relative to sites i and $i+1$, a first-order Trotter decomposition of the relative evolution operator is

$$e^{-iH\tau} = e^{-ih_1\tau} + e^{-ih_2\tau} + \ldots + e^{-ih_{L-2}\tau} + e^{-ih_{L-1}\tau} + o(\tau^2). \tag{5.25}$$

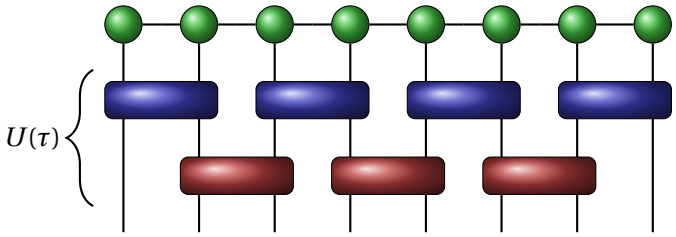

FIGURE 5.10: Time evolution of an MPS by a time step τ. Blue tensors are gates corresponding to the exponentiation of Hamiltonians for odd links, red ones are those corresponding to the exponentiation of Hamiltonians for even links.

It contains an error because the link Hamiltonians do not commute, $[h_i, h_{i+1}] \neq 0$. In order to have commuting terms one can split H in even (h_i^E, $i = 2,4,...$) and odd (h_i^O, $i = 1,3,...$) operators acting respectively on even and odd links and then apply all the odd gates first and the even ones after as shown in Figure 5.10. The big problem of this method is that finding a way of splitting the Hamiltonian in commuting pieces becomes more and more difficult for non nearest-neighbour Hamiltonians. A simple improvement on the algorithm given above is to do a second-order Trotter decomposition

$$e^{-iH\tau} = e^{-iH_{\text{odd}}\tau/2} + e^{-iH_{\text{even}}\tau} + e^{-iH_{\text{odd}}\tau/2} + o(\tau^3) \tag{5.26}$$

and this is what is used in the next.

The resulting algorithm consists of the following steps (assuming an initial MPS right-normalized):

1. Contract h_1^O on first link

2. Do a (truncated) SVD-decomposition for getting back two tensors, left-normalize the two tensors and put the remainder in the next link

3. Repeat steps 1 and 2 for remaining odd links

4. Contract h_{L-2}^E (or h_{L-1}^E if L is odd) on right end of the chain

5. Do a (truncated) SVD-decomposition for getting back two tensors, right-normalize the two tensors and put the remainder in the next link

6. Repeat steps 3 and 4 for remaining even links

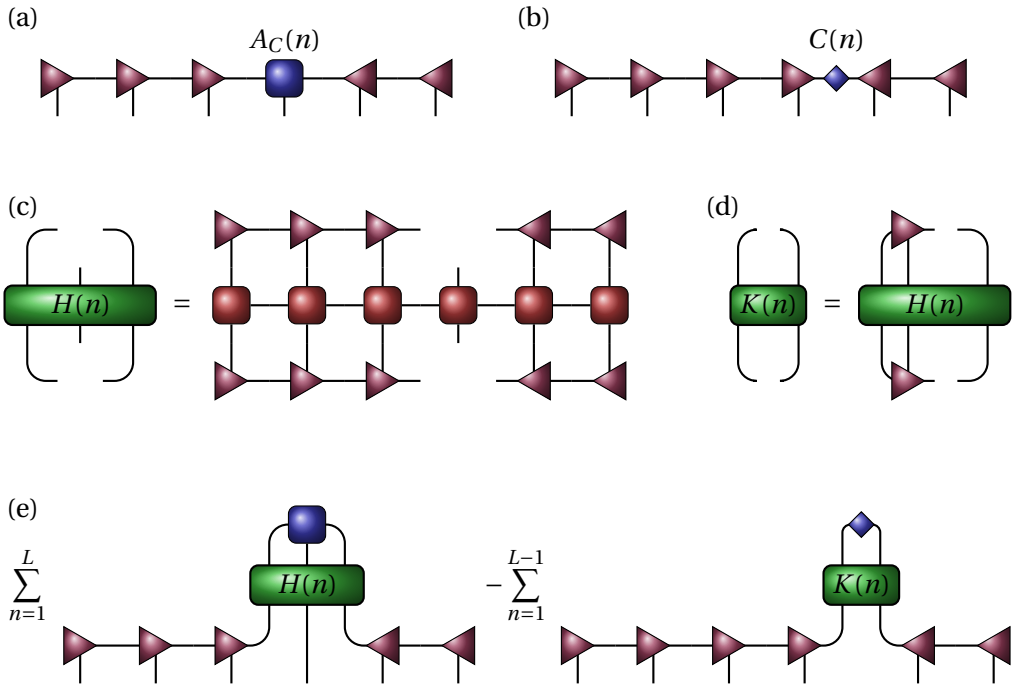

FIGURE 5.11: An MPS can be brought into a mixed-canonical form with a one-site center, $A_C(n)$, at site n (a) or even a zero-site center, $C(n)$, whose singular values correspond to the Schmidt coefficients of the state (b). One-site effective Hamiltonian $H(n)$ (c). Similarly, one can define a zero-site effective Hamiltonian $K(n)$ (d) which can easily be computed from $H(n)$. Right-hand side (up to the factor −i) of the TDVP equation, Eq. (5.27) (e).

5.5.2 Time Dependent Variational Principle method

The TDVP method corresponds to an orthogonal projection of the evolution vector of the Schrödinger equation ($-\mathrm{i}H|\Psi\rangle$) onto the tangent space of the MPS manifold at the current state:

$$\frac{\mathrm{d}|\Psi(M)\rangle}{\mathrm{d}t} = -\mathrm{i}PH|\Psi(M)\rangle \tag{5.27}$$

In this way the state is always in the MPS manifold and can be described by a set of time evolving parameters corresponding to the tensors of the MPS (M matrices).

The tangent space projector applied to $H|\Psi\rangle$ results in the diagrammatic expression of Figure 5.11 (e) where $H(n)$ and $K(n)$ are defined in Figure 5.11 (c)-(d) (for the explicit calculation of the projector see Supplemental Material of [88]). Taking the MPS in the form of Figure 5.11 (a) or Figure 5.11 (b) alternatively, we have the time-dependent parameters in tensors A and C and these tensors are the only ones that matter in the time derivative of the state. Equation (5.27) can be then exactly integrated for every single

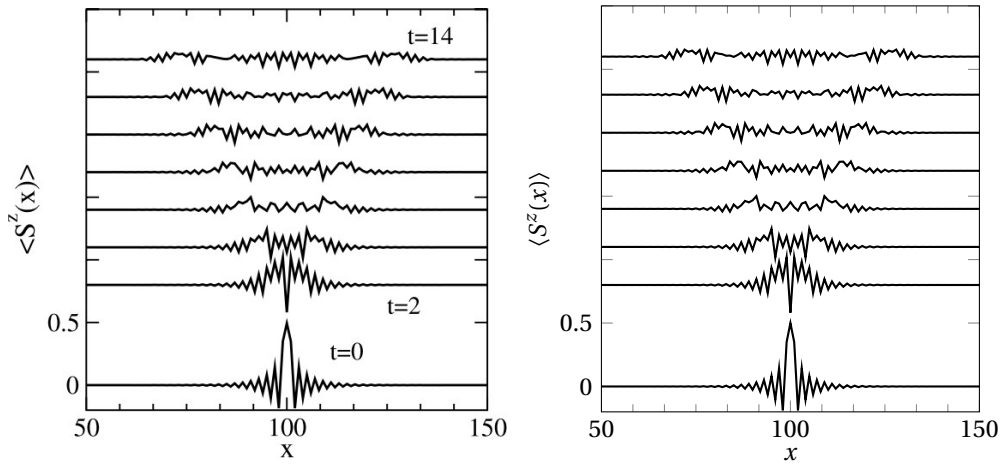

FIGURE 5.12: Spin-1 Heisenberg chain: time evolution of the local magnetization after a local quench at the center of the chain. Comparison between results of [91] (left box) and those obtained by a TDVP-TS evolution (right box). Left box is a figure taken from [91].

term of the sum with solutions:

$$A_n(t) = \exp\left[-\mathrm{i}H(n)\,t\right] A_n(0) \tag{5.28}$$

$$C_n(t) = \exp\left[+\mathrm{i}K(n)\,t\right] C_n(0) \tag{5.29}$$

Since we have a differential equation consisting in a sum of integrable parts it is natural to use a Lie-Trotter splitting approach and to evolve every single integrable part for a small step τ. In addition, the normal DMRG sweep already defines a natural order in doing so. Another simplification is the existence of Lanzcos routines [89, 90] for computing matrix exponential acting on a vector without the need of explicitly calculating the exponential.

The resulting algorithm for single-site integration consists of the following steps (assuming an initial MPS right-normalized):

1. Evolve $A(n,t)$ according to Eq. (5.28) obtaining $A(n,t+\tau)$
2. Do a QR-decomposition of $A(n,t+\tau)$ into a left normalized tensor and a remainder $C(n,t+\tau)$
3. Evolve $C(n,t+\tau)$ backwards according to Eq. (5.29) obtaining the new $C(n,t)$
4. Absorb $C(n,t)$ into the next site to create the new $A(n+1,t)$
5. Repeat steps 1-4 for all sites.

This algorithm can also be extended to a 2-sites version in which Eqs. (5.28)-(5.29) are replaced by

$$A_{n:n+1}(t) = \exp\left[-\mathrm{i}H(n:n+1)\,t\right] A_{n:n+1}(0) \tag{5.30}$$

$$A_n(t) = \exp\left[+\mathrm{i}H(n)\,t\right] A_n(0) \tag{5.31}$$

where Eq. (5.31) is the backwards analogous of Eq. (5.28), $A_{n:n+1}$ is the tensor resulting by the contraction of two neighbours sites and $H(n:n+1)$ is the 2-sites version of Fig. 5.11 (c). In this case on step 2 one has to perform a truncated SVD-decomposition to cut the bond dimension at the desired value. For a more specific description of the steps see Supplementary Material of [88].

5.5.3 Test: local quench

In order to check the validity of this relatively new method and to compare it with the more acknowledged TEBD, we repeat some results well known in literature analysing the correctness and timing performances of TDVP.

As a first test we consider the time evolution of the on-site magnetization for an excited state of a spin-1 Heisenberg chain [91]. In order to study the dynamics of this excitation, we first run the variational algorithm for obtaining the ground state of a chain of 200 sites. Then we perform a preliminary sweep to apply $\hat{S}^+$ to a single site located at the center of the chain thus getting the initial state as a localized wave packet consisting of all wave vectors. Finally we let this initial state evolve in time under the action of the Heisenberg Hamiltonian, and we measure the local magnetization $S_z(j)$ for each site j at every time step. The initial wave packet spreads out as time progresses; different components move with different speeds, given by the corresponding group velocity.

In Figure 5.12 we compare the results taken from [91] with those obtained with a two sites TDVP evolution. As one can see the plots are very similar. The differences with respect to the single site TDVP evolution have also been checked. The latter is much faster (see next section for a detailed time analysis) and, for this particular case, the lost in precision is not so pronounced as one can see in Figure 5.13. This figure shows the differences in local magnetization at different times for the two site (TS) and single site (SS) TDVP evolution. These differences grow with time but also for the longest time reached in the simulation they remain around 0.5% of the maximum magnetization value.

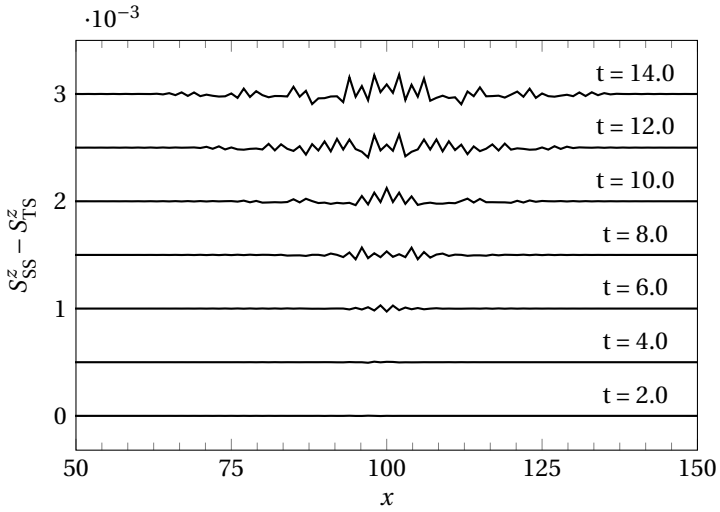

FIGURE 5.13: Spin-1 Heisenberg chain: comparison between single site (SS) and two sites (TS) TDVP evolution.

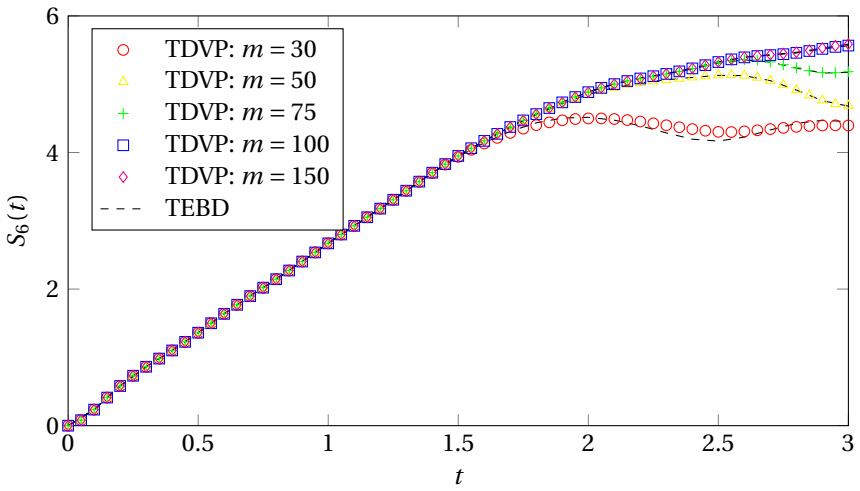

FIGURE 5.14: XX(Z) chain, global quench: comparison between TEBD and two sites TDVP algorithms.

5.5.4 Test: global quench

As a second test we consider the evolution of the block entanglement entropy in a linear XXZ chain. The state of the system at time $t = 0$ is the anti-ferromagnetic one. We let this initial state evolve with the Hamiltonian of the XX model thus changing from an initial product state to an entangled one. This entanglement can be measured by the

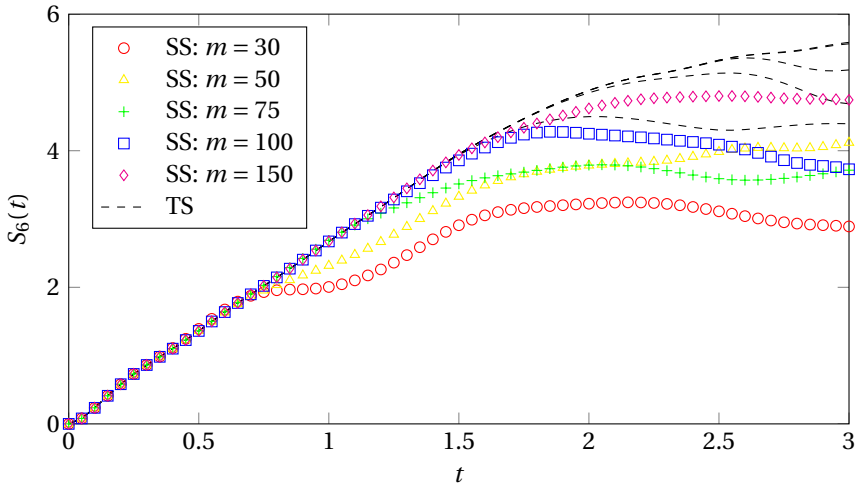

FIGURE 5.15: XX(Z) chain, global quench: comparison between single site and two sites TDVP evolution.

von Neumann entropy of the reduced density matrix of the block $\rho(t)$:

$$S(t) = -\mathrm{Tr}\left[\rho(t)\log_2\rho(t)\right] \tag{5.32}$$

This has been done for different values of the bond dimension m ranging from 30 to 200. Clearly, as the state evolves towards an entangled one, the entanglement present in the system grows and one needs more states to correctly describe it. An estimate of the number of states needed for an accurate description is given by $\propto 2^{S(t)}$ so when the block entropy reaches a (m-dependent) critical value it diverges from the theoretical curve. To maintain consistency with Ref. [92] we analyse $S(t)$ for a block of length 6 in a chain of 50 sites and with a time step $dt = 5 \times 10^{-2}$.

For this system we test the two sites TDVP algorithm not only against the literature result [92] but also against the TEBD algorithm. This comparison can be viewed in Figure 5.14. As one can see the block entropies obtained with the two different algorithms are in very good agreement between each other and also with respect to results of [92]. The single site TDVP instead diverges from the ideal curve much before (see Figure 5.15) making it not suitable for simulate systems of this type.

5.5.5 Strictly Single-Site TDVP Algorithm with Subspace Expansion

Single site TDVP is much faster than two sites TDVP but, as shown in the previous sections, it gives less accurate or, in some cases, even wrong results. We can try to improve

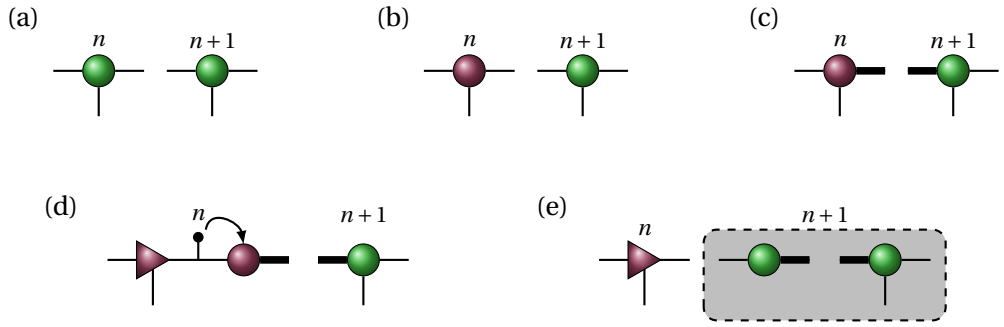

FIGURE 5.16: Steps of enhanced single site TDVP evolution for site n. Green tensors are at time t, purple ones at time $t+\delta t$. (a): initial MPS tensors. (b): evolution forward in time of tensor n. (c): enlargement of both tensors. (d): SVD decomposition, truncation and absorption of singular values into remainder tensor. (e): evolution back in time of remainder and contraction with tensor $n+1$ to obtain the next tensor.

the single-site algorithm implementing a method called "Strictly Single Site with Subspace Expansion" [93]. This method is designed for the variational algorithm and is based on an enlargement of the MPS tensors and a subsequent singular value decomposition during the minimization sweep (for more details see Ref. [93]). The steps we followed in adapting this method to the TDVP one are synthesized in Figure 5.16. The only thing that changes with respect to the normal single site TDVP algorithm is the tensor enlargement (see Ref. [93] for the explicit expression of the enlarged term) after the time evolution of the site tensor (step (c) in Fig. 5.16).

In Figure 5.17 the results of this algorithm compared with the "exact" two sites TDVP are shown. As one can see they are in very good agreement between each other. In the next section we will also analyse the differences in execution time for the different time evolution algorithms treated in this Section.

5.5.6 Timing

So far we have introduced two different algorithms for the time evolution of an MPS: Time Evolving Block Decimation method and Time Dependent Variational Principle method. For this second algorithm we have also introduced three different variants: Single Site, Two Sites and Single Site with subspace expansion. Now we want to analyse them from the point of view of the performances.

For doing so we ran 20 repetitions of each couple (m, alg) with equal initial conditions and where $m = 30, 50, 75, 100, 150, 200$ and alg = TDVP TS, TDVP SS, TDVP SSenh, TEBD.

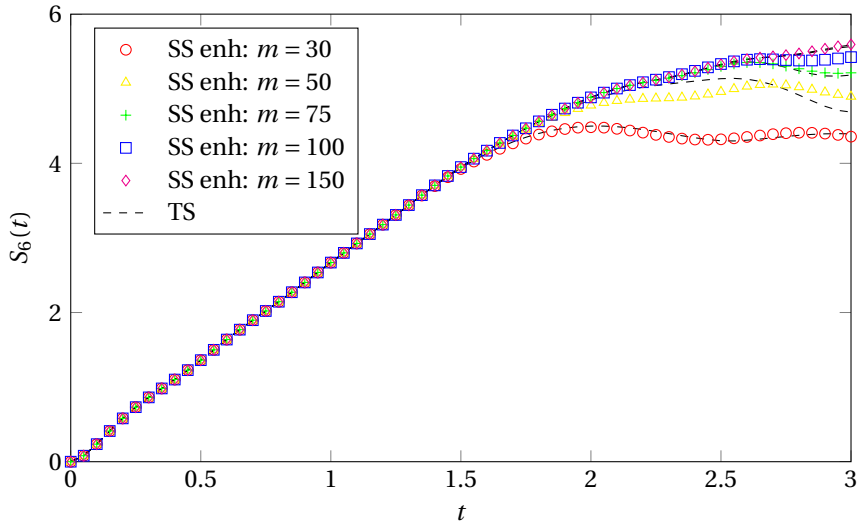

FIGURE 5.17: XX(Z) chain, comparison between "exact" two sites TDVP and single site TDVP with subspace expansion.

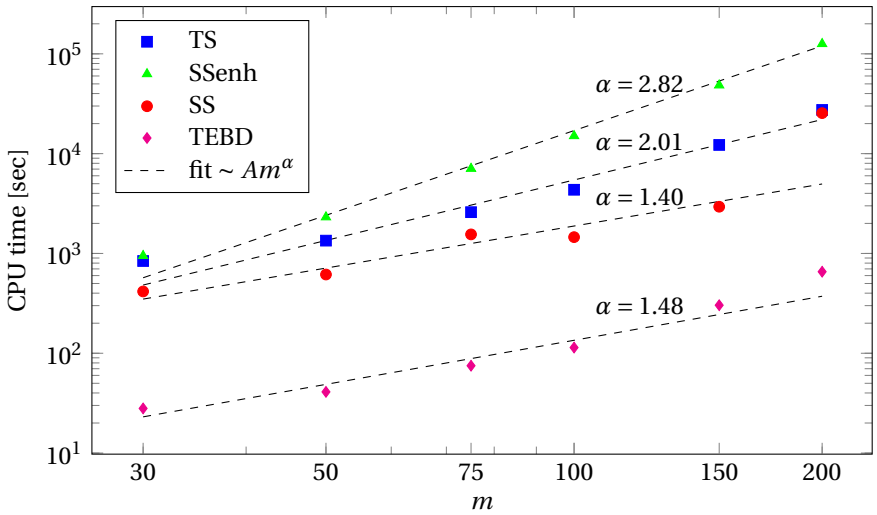

FIGURE 5.18: XX(Z) chain: execution time for different algorithms as a function of m. Dashed lines are fitted curves $\sim Am^{\alpha}$ with fitting parameter α indicated.

The averaged CPU times obtained are reported in Figure 5.18.

As one can see, TEBD is the fastest, at least one order of magnitude faster than the others. The slowest seems to be the single site TDVP with subspace expansion and this can be surprising at first since its creators claim that, for what regards the minimization, it is about 4 times faster than two sites version [93]. An explanation can be that in the

minimization procedure with subspace expansion the tensor that is minimized has always dimension $m^2 d$ as in the normal single site algorithm. Here instead we evolve in time a $m^2 d$ tensor and a $m^2(s+1)$ one (with s the MPO dimension) opposed to the single site TDVP case where tensors have dimensions $m^2 d$ and m^2.

Another thing that has to be considered is that all algorithms have been only checked for what regards the correctness of results but they have not been optimized with respect to performances.

Conclusion

In this Thesis I have presented our study on dynamical properties of mixtures of ultracold Bose gases. We analysed the behaviour of this system in different regimes: with and without coherent coupling between the two components, in homogeneous and harmonic shaped trapping potentials and in different dimensions and geometries. Most of the results presented here have been obtained by means of numerical solutions of coupled Gross-Pitaevskii equations and have been compared with theoretical predictions (and sometimes experiments), describing the same phenomena.

In Chapter 2 the stability of persistent currents in a two-component Bose-Einstein condensate in a toroidal trap is studied in both the miscible and the immiscible regime. In the miscible regime we show that superflow decay is related to linear instabilities of the spin-density Bogoliubov mode. We find a region of partial stability, where the flow is stable in the majority component while it decays in the minority component. We also characterize the dynamical instability appearing for a large relative velocity between the two components. In the immiscible regime the stability criterion is modified and depends on the specific density distribution of the two components. The effect of a coherent coupling between the two components is also discussed.

In Chapter 3 I have presented our study on the collective modes of the minority component of a highly unbalanced Bose-Bose mixture. In the immiscible case we find that the ground state can be a two-domain walls soliton. Although the mode frequencies are continuous at the transition, their behaviour is very different with respect to the miscible case. The dynamical behaviour of the solitonic structure and the frequency dependence

on the inter- and intra-species interaction is numerically studied using coupled Gross-Pitaevskii equations.

In this chapter we also showed the results of the study on the static and the dynamic response of coherently coupled two component Bose-Einstein condensates due to a spin-dipole perturbation. The static dipole susceptibility is determined and is shown to be a key quantity to identify the second order ferromagnetic transition occurring at large inter-species interactions. The dynamics, which is obtained by quenching the spin-dipole perturbation, is very much affected by the system being paramagnetic or ferromagnetic and by the correlation between the motional and the internal degrees of freedom. In the paramagnetic phase the gas exhibits well defined out-of-phase dipole oscillations, whose frequency can be related to the susceptibility of the system using a sum rule approach. In particular in the interaction $SU(2)$ symmetric case, when all the two-body interactions are the same, the external dipole oscillation coincides with the internal Rabi flipping frequency. In the ferromagnetic case, where linear response theory isnot applicable, the system shows highly non-linear dynamics. In particular we observe phenomena related to ground state selection: the gas, initially trapped in a domain wall configuration, reaches a final state corresponding to the magnetic ground state plus small density ripples. Interestingly, the time during which the gas is unable to escape from its initial configuration is found to be proportional to the square root of the wall surface tension.

Finally, in Chaper 5, I have introduced the Tensor Network method, a numerical method that allows to correctly take into account quantum correlation. This method is also very useful for extending the results obtained in this Thesis.

APPENDIX

A Thomas-Fermi approximation and speed of sound correction

The Gross-Pitaevskii equation

$$i\hbar\frac{\partial}{\partial t}\psi(\mathbf{r},t)=\left(-\frac{\hbar^2\nabla^2}{2m}+V_{\text{ext}}(\mathbf{r})+g|\psi(\mathbf{r},t)|^2\right)\psi(\mathbf{r},t) \tag{A.1}$$

should be solved numerically except in some important limits, one of this is the Thomas-Fermi limit. If we are in the presence of a repulsive interaction ($g>0$) the gas will expand and the size of the cloud will increase. Eventually, if the effect of the interaction is very significant, the width of the gas will become so large and the density profile so smooth that we can ignore the kinetic energy term in the Gross-Pitaevskii equation. This limit is called the Thomas-Fermi limit and it is characterized by the following analytical solution for the order parameter

$$\Psi_{\text{TF}}(\mathbf{r})=\sqrt{n_{\text{TF}}(\mathbf{r})}=\sqrt{\frac{1}{g}\left[\mu_{\text{TF}}-V_{\text{ext}}(\mathbf{r})\right]}. \tag{A.2}$$

The chemical potential μ_{TF} is obtained by imposing the normalization of n_{TF} to the number of particles, $\int d\mathbf{r}|\psi(\mathbf{r})|^2=N$, and it takes the value

$$\mu_{\text{TF}}=\frac{\hbar\omega_{\text{ho}}}{2}\left(\frac{15Na}{a_{\text{ho}}}\right)^{2/5} \tag{A.3}$$

where $a_{\text{ho}}=\sqrt{\hbar/(m\omega_{\text{ho}})}$ is the oscillator length associated with the geometrical average of the three trapping frequencies, ω_{ho}.

We now introduce a crucial quantity for the theory that characterizes the interacting nature of the system, namely the healing length

$$\xi = \sqrt{\frac{\hbar^2}{2mgn}}. \tag{A.4}$$

It is the shortest distance over which the wave function can change and is obtained equating the kinetic term to the energy scale of the system given by the chemical potential. Typically ξ is much smaller than the dimension of the system and smoothing of the wave function only occurs in a thin boundary layer so these surface effects give only small corrections to results calculated using the Thomas-Fermi approximation.

The condition of validity for the Thomas-Fermi approximation can be investigated rescaling the Gross-Pitaevskii equation (A.1) with spherical harmonic trapping of frequency $\omega_{\rm ho}$ and using $a_{\rm ho}$ and $\hbar\omega_{\rm ho}$ as units of length and energy:

$$\left[-\tilde{\nabla}^2 + \tilde{r}^2 + 8\pi\left(\frac{Na}{a_{\rm ho}}\right)\tilde{\Psi}^2(\tilde{\mathbf{r}})\right]\tilde{\Psi}(\tilde{\mathbf{r}}) = 2\tilde{\mu}\tilde{\Psi}(\tilde{\mathbf{r}}) \tag{A.5}$$

where $\tilde{\Psi} = N^{-1/2}a_{\rm ho}^{-3/2}\Psi_0$. So, in order to ignore the kinetic term we must have that the so called Thomas-Fermi parameter $Na/a_{\rm ho}$ is much higher than 1.

The density profile takes the form of an inverted parabola which vanishes at the classical turning point where $V_{\rm ext}(R_k) = \mu_{\rm TF}$, $k = x, y, z$. In case of an isotropic trapping these radii reduce to a single value

$$R_{\rm TF} = a_{\rm ho}\left(\frac{15Na}{a_{\rm ho}}\right)^{1/5} \tag{A.6}$$

and, if we evaluate the healing length at the centre of the trap where $n_{\rm TF}(0) = \mu/g$, we obtain for the ratio of ξ and R as

$$\frac{\xi}{R} = \left(\frac{15Na}{a_{\rm ho}}\right)^{-2/5} \tag{A.7}$$

showing that, as previously said, in the Thomas-Fermi limit the healing length becomes much smaller than the size of the condensate.

A.1 Thomas-Fermi approximation for 2-component BEC in a ring trap

To apply Thomas-Fermi approximation to our condensate in a ring geometry it is convenient to assume a displaced harmonic trap as confining potential (this has been done

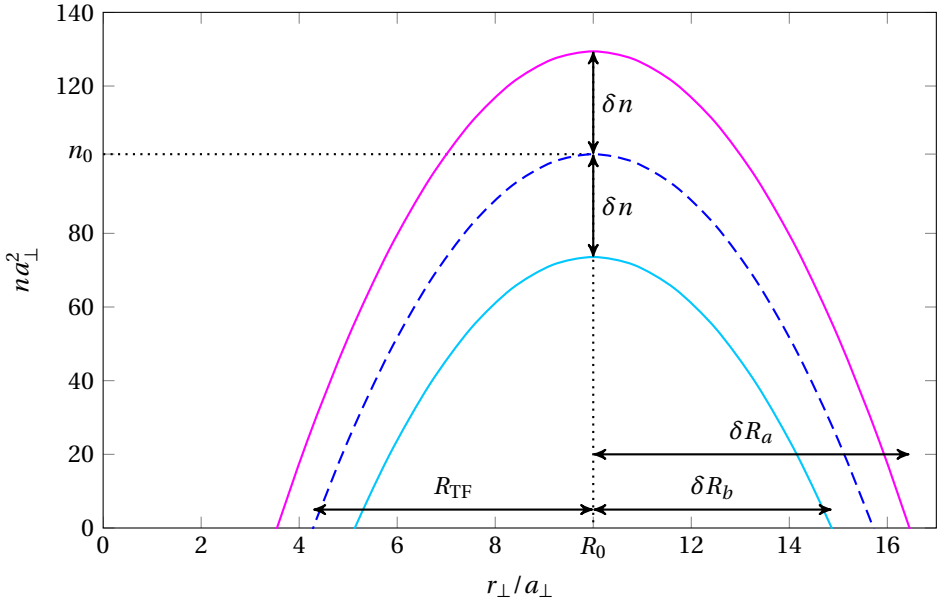

FIGURE A.1: Thomas-Fermi density profiles for a two-component mixture in a ring shaped harmonic trap. Dashed line corresponds to the balanced mixture, $N_a = N_b$, solid lines to the unbalanced one with polarization $P_z = (N_a - N_b)/N = 0.4$.

for example in [52]),

$$V(r_\perp) = \frac{1}{2} m\omega_\perp^2 (r_\perp - R_0)^2, \tag{A.8}$$

where m is the atomic mass, $\omega_\perp$ is the trapping frequency, $r_\perp^2 = x^2 + y^2$ is the radial coordinate and R_0 is the position of the potential minimum. Without any loss of generality we are considering here a two dimensional system as we have done in [22].

Neglecting the quantum pressure term in GP equations and assuming equal intra-species scattering lengths ($g_a = g_b \equiv g$), the densities for components $\sigma = a, b$ are given by

$$n_\sigma = n_0 \left[1 - \left(\frac{r_\perp - R_0}{R_{\rm TF}}\right)^2\right] \pm \delta n, \tag{A.9}$$

with $\pm$ corresponding respectively to a and b. In the last expression we used the central density n_0, the Thomas-Fermi radius $R_{\rm TF}$ and the half density difference δn given respectively by

$$n_0 = \frac{1}{2}\frac{\mu_a + \mu_b}{g + g_{ab}}, \tag{A.10}$$

$$R_{\rm TF}^2 = \frac{\mu_a + \mu_b}{m\omega_\perp^2}, \tag{A.11}$$

$$\delta n = \frac{1}{2}\frac{\mu_a - \mu_b}{g - g_{ab}}. \tag{A.12}$$

The quantity R_{TF} corresponds to the Thomas-Fermi radius of the total density. Since the components can be differently populated, the radial extent of the corresponding clouds can also be different. This allows us to define inner (+) and outer (−) radii for the two components as

$$R_{\pm}^{a} = R_0 \pm \delta R_a = R_0 \pm R_{\mathrm{TF}}\sqrt{1 + \frac{\delta n}{n_0}}, \tag{A.13}$$

$$R_{\pm}^{b} = R_0 \pm \delta R_b = R_0 \pm R_{\mathrm{TF}}\sqrt{1 - \frac{\delta n}{n_0}}. \tag{A.14}$$

Normalization of the densities to N_a and N_b gives the chemical potentials

$$\mu_a = \frac{\mu_0}{g + g_{ab}}\left[g\left(\frac{2N_a}{N}\right)^{2/3} + g_{ab}\left(\frac{2N_b}{N}\right)^{2/3}\right], \tag{A.15}$$

$$\mu_a = \frac{\mu_0}{g + g_{ab}}\left[g\left(\frac{2N_b}{N}\right)^{2/3} + g_{ab}\left(\frac{2N_a}{N}\right)^{2/3}\right], \tag{A.16}$$

where μ_0 is given by

$$\mu_0 = \frac{1}{2}\hbar\omega_\perp\left(\frac{3}{16\pi}\frac{g + g_{ab}}{\hbar\omega_\perp a_\perp^2}\frac{a_\perp}{R_0}N\right)^{2/3} \tag{A.17}$$

and corresponds to the chemical potential of the symmetric mixture ($N_a = N_b$). An example of what these density profiles look like is given in Figure A.1, where the relevant parameters are indicated. We can also rewrite the chemical potentials as functions of the total number of particles $N = N_a + N_b$ and of the polarization $P_z = (N_a - N_b)/N$

$$\mu_a = \frac{\mu_0}{g + g_{ab}}\left[g\,(1 + P_z)^{2/3} + g_{ab}\,(1 - P_z)^{2/3}\right], \tag{A.18}$$

$$\mu_a = \frac{\mu_0}{g + g_{ab}}\left[g\,(1 - P_z)^{2/3} + g_{ab}\,(1 + P_z)^{2/3}\right]. \tag{A.19}$$

A.2 Speed of sound correction in a ring trap

The spin speed of sound expression used to delimit the region in which currents are stable in chapter 2.3 is calculated taking into account a one dimensional system. Here we calculate the correction to this value given by the presence of a transverse (radial) degree of freedom.

For a single component condensate in a 3D harmonic trap the renormalizing factor ranges from unity in the noninteracting limit to $1/\sqrt{2}$ in the Thomas-Fermi one [94, 95,

96, 97]. This correction depends on the geometry and on the density structure, not in the nature of the mode (spin or density) or in the number of components (provided that the mixture is in the miscible phase).

In order to simplify our problem we observe two things. First, a ring trap with circumference, $2\pi R_0$, much larger than the radial width can be thought of as a very long prolate trap with periodic boundary conditions. Second, the densities of the two components in the Thomas-Fermi limit take the same inverted parabola structure as for one component (see Section A.1). Therefore, without any loss of generality, we can calculate the Thomas-Fermi correction factor to the speed of sound for a single component condensate confined in a 2D prolate trap and apply it to the two-component ring-confined case.

To derive the correction factor to the speed of sound we start from the hydrodynamic equations for the density and the velocity in a 2D system,

$$\frac{\partial n}{\partial t} + \nabla_\perp(\mathbf{v}n) = 0, \tag{A.20}$$

$$m\frac{\partial \mathbf{v}}{\partial t} + \nabla_\perp\left[V_{\mathbf{ext}} + gn + -\frac{\hbar^2}{2m\sqrt{n}}\nabla_\perp^2\sqrt{n} + \frac{1}{2}mv^2\right] = 0, \tag{A.21}$$

where $V_{\text{ext}} = \frac{1}{2}m\omega_x^2x^2 + \frac{1}{2}m\omega_y^2y^2$. We want to analyse the situation where $\omega_x \gg \omega_y$, which is the relevant one for the toroidal trap where the y coordinate corresponds to the azimuthal angle around the trap axis. Neglecting the quantum pressure term ($\sim \nabla_\perp^2\sqrt{n}$), the ground state at rest is characterized by an inverted parabola profile with Thomas-Fermi radii given by $R_x = \sqrt{\frac{2\mu}{m\omega_x^2}}$ and $R_y = \sqrt{\frac{2\mu}{m\omega_y^2}}$. The system forms an ellipse on the xy-plane with minor and major axis given by R_x and R_y respectively. The chemical potential is given by $\mu = \hbar\omega_y\sqrt{N\tilde{g}/(\pi\lambda_\perp)}$, where $\tilde{g} = g/(\hbar\omega_y a_y^2)$, with g the 2D coupling constant, $a_y = \sqrt{\hbar/(m\omega_y)}$ and where we have introduced the ratio of trapping frequencies $\lambda_\perp = \omega_y/\omega_x$.

By linearising the hydrodynamic equations and combining them, one finds the eigenvalue equation

$$\omega^2\delta n = -\partial_x\left[\frac{\mu - V_{\text{ext}}}{m}\partial_x\delta n\right] - \partial_y\left[\frac{\mu - V_{\text{ext}}}{m}\partial_y\delta n\right], \tag{A.22}$$

where $\delta n = n - n_0$ and n_0 is the unperturbed density. Notice that we have assumed a temporal dependence of the density perturbations $\delta n \sim e^{i\omega t/\hbar}$ and analogously for the velocity perturbation. We are interested in finding the lowest energy excitations which, consistently with our assumption $\omega_x \gg \omega_y$, will mainly come from the y-dependent part of the eigenvalue equation above. Neglecting thus all dependence of δn on x, that is

taking $\delta n \equiv \delta n_0(y)$, and integrating the whole equation with respect to x, we find

$$\omega \delta n_0 = -\frac{1}{3}\omega_y^2 \left(R_y^2 - y^2\right) \partial_y^2 \delta n_0 + 2\omega_y^2 y \partial_y \delta n_0. \tag{A.23}$$

For the excitations localized at the center of the trap ($y \simeq 0$) this yelds

$$\omega^2 = \frac{1}{3}\omega_y^2 R_y^2 k^2 = \frac{2}{3}\frac{\mu}{m}k^2. \tag{A.24}$$

Using the well-known result $c_0 = \sqrt{\mu/m}$ for the speed of sound of a uniform condensate we recover the dispersion relation $\omega = ck$ with

$$c = \sqrt{\frac{2}{3}}c_0. \tag{A.25}$$

The correction factor due to radial confinement is thus $\sqrt{2/3}$. The main deviation from this factor would come from a density profile that was not close enough to the Thomas-Fermi limit.

Acknowledgements

Arrived to the end of this work I think it is worth to acknowledge the important role of those who guided, helped and supported me during this three-year-long PhD program.

Let me start by thanking those who, by sharing with me their expertise, made it possible to realize this work. I thank my supervisor Alessio Recati. He constantly encouraged me, from my first steps into the world of cold gases to the defense of this Thesis. I also thank Matteo Rizzi for his patience and his clarity in explaining me DMRG.

I wish to thank all the members of the BEC Center in Trento who assured a stimulating and enjoyable environment for the advancement of my PhD and all the members of the Komet337 group of the Johannes Gutenberg Universität Mainz for their kind hospitality.

Before concluding, some words also in Italian.

Ringrazio di cuore i miei genitori e mia sorella che sono rimasti al mio fianco lungo qualunque mio cammino, professionale e personale. Un grazie anche ad Alice, inestimabile fonte di conforto, distrazione e risate.

Infine ringrazio Alessio, Marco e Simone con i quali ho condiviso i successi e le problematiche di questo mio percorso.

Bibliography

[1] J. SMYRNAKIS, S. BARGI, G. M. KAVOULAKIS, M. MAGIROPOULOS, K. KÄRKKÄINEN, and S. M. REIMANN. Mixtures of Bose Gases Confined in a Ring Potential. *Physical Review Letters*, **103**:10 (Sept. 2009), p. 100404.

[2] T. SHIMODAIRA, T. KISHIMOTO, and H. SAITO. Connection between rotation and miscibility in a two-component Bose-Einstein condensate. *Physical Review A*, **82**:1 (July 2010), p. 013647.

[3] K. ANOSHKIN, Z. WU, and E. ZAREMBA. Persistent currents in a bosonic mixture in the ring geometry. *Physical Review A*, **88**:1 (July 2013), p. 013609.

[4] S. BEATTIE, S. MOULDER, R. J. FLETCHER, and Z. HADZIBABIC. Persistent Currents in Spinor Condensates. *Physical Review Letters*, **110**:2 (Jan. 2013), p. 025301.

[5] A. F. ANDREEV and E. P. BASHKIN. Three-velocity hydrodynamics of superfluid solutions. *Journal of Experimental and Theoretical Physics*, **42**:1 (1975), pp. 164–167.

[6] S. I. SHEVCHENKO and D. V. FIL. The Andreev-Bashkin effect in a two-component Bose gas. *Journal of Experimental and Theoretical Physics*, **105**:1 (July 2007), pp. 135–137.

[7] M.-S. CHANG, Q. QIN, W. ZHANG, L. YOU, and M. S. CHAPMAN. Coherent spinor dynamics in a spin-1 Bose condensate. *Nature Physics*, **1**:2 (Oct. 2005), pp. 111–116.

[8] T. ZIBOLD, E. NICKLAS, C. GROSS, and M. K. OBERTHALER. Classical Bifurcation at the Transition from Rabi to Josephson Dynamics. *Physical Review Letters*, **105**:20 (Nov. 2010), p. 204101.

[9] J. I. CIRAC, M. LEWENSTEIN, K. MØLMER, and P. ZOLLER. Quantum superposition states of Bose-Einstein condensates. *Physical Review A*, **57**:2 (Feb. 1998), pp. 1208–1218.

[10] C. GROSS, H. STROBEL, E. NICKLAS, T. ZIBOLD, N. BAR-GILL, G. KURIZKI, and M. K. OBERTHALER. Atomic homodyne detection of continuous-variable entangled twin-atom states. *Nature*, **480**:7376 (Dec. 2011), pp. 219–23.

[11] D. T. SON and M. A. STEPHANOV. Domain walls of relative phase in two-component Bose-Einstein condensates. *Physical Review A*, **65**:6 (June 2002), p. 063621.

[12] K. KASAMATSU, M. TSUBOTA, and M. UEDA. Vortex molecules in coherently coupled two-component Bose-Einstein condensates. *Physical review letters*, **93**:25 (Dec. 2004), p. 250406.

[13] B. DECONINCK, P. G. KEVREKIDIS, H. E. NISTAZAKIS, and D. J. FRANTZESKAKIS. Linearly coupled Bose-Einstein condensates: From Rabi oscillations and quasiperiodic solutions to oscillating domain walls and spiral waves. *Physical Review A*, **70**:6 (Dec. 2004), p. 063605.

[14] J. SABBATINI, W. H. ZUREK, and M. J. DAVIS. Phase separation and pattern formation in a binary Bose-Einstein condensate. *Physical review letters*, **107**:23 (Dec. 2011), p. 230402.

[15] C. LEE, W. HAI, L. SHI, and K. GAO. Phase-dependent spontaneous spin polarization and bifurcation delay in coupled two-component Bose-Einstein condensates. *Physical Review A*, **69**:3 (Mar. 2004), p. 033611.

[16] N. R. BERNIER, E. G. DALLA TORRE, and E. DEMLER. Unstable avoided crossing in coupled spinor condensates. *Physical review letters*, **113**:6 (Aug. 2014), p. 065303.

[17] J. DALIBARD, F. GERBIER, G. JUZELIŪNAS, and P. ÖHBERG. Colloquium : Artificial gauge potentials for neutral atoms. *Reviews of Modern Physics*, **83**:4 (Nov. 2011), pp. 1523–1543.

[18] J. CATANI, G. LAMPORESI, D. NAIK, M. GRING, M. INGUSCIO, F. MINARDI, A. KANTIAN, and T. GIAMARCHI. Quantum dynamics of impurities in a one-dimensional Bose gas. *Physical Review A*, **85**:2 (Feb. 2012), p. 023623.

[19] T. FUKUHARA, A. KANTIAN, M. ENDRES, M. CHENEAU, P. SCHAUSS, S. HILD, D. BELLEM, U. SCHOLLWÖCK, T. GIAMARCHI, C. GROSS, I. BLOCH, and S. KUHR. Quantum dynamics of a mobile spin impurity. *Nature Physics*, **9**:4 (Feb. 2013), pp. 235–241.

[20] I. AFFLECK. Quantum Impurity Problems in Condensed Matter Physics. (Sept. 2008), p. 44. arXiv: 0809.3474.

[21] A. SARTORI and A. RECATI. Dynamics of highly unbalanced Bose-Bose mixtures: Miscible vs. immiscible gases. *European Physical Journal D*, **67**:260 (2013).

[22] M. ABAD, A. SARTORI, S. FINAZZI, and A. RECATI. Persistent currents in two component condensates in a toroidal trap. *Physical Review A*, **89**:5 (May 2014), p. 11.

[23] A. SARTORI, J. MARINO, S. STRINGARI, and A. RECATI. Spin-dipole oscillation and relaxation of coherently coupled Bose-Einstein condensates. *New Journal of Physics*, **17**:9 (Sept. 2015), p. 093036.

[24] L. P. PITAEVSKII and S. STRINGARI. *Bose-Einstein Condensation*. International Series of Monographs on Physics. Oxford University Press, 2003, p. 400.

[25] Y. CASTIN. Bose-Einstein Condensates in Atomic Gases: Simple Theoretical Results. *Coherent atomic matter waves: 27 July–27 August 1999*. Ed. by R. KAISER, C. WESTBROOK, and F. DAVID. Vol. 72. Les Houches - Ecole d'Ete de Physique Theorique. Berlin, Heidelberg: Springer Berlin Heidelberg, 2001, pp. 1–136.

[26] E. P. GROSS. Structure of a quantized vortex in boson systems. *Il Nuovo Cimento*, **20**:3 (May 1961), pp. 454–477.

[27] L. P. PITAEVSKII. Vortex Lines in an Imperfect Bose Gas. *Journal of Experimental and Theoretical Physics*, **13**:2 (1961), p. 451.

[28] E. H. LIEB, R. SEIRINGER, J. P. SOLOVEJ, and J. YNGVASON. The Mathematics of the Bose Gas and its Condensation. (Oct. 2006), p. 213.

[29] T.-L. HO and V. B. SHENOY. Binary Mixtures of Bose Condensates of Alkali Atoms. *Physical Review Letters*, **77**:16 (Oct. 1996), pp. 3276–3279.

[30] A. L. GAUNT, T. F. SCHMIDUTZ, I. GOTLIBOVYCH, R. P. SMITH, and Z. HADZIBABIC. Bose-Einstein Condensation of Atoms in a Uniform Potential. *Physical Review Letters*, **110**:20 (May 2013), p. 200406.

[31] W. B. COLSON and A. L. FETTER. Mixtures of Bose liquids at finite temperature. *Journal of Low Temperature Physics*, **33**:3-4 (Nov. 1978), pp. 231–242.

[32] A. A. SVIDZINSKY and S. T. CHUI. Normal modes and stability of phase-separated trapped Bose-Einstein condensates. *Physical Review A*, **68**:1 (July 2003), p. 013612.

[33] F. RIBOLI and M. MODUGNO. Topology of the ground state of two interacting Bose-Einstein condensates. *Physical Review A*, **65**:6 (June 2002), p. 063614.

[34] P. TOMMASINI, E. J. V. DE PASSOS, A. F. R. DE TOLEDO PIZA, M. S. HUSSEIN, and E. TIMMERMANS. Bogoliubov theory for mutually coherent condensates. *Physical Review A*, **67**:2 (Feb. 2003), pp. 1–17.

[35] P. B. BLAKIE, R. J. BALLAGH, and C. W. GARDINER. Dressed states of a two component Bose-Einstein condensate. *Journal of Optics B: Quantum and Semiclassical Optics*, **1**:4 (Aug. 1999), pp. 378–382.

[36] C. P. SEARCH and P. R. BERMAN. Manipulating the speed of sound in a two-component Bose-Einstein condensate. *Physical Review A*, **63**:4 (Mar. 2001), p. 043612.

[37] E. V. GOLDSTEIN and P. MEYSTRE. Quasiparticle instabilities in multicomponent atomic condensates. *Physical Review A*, **55**:4 (Apr. 1997), pp. 2935–2940.

[38] C. P. SEARCH, A. G. ROJO, and P. R. BERMAN. Ground state and quasiparticle spectrum of a two-component Bose-Einstein condensate. *Physical Review A*, **64**:1 (June 2001), p. 013615.

[39] M. ABAD and A. RECATI. A study of coherently coupled two-component Bose-Einstein condensates. *The European Physical Journal D*, **67**:7 (July 2013), p. 148.

[40] S. GUPTA, K. W. MURCH, K. L. MOORE, T. P. PURDY, and D. M. STAMPER-KURN. Bose-Einstein condensation in a circular waveguide. *Physical review letters*, **95**:14 (Sept. 2005), p. 143201.

[41] S. MOULDER, S. BEATTIE, R. P. SMITH, N. TAMMUZ, and Z. HADZIBABIC. Quantized supercurrent decay in an annular Bose-Einstein condensate. *Physical Review A*, **86**:1 (July 2012), p. 013629.

[42] F. BLOCH. Superfluidity in a Ring. *Physical Review A*, **7**:6 (June 1973), pp. 2187–2191.

[43] M. BENAKLI, S. RAGHAVAN, A. SMERZI, S. FANTONI, and S. R. SHENOY. Macroscopic angular-momentum states of Bose-Einstein condensates in toroidal traps. *Europhysics Letters (EPL)*, **46**:3 (May 1999), pp. 275–281.

[44] J. TEMPERE, J. T. DEVREESE, and E. R. I. ABRAHAM. Vortices in Bose-Einstein condensates confined in a multiply connected Laguerre-Gaussian optical trap. *Physical Review A*, **64**:2 (July 2001), p. 023603.

[45] P. CAPUZZI and D. M. JEZEK. Stationary arrays of vortices in Bose-Einstein condensates confined by a toroidal trap. *Journal of Physics B: Atomic, Molecular and Optical Physics*, **42**:14 (July 2009), p. 145301.

[46] J. D. REPPY. Application of a Superfluid Gyroscope to the Study of Critical Velocities in Liquid Helium Near the λ Transition. *Physical Review Letters*, **14**:18 (May 1965), pp. 733–735.

[47] O. AVENEL and E. VAROQUAUX. Observation of singly quantized dissipation events obeying the Josephson frequency relation in the critical flow of superfluid 4He through an aperture. *Physical review letters*, **55**:24 (Dec. 1985), pp. 2704–2707.

[48] E. VAROQUAUX, M. MEISEL, and O. AVENEL. Onset of the critical velocity regime in superfluid 4He at low temperature. *Physical review letters*, **57**:18 (Nov. 1986), pp. 2291–2294.

[49] J. DAVIS, J. STEINHAUER, K. SCHWAB, Y. MUKHARSKY, A. AMAR, Y. SASAKI, and R. PACKARD. Evidence for quantum tunneling of phase-slip vortices in superfluid 4He. *Physical review letters*, **69**:2 (July 1992), pp. 323–326.

[50] A. RAMANATHAN, K. C. WRIGHT, S. R. MUNIZ, M. ZELAN, W. T. HILL, C. J. LOBB, K. HELMERSON, W. D. PHILLIPS, and G. K. CAMPBELL. Superflow in a Toroidal Bose-Einstein Condensate: An Atom Circuit with a Tunable Weak Link. *Physical Review Letters*, **106**:13 (Mar. 2011), p. 130401.

[51] K. C. WRIGHT, R. B. BLAKESTAD, C. J. LOBB, W. D. PHILLIPS, and G. K. CAMPBELL. Driving Phase Slips in a Superfluid Atom Circuit with a Rotating Weak Link. *Physical Review Letters*, **110**:2 (Jan. 2013), p. 025302.

[52] S. BARGI, F. MALET, G. M. KAVOULAKIS, and S. M. REIMANN. Persistent currents in Bose gases confined in annular traps. *Physical Review A*, **82**:4 (Oct. 2010), p. 043631.

[53] Z. WU and E. ZAREMBA. Mean-field yrast spectrum of a two-component Bose gas in ring geometry: Persistent currents at higher angular momentum. *Physical Review A*, **88**:6 (Dec. 2013), p. 063640.

[54] Z. WU, E. ZAREMBA, J. SMYRNAKIS, M. MAGIROPOULOS, N. K. EFREMIDIS, and G. M. KAVOULAKIS. Mean-field yrast spectrum and persistent currents in a two-component Bose gas with interaction asymmetry. *Physical Review A*, **92**:3 (Sept. 2015), p. 033630.

[55] A. I. YAKIMENKO, K. O. ISAIEVA, S. I. VILCHINSKII, and M. WEYRAUCH. Stability of persistent currents in spinor Bose-Einstein condensates. *Physical Review A*, **88**:5 (Nov. 2013), p. 051602.

[56] H. TAKEUCHI, S. ISHINO, and M. TSUBOTA. Binary Quantum Turbulence Arising from Countersuperflow Instability in Two-Component Bose-Einstein Condensates. *Physical Review Letters*, **105**:20 (Nov. 2010), p. 205301.

[57] S. ISHINO, M. TSUBOTA, and H. TAKEUCHI. Countersuperflow instability in miscible two-component Bose-Einstein condensates. *Physical Review A*, **83**:6 (June 2011), p. 063602.

[58] C. K. LAW, C. M. CHAN, P. T. LEUNG, and M.-C. CHU. Critical velocity in a binary mixture of moving Bose condensates. *Physical Review A*, **63**:6 (May 2001), p. 063612.

[59] L. Y. KRAVCHENKO and D. V. FIL. Stationary Waves in a Supersonic Flow of a Two-Component Bose Gas. *Journal of Low Temperature Physics*, **155**:5-6 (Apr. 2009), pp. 219–234.

[60] C. HAMNER, J. J. CHANG, P. ENGELS, and M. A. HOEFER. Generation of Dark-Bright Soliton Trains in Superfluid-Superfluid Counterflow. *Physical Review Letters*, **106**:6 (Feb. 2011), p. 065302.

[61] M. A. HOEFER, J. J. CHANG, C. HAMNER, and P. ENGELS. Dark-dark solitons and modulational instability in miscible two-component Bose-Einstein condensates. *Physical Review A*, **84**:4 (Oct. 2011), p. 041605.

[62] T. OZAWA, L. P. PITAEVSKII, and S. STRINGARI. Supercurrent and dynamical instability of spin-orbit-coupled ultracold Bose gases. *Physical Review A*, **87**:6 (June 2013), p. 063610.

[63] F. PIAZZA, L. A. COLLINS, and A. SMERZI. Vortex-induced phase-slip dissipation in a toroidal Bose-Einstein condensate flowing through a barrier. *Physical Review A*, **80**:2 (Aug. 2009), p. 021601.

[64] M. ABAD, M. GUILLEUMAS, R. MAYOL, M. PI, and D. M. JEZEK. Dipolar condensates confined in a toroidal trap: Ground state and vortices. *Physical Review A*, **81**:4 (Apr. 2010), p. 043619.

[65] M. ABAD. Persistent currents in coherently coupled Bose-Einstein condensates in a ring trap. (Nov. 2015), p. 12. arXiv: 1511.03768.

[66] R. W. PATTINSON, T. P. BILLAM, S. A. GARDINER, D. J. MCCARRON, H. W. CHO, S. L. CORNISH, N. G. PARKER, and N. P. PROUKAKIS. Equilibrium solutions for immiscible two-species Bose-Einstein condensates in perturbed harmonic traps. *Physical Review A*, **87**:1 (Jan. 2013), p. 013625.

[67] A. SARTORI. Mixtures of atomic Bose gases: ground state and dynamics. Master Thesis. University of Trento, 2012.

[68] C. MENOTTI and S. STRINGARI. Collective oscillations of a one-dimensional trapped Bose-Einstein gas. *Physical Review A*, **66**:4 (Oct. 2002), p. 043610.

[69] P. G. KEVREKIDIS, H. E. NISTAZAKIS, D. J. FRANTZESKAKIS, B. A. MALOMED, and R. CARRETERO-GONZALEZ. Families of matter-waves in two-component Bose-Einstein condensates. *The European Physical Journal D - Atomic, Molecular and Optical Physics*, **28**:2 (Feb. 2004), pp. 181–185.

[70] A. RECATI and S. STRINGARI. Spin Fluctuations, Susceptibility, and the Dipole Oscillation of a Nearly Ferromagnetic Fermi Gas. *Physical Review Letters*, **106**:8 (Feb. 2011), p. 080402.

[71] O. BOHIGAS, A. LANE, and J. MARTORELL. Sum rules for nuclear collective excitations. *Physics Reports*, **51**:5 (Apr. 1979), pp. 267–316.

[72] E. LIPPARINI and S. STRINGARI. Sum rules and giant resonances in nuclei. *Physics Reports*, **175**:3-4 (Apr. 1989), pp. 103–261.

[73] A. SARTORI. *Spinor BEC spind-dipole oscillation in paramagnetic regime*. YouTube. https://youtu.be/bZ7PCF6aQOE.

[74] A. SARTORI. *Spinor BEC spind-dipole oscillation in paramagnetic regime for equal interactions*. YouTube. https://youtu.be/2DublN6hrkI.

[75] A. SARTORI. *Spinor BEC spind-dipole oscillation in ferromagnetic regime: ground state relaxation*. YouTube. https://youtu.be/RpUU5myNVro.

[76] L. D. LANDAU and LIFSHITZ E. M. *Statistical Physics Part 1*. Oxford Pergamon, 1980.

[77] WEINBERG E. J. *Classical Solutions in Quantum Field Theory: Solitons and Instantons in High Energy Physics*. Cambridge University Press, 2015, p. 342.

[78] W. BAO, S. JIN, and P. A. MARKOWICH. Numerical Study of Time-Splitting Spectral Discretizations of Nonlinear Schrödinger Equations in the Semiclassical Regimes. *SIAM Journal on Scientific Computing*, **25**:1 (Jan. 2003), pp. 27–64.

[79] W. BAO, D. JAKSCH, and P. A. MARKOWICH. Numerical solution of the Gross-Pitaevskii equation for Bose-Einstein condensation. *Journal of Computational Physics*, **187**:1 (May 2003), pp. 318–342.

[80] M. FRIGO and S. G. JOHNSON. *FFTW Home Page*. `http://www.fftw.org/`.

[81] M. TSUBOTA, K. KASAMATSU, and M. UEDA. Vortex lattice formation in a rotating Bose-Einstein condensate. *Physical Review A*, **65**:2 (Jan. 2002), p. 023603.

[82] S. R. WHITE. Density matrix formulation for quantum renormalization groups. *Physical review letters*, **69**:19 (Nov. 1992), pp. 2863–2866.

[83] S. R. WHITE. Density-matrix algorithms for quantum renormalization groups. *Physical Review B*, **48**:14 (Oct. 1993), pp. 10345–10356.

[84] F. VERSTRAETE, D. PORRAS, and J. I. CIRAC. Density matrix renormalization group and periodic boundary conditions: a quantum information perspective. *Physical review letters*, **93**:22 (Nov. 2004), p. 227205.

[85] A. J. DALEY, C. KOLLATH, U. SCHOLLWÖCK, and G. VIDAL. Time-dependent density-matrix renormalization-group using adaptive effective Hilbert spaces. *Journal of Statistical Mechanics: Theory and Experiment*, **2004**:04 (Apr. 2004), P04005.

[86] D. POULIN, A. QARRY, R. SOMMA, and F. VERSTRAETE. Quantum simulation of time-dependent Hamiltonians and the convenient illusion of Hilbert space. *Physical review letters*, **106**:17 (Apr. 2011), p. 170501.

[87] J. HAEGEMAN, J. I. CIRAC, T. J. OSBORNE, I. PIŽORN, H. VERSCHELDE, and F. VERSTRAETE. Time-Dependent Variational Principle for Quantum Lattices. *Physical Review Letters*, **107**:7 (Aug. 2011), p. 070601.

[88] J. HAEGEMAN, C. LUBICH, I. OSELEDETS, B. VANDEREYCKEN, and F. VERSTRAETE. Unifying time evolution and optimization with matrix product states. *Arxiv*, (Aug. 2014), p. 5. arXiv: `1408.5056`.

[89] R. B. SIDJE. *expokit web page*. `http://www.maths.uq.edu.au/expokit/`.

[90] R. B. SIDJE. Expokit: a software package for computing matrix exponentials. *ACM Transactions on Mathematical Software*, **24**:1 (1998), pp. 130–156.

[91] S. R. WHITE and A. E. FEIGUIN. Real-time evolution using the density matrix renormalization group. *Physical Review Letters*, **93**:7 (2004), pp. 1–4.

[92] G. DE CHIARA, M. RIZZI, D. ROSSINI, and S. MONTANGERO. Density Matrix Renormalization Group for Dummies. *Journal of Computational and Theoretical Nanoscience*, **5**:7 (July 2008), pp. 1277–1288.

[93] C. HUBIG, I. P. MCCULLOCH, U. SCHOLLWÖCK, and F. A. WOLF. Strictly single-site DMRG algorithm with subspace expansion. *Physical Review B*, **91**:15 (Apr. 2015), p. 155115.

[94] E. ZAREMBA. Sound propagation in a cylindrical Bose-condensed gas. *Physical Review A*, **57**:1 (Jan. 1998), pp. 518–521.

[95] G. M. KAVOULAKIS and C. J. PETHICK. Quasi-one-dimensional character of sound propagation in elongated Bose-Einstein condensed clouds. *Physical Review A*, **58**:2 (Aug. 1998), pp. 1563–1566.

[96] S. STRINGARI. Dynamics of Bose-Einstein condensed gases in highly deformed traps. *Physical Review A*, **58**:3 (Sept. 1998), pp. 2385–2388.

[97] P. O. FEDICHEV and G. V. SHLYAPNIKOV. Critical velocity in cylindrical Bose-Einstein condensates. *Physical Review A*, **63**:4 (Mar. 2001), p. 045601.